2026-01

Spatiotemporal Analysis of Ionospheric Total Electron Content and Equatorial Plasma Bubbles over East Africa Based on GNSS Observations

Amsalu, Hundesa

Bahir Dar University
College of Science
Department of Physics

Spatiotemporal Analysis of Ionospheric Total Electron Content and Equatorial Plasma Bubbles over East Africa Based on GNSS Observations

By

Amsalu Hundesa Dinede

January, 2026

Bahir Dar, Ethiopia

Bahir Dar University
College of Science
Department of Physics

Spatiotemporal Analysis of Ionospheric Total Electron Content and Equatorial Plasma Bubbles over East Africa Based on GNSS Observations

By

Amsalu Hundesa Dinede

A Dissertation Submitted In Partial Fulfillment Of The Requirements For The Degree of Doctor of Philosophy (Ph.D) In Space Physics

Supervisor Prof. Tsegaye Kassa (Ph.D)
Professor of Space Physics
Department of Physics
Bahir Dar University
Bahir Dar, Ethiopia

January, 2026

Bahir Dar, Ethiopia

Declaration

This is to certify that the thesis entitled "**Spatiotemporal Analysis of Ionospheric Total Electron Content and Equatorial Plasma Bubbles over East Africa Based on GNSS Observations**", submitted in partial fulfillment of the requirements for the degree of Doctor of Philosophy in Space Physics in Department of Physics, Bahir Dar University, is a record of original work carried out by me and has never been submitted to this or any other institution to get any other degree or certificates. The assistance and help I received during the course of this investigation have been duly acknowledged.

Amsalu Hundesa Dinede

Approval of Dissertation

I hereby certify that I have supervised, read, and evaluated this dissertation entitled "**Spatiotemporal Analysis of Ionospheric Total Electron Content and Equatorial Plasma Bubbles over East Africa Based on GNSS Observations**" by Amsalu Hundesa Dinede prepared under my guidance. I recommend the dissertation be submitted for oral defense.

Research Supervisor: ______________________________
Prof. Tsegaye Kassa

Department Head: ______________________________
Dr. Tamiru Negussie

Approval of Dissertation Defense Result

As members of the board of examiners, we examined this dissertation entitled "**Spatiotemporal Analysis of Ionospheric Total Electron Content and Equatorial Plasma Bubbles over East Africa Based on GNSS Observations**" by Amsalu Hundesa Dinede. We hereby certify that the dissertation is accepted for fulfilling the requirements for the award of the degree of Doctor of Philosophy in Space Physics.

Board of Examiners

External Examiner 1: ________________________
Prof. Aramesh Seif (Ph.D)

External Examiner 2: ________________________
Dr. Gebregiorgis Abraha (Ph.D)

Internal Examiner 1: ________________________
Dr. Melessew Nigussie (Ph.D)

Internal Examiner 2: ________________________
Dr. Ambelu Tebabal (Ph.D)

Research Supervisor: ________________________
Prof. Tsegaye Kassa (Ph.D)

Chair-man: ________________________
Dr. Tamiru Negussie (Ph.D)

Acknowledgment

First and foremost, I would like to express my deepest gratitude to God for granting me the strength, patience, and perseverance to complete this dissertation. Without His divine guidance and grace, this achievement would not have been possible. I extend my heartfelt appreciation to my advisor, Professor Tsegaye Kassa Gogie, for his invaluable mentorship, continuous encouragement, and insightful feedback throughout every stage of this research. His unwavering support and wisdom have played a critical role in shaping the quality and depth of this work. I am also sincerely thankful to Professor Melessew Nigussie Gereme, whose dedicated teaching and consistent support during my Ph.D. coursework significantly influenced my academic development. His clarity in instruction and willingness to help were deeply impactful and greatly appreciated.

My gratitude also goes to Dr. Ambelu Tebable and Dr. Tamiru Nigussie, for their academic guidance, encouragement, and kind support during various stages of this study. Their availability and professional insights were invaluable to my progress. I am especially grateful to my dear friends, Andarge Gerawork, Dr. Shumet Worke, and Dr. Tsehaye Negashe. Your genuine friendship, encouragement, and moral support have been a tremendous source of strength to me throughout this journey. The shared experiences, thoughtful conversations, and lighthearted moments have made this challenging path more rewarding and meaningful. I would also like to thank the faculty and staff of the Department of Physics at Bahir Dar University and Bonga University for their academic support and institutional assistance. I appreciate all individuals who contributed directly or indirectly to the success of this research. My special thanks go to the institutions and data providers whose resources were essential to the completion of this work.

A special and heartfelt acknowledgment goes to my beloved wife, Tarike Senbeta Jimma, for her endless love, patience, and steadfast support. Your belief in me, especially during the most demanding times, gave me the strength to continue and complete this journey. To my precious daughter, Ablakt Amsalu, your smile and presence brought light and joy into my life and inspired me every day to keep going. Lastly, to my beloved family thank you for your unconditional love, prayers, and support. I am especially grateful to my mother, Shashitu Eba, and my father, Hundesa Dinede, whose sacrifices, values, and encouragement laid the foundation for my academic and personal growth. Your unwavering love and belief in me have been the greatest gift of all.

Abstract

This dissertation explores the spatiotemporal variations of ionospheric Total Electron Content (TEC) and the characteristics of Equatorial Plasma Bubbles (EPBs) over East Africa, based on a comprehensive analysis of global navigation satellite system (GNSS) TEC gathered from 2012 to 2016. Understanding these phenomena is essential for enhancing the accuracy of satellite-based navigation, communication, and positioning systems, particularly in regions like East Africa that are vulnerable to ionospheric disturbances. Employing Ordinary Kriging (OK), geostatistical interpolation technique, this research meticulously quantifies the spatial and temporal behavior of TEC across various geographic regions within Ethiopia. The results indicate significant diurnal variations, with TEC values consistently peaking around noon (approximately 12: 00 UT) and showing marked differences across latitudes. For instance, northern regions often display elevated TEC levels compared to southern areas, highlighting a pronounced north-south gradient that aligns with variations in solar and geomagnetic influences. In addition to TEC analysis, the study employs GNSS- derived parameters such as the Rate of TEC Index (ROTI) and slant TEC (sTEC) to characterize the occurrence and dynamics of EPBs during geomagnetically quiet conditions. The findings reveal that EPB activity predominantly occurs between 17:00 and 22:00 UT, with peak occurrences aligned with equinox seasons. This pattern underscores the influence of solar terminator alignment with the geomagnetic meridian, which facilitates the generation of EPBs through enhanced vertical plasma drift and subsequent Rayleigh-Taylor instability. Furthermore, the research establishes correlation between TEC variability and EPB occurrences, suggesting that increased TEC prior to sunset enhances the likelihood of EPB formation. The insights gained from this study contribute to a deeper understanding of equatorial ionospheric dynamics and the complex interactions between solar activity, geomagnetic conditions, and ionospheric structure. Overall, this dissertation not only advances the scientific knowledge of ionospheric behaviors in East Africa but also emphasizes the effectiveness of geostatistical modeling techniques in enhancing predictive capabilities for TEC variability and EPB dynamics. By providing a detailed analysis of these crucial phenomena, this work aims to support improved forecasting and mitigation strategies for the impacts of space weather on technological systems reliant on accurate ionospheric data.

Keywords: Total Electron Content (TEC), Equatorial Plasma Bubbles (EPBs), Global Navigation Satellite System (GNSS), Ordinary Kriging (OK), Rate of TEC Index (ROTI), Ionospheric Variability.

Dedication

This dissertation is dedicated to Tarike Senbeta Jimma, Ablakt Amsalu Hundesa and to all my family, whose love, patience, and unwavering support have sustained me throughout this journey. Your presence in my life has been a constant source of strength, inspiration, and purpose as I walked this path of learning and discovery.

Publications and Presentations

Publications

1. Amsalu Hundesa, Tsegaye Kassa and Fasil Tesema (2025), Study of Total Electron Content Variations over the Ethiopian region using Kriging Technique, Geomagnetism and Aeronomy, $https://doi.org/10.1134/S0016793224600942$.

2. Amsalu Hundesa and Tsegaye Kassa (2025), Characterization of equatorial plasma bubbles over the East African Sector using the ROTI and sTEC depletion depth, Advances in Space Research, $https://doi.org/10.1016/j.asr.2025.03.062$.

Work in progress

1. Amsalu Hundesa and Tsegaye Kassa, Investigation of Total Electron Content Responses to Equatorial Plasma Bubbles, under review on, Advances in Space Research.

Presentations

1. Amsalu Hundesa and Tsegaye Kassa (2025), **Characterization of equatorial plasma bubbles over the East African Sector using the ROTI and sTEC depletion depth**. In the **5th African Graduate Students Conference** ($AGSCV - BDU - 2025$) held on May $12 - 13$, 2025 at Bahir Dar University, Bahir Dar, Ethiopia.

2. Amsalu Hundesa and Tsegaye Kassa (2025), **Characterization of equatorial plasma bubbles over the East African Sector using the ROTI and sTEC depletion depth**. The **13th Annual National Conference on Recent Trends in scientific Research** ($NCRTSR-2025$) held on June $20-21$, 2025 at Bahir Dar University, Bahir Dar, Ethiopia.

3. **Spatiotemporal Variations of Ionospheric Total electron Content and Equatorial Plasma Bubbles over East Africa using Kriging and GNSS-Derived Parameters** held on 07/11/2025, **Seminar presentation**.

Contents

List of Figures

List of Tables

Abbreviations and Acronyms

EIA	Equatorial Ionization Anomaly
Dst	Disturbance Storm Time index
sTEC	Slant Total Electron Content
TEC	Total Electron Content
VTEC	Vertical Total Electron Content
TECU	Total Electron Content Unit
EPB	Equatorial Plasma Bubble
RTI	Rayleigh−Taylor Instability
GNSS	Global Navigation Satellite System
ROTI	Rate of Change of Total Electron Content Index
GPS	Global Positioning System
UV	Ultraviolet
HF	High-Frequency
TID	Traveling Ionospheric Disturbance
S_4	Amplitude Scintillation Index
$\delta\phi$	Phase Scintillation Index
ESF	Equatorial Spread-F
OK	Ordinary Kriging
UK	Universal Kriging
SK	Simple Kriging
IK	Indicator Kriging
CK	Co-Kriging
UT	Universal Time
LT	Local Time
RMSRes	Root Mean Square Residuals
AU	Astronomical Unit
F10.7	Solar radio flux
EUV	Extreme Ultraviolet
MEO	Medium Earth Orbit
PRN	Pseudo Range Noise
V_g	Group Velocity
V_ϕ	Phase Velocity
f_p	Plasma frequency
Ne	Electron density
Δt	Time delay

ΔE	Perturbed electric filed
PRE	pre-reversal enhancement
SSN	Sunspot number
dsTEC	depletion in slant total electron content
σ_o	Parallel conductivity
P_σ	Pedersen conductivity
H_σ	Hall conductivity
q	Electron production
L	Loss due to electron
e	Electron
E	Electric filed
B	Magnetic filed
J	Current density
V_i	Velocity of ion
MF	Mapping function
IPP	Ionospheric price point
Dp	Depletion depth
L_{max}	Left maximum
R_{max}	Right maximum
RESE	Root mean square error
MAE	Mean absolute error
TEC_{min}	Minimum total electron content
nT	nano-Tesla
IDW	Inverse Distance Weighting
MQ	Multiquadric function
KR	Kriging
NN	Neural Network

Chapter 1

Introduction

Sun is a nearly perfect sphere of hot plasma. It provides energy necessary for life on Earth and governs the orbits of the planets and other celestial bodies (Fitzpatrick, 2022; Gombosi, 1998; Hargreaves, 1992; Prölss, 2012). Sun has three constitutive layers photosphere, chromosphere and corona. The lowest layer is the photosphere. This layer has a temperature of about $5,773°K$ and features sunspots, darker, and cooler regions caused by magnetic disturbances. Above the photosphere lies the chromosphere, a thinner region that appears as a reddish glow during solar eclipses. It has temperatures around $6,273°K$ at the base to approximately $25,273°K$ at higher altitudes (Shaver et al., 2024). Just above that is the transition region, a very narrow zone where the temperature increases sharply, jumping from thousands to millions of degrees in a short vertical distance. The outermost layer is the corona, which stretches millions of kilometers into space (Kivelson and Russell, 1995).

The change in space environment between the sun and Earth called space weather. These conditions influence a wide range of geophysical processes. In particular, the Earths ionosphere is highly sensitive to variations in space weather, which can significantly alter its structure and behavior (Seif and Panda, 2023). Consequently, researchers study the ionosphere find the propagation of ionospheric irregularities during space weather events to be an intriguing field of study (Vankadara et al., 2022). The ionospheric irregularities are more dynamic at the magnetic equator. During the night, the lower ionosphere quickly decays, and the raised F-layer's bottom side experiences a vertical density gradient (Kelley, 2009). The electron density in the F_2 ionospheric region rapidly rises to higher altitudes in the evening sector due to an upward plasma $\overrightarrow{E} \times \overrightarrow{B}$ drift, known as the pre-reversal enhancement (PRE) (Farley et al., 1986; Haerendel et al., 1992; Heelis, 2004; Heelis et al., 1974). The drifted plasma triggers plasma instability on the bottom side of the F region through the well-known generalized Rayleigh-Taylor Instability (RTI) mechanism (Huba and Ossakow, 1981; Sultan, 1996). The RTI initiates the development of Equatorial Plasma Bubbles (EPBs) (Gentile et al., 2006; Li et al., 2021). Then the EPBs can have a significant impact on propagation of signals, navigation and radio wave communication systems. These bubbles possess the potential to disrupt the propagation of radio waves, leading to fluctuations in signal strength, phase, and time delay (Pedatella et al., 2024). These disruptions caused by EPBs, known as ionospheric scintillations, present challenges for the reliable and efficient operation of these systems, especially in regions where EPBs are prevalent, such as the equatorial and low-latitude ionosphere(Chen et al., 2008). The scintillation level is identified using the Amplitude and Phase Scintillation (Acharya and Majumdar, 2019; Carrano et al., 2019; Li et al., 2020a; Manga et al., 2021). Scintillations are more prominent after sunset and during midnight hours (Vankadara et al., 2022). It degrades the accuracy and reliability of space-based positioning and navigational operations, such as the Global Navigation Satellite System (GNSS), by causing signal fading, cycle slips, signal distortion, interruptions, or loss of lock (Carmo et al., 2021; Gentile et al., 2006; Magdaleno et al., 2017; Mendillo et al., 2001).

The Global Positioning System (GPS) consists of a network of satellites and receiving devices that work together to determine precise locations on Earth. It is a crucial tool for researching ionospheric plasma bubbles and spatiotemporal variability of TEC. Because its has the ability to optimize the simultaneous study of ionospheric irregularities over large areas (Kintner et al., 2007; Vankadara et al., 2022). GPS receivers can measure the TEC along the signal path between the satellites and the receivers, providing valuable data for studying ionospheric disturbances, including plasma bubbles (Jakowski et al., 2011). By analyzing the TEC data, researchers can identify the spatial-temporal variability of TEC and characteristics of plasma bubbles, such as their occurrence rate, size, altitude, drift velocity, and evolution (Kintner et al., 2007).

The study of ionospheric TEC variability and plasma bubbles is important for various applications. In the field of satellite-based navigation and positioning systems, understanding and mitigating the effects of plasma bubbles are crucial for improving the accuracy and reliability of GPS and other satellite navigation systems (Datta-Barua and Bust, 2011; Lee et al., 2011). For example, by developing advanced algorithms and models that capture the spatial-temporal variability of TEC and predict the occurrence and behavior of plasma bubbles. The navigation systems can implement corrective strategies to reduce the impact of ionospheric scintillation on signal quality and positioning performance (Ledvina et al., 2008). Geomagnetic and solar indices are used to observe different phenomenon inside ionosphere. Those are the Dst (Disturbance Storm Time), Kp, Sunspot numbers and F10.7 indices. The Dst and Kp indices are two widely used geomagnetic indices's that quantify the level of geomagnetic activity in Earth's magnetosphere, primarily in response to solar wind disturbances. These indices serve as critical indicators in space weather monitoring and forecasting, especially for understanding the impact of geomagnetic storms on satellite systems, navigation signals, and power grids. The Dst index is used to identify the strengths of geomagnetic storms as weak, moderate storm, strong storm, severe strong storm and super intense (Gonzalez et al., 1994). The Kp index, on the other hand, provides a global measure of geomagnetic activity over a three hour period and ranges from 0 to 9 (Mandea and Korte, 2010). Kp= 0 to 1, quiet, Kp= 2 to 3, unsettled, Kp=4, active, Kp= 5, minor storm, Kp= 6, moderate storm, Kp=7, strong storm, Kp= 8, severe storm, and Kp=9, extreme storm. The other solar index is the sunspot number (SSN). SSN are temporary phenomena on the photosphere of the Sun that appear visibly as dark spots compared to surrounding regions (Davies, 1990). They are caused by intense magnetic activity, which inhibits convection by an effect comparable to the eddy current brake, forming areas of reduced surface temperature. They usually appear in pairs, with each SSN having the opposite magnetic pole to the other. SSN can be used to measure the solar rotation. Galileo was one of the first who saw SSN using a telescope. He used it to measure the period of solar rotation (Kumar, 2017).

In this work Geostatistical interpolation techniques, and GNSS-derived parameters, are employed to investigate the spatiotemporal variability of TEC and occurrence of EPBs during geomagnetically quiet periods. The Kriging method is geostatistical method used to study the spatial and temporial variation of TEC over the region. It is interpolation technique originated from the work of South African mining engineer Daniel Gerhardus Kriging, who developed a statistical approach for estimating gold concentrations (Türkoğlu et al., 2016). Over time, Kriging has evolved into several variants, including Simple Kriging (SK), Ordinary Kriging (OK), Universal Kriging (UK), Co-Kriging (ck), and Indicator Kriging (IK) (Türkoğlu et al., 2016). In this study, we applied OK to interpolate GPS-derived TEC across the East African sector (Abe et al., 2018). OK offers several advantages over UK, particularly in situations involving limited data availability and uncertain spatial trends. Unlike UK, which requires explicit modeling of a deterministic trend, OK assumes a constant but unknown local mean, reducing the risk of model misspecification when the trend is difficult to define (Nigussie et al., 2016). This makes OK more robust and reliable for smaller or sparsely distributed datasets. In addition, OK is computationally simpler, as it involves fewer parameters and lower computational cost compared to UK, which must estimate both the variogram and the trend components. As a result, OK is often preferred when computational efficiency is important and when the focus is on capturing local spatial variability rather than large-scale trends. This method was chosen because OK assumes a locally constant but unknown mean, which aligns well with the spatial characteristics of TEC in the low-latitude ionosphere. Such an assumption provides a realistic approximation of TEC behavior in this region, enhancing the accuracy of spatial estimations (Isaaks et al., 1989). This interpolation technique has different types of Variogram methods, such as Spherical, Exponential and Gaussian Variogram and the performance of those variogram those are reported.

The GNSS-derived parameters are Rate of Change of Total Electron Content Index (ROTI) is utilized to measure the level of irregularities because ROTI and S4 indices exhibit excellent agreement, depletion depth of sTEC, and duration of the depletion which are used to characterize the occurrence of EPB (Babu Sree Harsha et al., 2020; Seif and Panda, 2023; Seok et al., 2022; Vankadara et al., 2022). EPB occurrences are found to be dependent on various factors, including the time of day, season, latitude, longitude, and conductivity of the E-region (Kepkar et al., 2020; Kumar et al., 2016). It has been demonstrated that the frequency of EPB events varies with solar activity and is higher during years with high solar activity (Pimenta et al., 2001; Sahai et al., 2000; Smith and Heelis, 2017; Sobral et al., 2002). Plasma bubbles are considered to occur when the observed total electron content (TEC) depletions from a satellite exceed 5 TECU and exhibit an apparent duration between 10 minutes and 180 minutes (Portillo et al., 2008). Kumar and Chen (2016) conducted investigations on the frequency and characteristics of plasma bubbles over Hong Kong using GNSS data between 2007 and 2009. Over the years, several techniques such as radar observation, ionogram analysis, in-situ satellite measurements, radio scintillation, airglow observation, and satellite-based measurements have been employed to study the characteristics of plasma bubbles (Abiriga et al., 2020; Kumar and Chen, 2016; Portillo et al., 2008). Many researchers have studied the spatiotemporal variation of TEC and occurrence of EPBs , at different latitudes, longitude and geographic locations using different time perspectives (Basu et al., 1999; Groves et al., 2000). Choi and Kil (2017) study the TEC variation and depletion in North Korea caused by a missile and rocket launch and the largest rocket launch in 2016 on February at 00:30 UT. Further studies were conducted on TEC variation in South American, on statistics of total electron depletion over the South America continent using 127 receivers (Seemala and Valladares, 2011). Mengist et al. (2015) map the East African Ionosphere Using Ground-based GPS-TEC Measurements by applying Inverse Distance Weighted (IDW) interpolation. Getahun et al. (2022) study comparative assessment of the performances of GPS-TEC assisted NTCM, NeQuick2 and Neural Network models to describe the East-African equatorial Ionosphere. Magdaleno et al. (2017) study climatologically characterization of equatorial plasma bubbles using GPS data global for the period 1998-2008. Giday et al. (2020) observes the effect of moderate geomagnetic storms on equatorial plasma bubbles over eastern Africa in the year 2012. Portillo et al. (2008) study equatorial plasma bubbles using African slant total electron content observations in 2004 taking six stations for six months. Existing studies, including statistical analyses, indicate that the African equatorial ionosphere exhibits irregularity patterns that are distinct from those observed in other longitude sectors. Despite its scientific significance and its coverage of the largest ground footprint along the geomagnetic equator, this region remains inadequately investigated.

This limited progress is primarily attributed to the scarcity of ground-based observational instruments, the lack of reliable regional total electron content (TEC) mapping models, insufficient characterization of equatorial plasma bubbles (EPBs), and the absence of a comprehensive regional ionospheric climatology. Moreover, most previous studies have focused on geomagnetically disturbed periods, leaving ionospheric behavior under quiet conditions relatively unexplored. In addition, existing modeling efforts largely rely on deterministic approaches, which may be insufficient to capture the complex and highly variable nature of ionospheric dynamics.

These gaps motivate the present study, which investigates the spatiotemporal variability of TEC and EPBs over the understudied East African equatorial region. To address the limitations imposed by sparse observations, a geostatistical modeling framework is employed to characterize ionospheric variability and quantify associated uncertainties. This approach enables the interpolation of observational gaps, enhances predictive capability, and facilitates the integration of diverse datasets while accounting for spatial and temporal autocorrelation inherent in sparsely distributed measurements.

This thesis investigates the spatiotemporal variation of TEC and the impact of ionospheric EPBs on GNSS signals over East Africa during Solar Cycle 24. The study focuses on, analyzing TEC variability across the region, characterizing equatorial EPBs, and examining the response of TEC to EPB events. To assess TEC variability, OK or a geostatistical interpolation method was employed. This technique allows for the prediction of unknown TEC values at specific locations using data from surrounding known points. For EPB characterization, we utilized several indicators, including the ROTI, depletion in slant TEC (dsTEC), and geomagnetic indices such as Kp and Dst, to identify and examine EPB occurrences. Finally, to understand the TEC response to EPBs, we carefully selected optimal time windows for analysis and EPB occurrence rate across four consecutive years. This selection process ensured that the impact of EPBs on TEC was accurately captured and interpreted.

1.1 Motivation

The ionosphere in low-latitude and equatorial regions exhibits complex and highly dynamic behavior due to the combined effects of solar radiation, geomagnetic field geometry, and electrodynamic processes. Unlike the mid and high-latitude ionosphere, the equatorial ionosphere is strongly influenced by the equatorial electrojet (EEJ), the equatorial ionization anomaly (EIA), and the presence of plasma irregularities such as EPBs (Christensen et al., 2003; Fejer, 1991). Probing EPBs and the associated ionospheric irregularities and dynamics at equatorial and low latitudes is critically important due to their significant impact on satellite-based communication, navigation, and surveillance systems. EPBs are large-scale depletions of plasma density that develop in the nighttime equatorial ionosphere and can rise to high altitudes, often extending to low latitudes. These structures cause rapid fluctuations in the ionospheric TEC, leading to signal scintillation and degradation of GNSS, such as GPS, particularly during post-sunset hours. The equatorial and low-latitude ionosphere is governed by unique electrodynamic processes, including the EEJ and PRE, which play a vital role in the initiation and evolution of EPBs. Understanding the spatial and temporal characteristics of these irregularities especially under quiet geomagnetic conditions is important for improving predictive models, enhancing the reliability of space-based systems, and supporting the development of regional space weather monitoring frameworks. This is especially crucial for equatorial regions like East Africa, where the socio-economic dependence on GNSS-based technologies is growing. The Earth's ionosphere frequently exhibits highly irregular plasma density and velocity fluctuations. Plasma irregularities in the F-region ionosphere occur predominantly at night and are of particular interest to space scientists due to the complex dynamical processes and instability mechanisms active at the equator and low latitude region. At the magnetic equator, the geomagnetic field lines are horizontal and oriented perpendicular to gravity. When combined with prevailing neutral winds and background electric fields, they create a unique electrodynamic environment. These conditions promote the development of plasma irregularities, which are typically aligned with the geomagnetic field.

In particular, GNSS-derived parameters such as ROTI, dSTEC, sTEC depletion depth, and depletion duration are analyzed to characterize the occurrence of EPBs. Their ability to capture uncertainty and variability makes them especially valuable for studying dynamic and data-sparse regions such as the African equatorial ionosphere.

This motivates us to addresses spatiotemporal variability of TEC and EPBs as well as their ionospheric impacts, which is under-studied. In this work spatial distribution of TEC across the East African region using the OK interpolation technique, which involves evaluating the performance of various semi-variogram models to ensure accurate spatial prediction of TEC. Additionally, the study introduces a novel approach that combines the ROTI with sTEC depletion analysis to identify and characterize EPBs under geomagnetically quiet conditions. Observations are based on data collected from stations located near the geomagnetic equator in the East African sector.

1.2 Research Objectives

The main goal of this research is to investigate the spatiotemporal variability of the ionospheric Total Electron Content (TEC) and the characteristics of Equatorial Plasma Bubbles (EPBs) over East Africa using GNSS-derived parameters and geostatistical modeling techniques. Specifically, the study aims to:

1. Analyze the spatial and temporal variations of ionospheric Total Electron Content (TEC) over Ethiopia by applying the Ordinary Kriging (OK) interpolation technique to GNSS observations.

2. Characterize the occurrence of Equatorial Plasma Bubbles (EPBs) during geomagnetically quiet conditions using GNSS-derived parameters such as the Rate of Total Electron Content Index (ROTI), slant TEC (sTEC), depletion depth of sTEC.

3. Examine the response of Total Electron Content (TEC) to Equatorial Plasma Bubble (EPB) events by integrating TEC variability analysis with ROTI and using different window size. This objective focuses on understanding how EPB activity modifies ionospheric electron density distribution, setting best candidate window size to detect the occurrence of EPBs and impacts GNSS signal integrity across the East African equatorial region.

Through these objectives, the study seeks to enhance the understanding of ionospheric dynamics in East Africa and to contribute to the development of regional models for monitoring and mitigating space weather effects on satellite-based navigation and communication systems.

This research seeks to investigate the following key scientific questions:

- How effectively can the OK interpolation technique capture the spatial and temporal variability of the ionosphere in the East African equatorial region?

- Which semi-variogram model provides the most accurate representation of TEC variability for reliable spatial prediction?

- To what extent does the Kriging derived TEC agree with GPS-measured TEC, and how strong is the correlation between the two datasets?

- Do GNSS-derived parameters such as ROTI, dSTEC, and sTEC depletion depth adequately represent the occurrence and characteristics of EPBs?

- Can EPBs be detected during geomagnetically quiet conditions, and what does their occurrence reveal about underlying ionospheric processes?

- What is the optimal temporal window size for effectively capturing sTEC depletion signatures and associated ionospheric irregularities?

1.3 Significance of the study

Africa, with its vast geographical footprint, remains underexplored in terms of ionospheric behavior, particularly in the East African region, where unique ionospheric dynamics play a significant role. The East African region, located directly on the magnetic equator, frequently experiences EPBs due to strong post-sunset electric fields, favorable seasonal and longitudinal conditions, and the presence of RTI triggered by sharp ionospheric density gradients.

This study is significant as it offers valuable insights into:

- Contribution to space-weather modeling in data-sparse regions.
- Enhancement of GNSS accuracy for aviation, surveying, or communications in East Africa.
- Support for regional ionospheric monitoring networks.

By focusing on this unstudied region, the research enhances our understanding of space weather effects on satellite-based technologies, contributing to better planning and resilience of communication and navigation systems in East Africa and beyond.

1.4 Organization of the Dissertation

This thesis includes 7 chapters. The first chapter describes the general introduction of the work, research problem, objective of the thesis. The second chapter provides detail review of the ionospheric dynamics. Chapter 3 provides details of the available data sources, geomagnetic index's and instruments that were used. These include the methods that were used to obtain TEC values from GPS signals. Chapter 4 discuses about study of total electron content variations over the Ethiopia Region Using Kriging technique. Chapter 5 presents the characterization of equatorial plasma bubbles over the East African sector using the ROTI and sTEC depletion depth. Chapter 6 analysis investigation of total electron content responses to equatorial plasma bubbles. Finally, in Chapter 7, conclusions and recommendations made on the possibility of improving techniques to capture TEC variability, TEC modeling techniques, and equatorial plasma bubble structures over East Africa sector.

Chapter 2

Theory and Literature Review

2.1 Introduction

This chapter introduces the solar radiation, ionosphere, equatorial ionization anomaly, and dynamics of the equatorial plasma bubble. It also provides background information on various ionospheric structures, with a particular emphasis on those observed in equatorial and low-latitude regions. By highlighting the distinguishing characteristics and behaviors of equatorial and low-latitude ionospheric regions, this section lays the groundwork for analyzing their role in shaping ionospheric variability and space weather impacts.

2.2 Solar Radiation

The sun is the unique star in our solar system, made of hydrogen and helium, providing light energy to all solar systems planets. It is an enormous ball of extremely hot, largely ionized gas, shining under its own energy. All other objects like stars, planets and moon get there energy from sun, then sun is the source of energy (Fitzpatrick, 2022; Gombosi, 1998; Hargreaves, 1992; Prölss, 2012). The mean distance from the sun to the Earth is one astronomical unit (1AU) and is about 1.5×10^{11} m. The temperature at the solar center is assumed to be as high as 1.5×10^{7} K. At this high temperature protons will be converted to helium nuclei by thermonuclear reactions such as the proton-proton and carbon−cycle chains (Brekke, 2012; Fitzpatrick, 2022; Prölss, 2012). The proton−proton chain can be illustrated as follows:.

$$
\begin{aligned}
1_H + 1_H &\rightarrow 2_H + e^+ + v + 0.42Mev \\
1_H + 2_{He} &\rightarrow 3_H + \gamma + 5.5Mev \\
3_{He} + 3_{He} &\rightarrow 4_{He} + 2^1H + 12.8Mev
\end{aligned}
$$

where e^+, v, and γ represent a positron, a neutrino, and a gamma ray quantum, respectively. We notice that four protons are converted into one helium nucleus while an energy of 24.64 MeV is released. In addition, energy will be released as the positron is annihilated by an electron, and the kinetic energy of the neutrino must also be included. The loss of energy from the sun is due to electromagnetic radiation particle outflow with radiated energy being by far the dominate energy loss process is in table 2.1 below (Schunk and Nagy, 2009).

Table 2.1: Energy and mass loss from the sun

Radiated power	3.8×10^{26} watt
Solar wind power	4.1×10^{20} watt
CME power	7.0×10^{18} watt
Mass loss (Radiation)	4.2×10^{9} kgs^{-1}
Mass loss (particles)	1.3×10^{9} kgs^{-1}

The sun's primary mechanism of energy and mass loss is through radiation as we can observe from table 2.1. Particle loss (solar wind + CMEs) contributes much less, but plays a crucial role in space weather and in shaping the heliosphere.

2.2.1 Solar atmosphere

The heat generated in the sun's interior is transported outward through the solar atmosphere by a combination of radiation and convection. As photons and energetic particles emerge from the inner layers, they are absorbed by the layers just above. These layers then re-emit new photons, which in turn are absorbed and re-emitted by successive layers. Through this continuous process of absorption and emission, radiation energy gradually moves outward, carrying heat from the sun's core to its outer atmosphere. The sun's atmosphere is made up of several layers, mainly the photosphere, the chromosphere and the corona. The photosphere is the lowest layer of the sun's atmosphere the innermost layer we can observe directly. The term photosphere means "sphere of light" and is the layer where most of the sun's energy is emitted. It takes about eight minutes for sunlight from the photosphere to reach Earth (Hargreaves, 1992). In the photosphere, temperature as well as density decreases. In the inner part of the layer, the temperature is about 7,500 K and it decreases to about 4,200 K at the top of the photosphere. It is also the source of solar flares, that extend hundreds of thousands of miles above the sun's surface. Solar flares produce bursts of X-rays, ultraviolet radiation, electromagnetic radiation and radio waves. The second layer of sun is chromosphere. The chromosphere emits a reddish glow as super heated hydrogen burns off. But the red rim can only be seen during a total solar eclipse. The chromosphere may play a role in conducting heat from the interior of the sun to its outermost layer corona. The third layer of the sun's atmosphere is the corona. Like the chromosphere, the sun's corona can only be seen during a total solar eclipse. It is hottest part of the solar atmosphere, where the temperature is fairly uniform and close to 10^6 K (Brekke, 2012). In this region the solar atmosphere is fully ionized. The thermal conductivity in the corona is very high, where hydrogen as well as helium are almost totally ionized. The corona is therefore more or less isothermal at a temperature of close to 10^6 K.

2.3 Atmosphere of the Earth

Atmosphere of the Earth is ocean of gas that envelop the globe, mainly composed of molecular nitrogen (78%), oxygen (21%), carbon dioxide and water with other trace gases (1%). It is divided into four layers such as, troposphere, stratosphere, mesosphere and thermosphere. The temperature of atmospheric layers shows variations with height, it starts decreasing in troposphere, increasing in stratosphere, decreasing in mesosphere and increasing in thermosphere (Brekke, 2012). Therefore, raising and lowering of atmospheric temperature happen due to the existence of absorption and emission of solar radiation in it. EUV and X-ray radiation from the Sun consists of high-energy photons capable of dissociating and ionizing atmospheric species. These processes alter the chemical composition of the atmosphere and lead to significant heating. The resulting thermal energy produces a hot upper region known as the thermosphere, which is less turbulent than the layers below it. Within the thermosphere lies the ionosphere, a region containing free electrons where most ionization occurs. (Hargreaves, 1992).

2.3.1 Layers of Earth atmosphere

Layers of Earth's atmosphere starts at 7 km and ends at around 1000 km above the Earth surface. The first layer is called troposphere, it is the lowest layer of Earth's atmosphere which covers a height from the Earth's surface to about 7 km height at the North and South poles and 17 km high at the equator. It contains 99% of water vapor, which plays a major role in regulating air temperature and temperature decreases with hight, because of emission (Saha, 2008). The troposphere contains about 80% of the total mass of the atmosphere, and the upper boundary is called tropopause, which is the boundary between troposphere and stratosphere (Mohannakumar, 2008). The second layer of the atmosphere is called stratosphere, it extends from the tropopause height of 17 to 50 km to a height of about 50 km and contains about 19% of the atmospheric gases. The stratosphere experiences increasing temperature and solar radiation with height. It contains the ozone layer, because the solar radiation is increasingly absorbed by oxygen molecules in the stratosphere, leading to the formation of ozone. Even if the thickness of the stratosphere layer determined seasonally and geographically in different locations the ozone layer resides in the lower portion of the stratosphere. The boundary between stratosphere and mesosphere is called stratopauses, this boundary separate the stratosphere and the mesosphere. Air plane can fly in this layer (Joshi et al., 2010). Mesosphere is the third layer that have a height 50 km to a height of about 80 to 85 km. It consists less dense gases and the temperature decrease with height, and form the all atmospheric layers this layer is the coldest one. The lower boundary is called stratopause and the upper boundary is called mesopause.

The last layer is known as thermosphere, as the name indicates, thermo means heat, due to this it is the hottest layers. The thermosphere extends from the mesopause height of 85 km to a height of between 1000 km and it is the upper part of atmosphere, where ionosphere is existed because ionized particles are available there.

2.4 The Ionosphere

The Earth's atmosphere includes a wide variety of chemical constituents and is characterized by a significant presence of free electrons and ions. These charged particles are mainly generated through photo-ionization caused by solar radiation, particularly EUV and X-rays. It's important to note that despite the presence of these charged particles, the ionosphere is still mainly composed of neutral atoms and molecules. As shown in Fig. 2.6, even at the point where the electron and ion densities are at their peak, they remain much lower than the density of neutral molecules. This is why the ionosphere is described as a weakly ionized plasma (Schunk and Nagy, 2000). The most abundant neutral constituents in the atmosphere are nitrogen (N), and oxygen (O), as illustrated in Fig. 2.1. These components are largely produced and influenced by photochemical processes, which play a fundamental role in the formation of the ionosphere. These processes determine the ionospheres structure, composition, and its variability over time. Ionosphere is the ionized part of upper atmosphere where free electrons and charged particles are exists (Hargreaves, 1992; Rishbeth and Garriott, 1969). It can be viewed as a variable shell of ionization plasma surrounding the Earth. The range of variability in vertical profiles of the electron density up to altitudes of 1000 km and around. The ionosphere forms primarily due to the interaction between solar radiation and atmospheric gases. Highly energetic ultraviolet (UV) and X$-$ray photons from the sun ionize neutral atoms and molecules in the atmosphere by knocking out electrons, creating free electrons and positively charged ions. The formation of the ionosphere primarily involves three main processes. First, photoionization, driven by solar radiation, ionizes neutral particles in the Earth's atmosphere (Kamide and Chian, 2007). Second, chemical reactions, such as recombination and charge exchange between ions and neutral particles, play a significant role in shaping ionospheric dynamics. Finally, particle precipitation, caused by energetic particles from the solar wind and the magnetospheric region, also contributes to the ionosphere's structure and behavior.

2.4.1 Layers of the Ionosphere

The ionosphere is stratified into noticeable layers based on altitude and electron density. These layers are dynamic and exhibit variations depending on solar activity, time of day, seasons, and geographic location.

- **D-Layer:** This layer has an altitude range of $\sim$ 50 to $\sim$ 90 km, with less ionization than in the E and F-layers. It is the lowest region of the ionosphere and has the lowest electron density. The ionization in this layer is primarily caused by Lyman- radiation and soft X-rays from the Sun (Moldwin, 2022; Ratcliffe, 1972). During the daytime, the D-layer absorbs low-frequency radio waves, leading to signal attenuation. At night, it essentially disappears due to rapid recombination.

- **E-Layer:** The E layer falls within the altitude range of $\sim$ 90 to $\sim$ 150 km. This layers also known as the Kennelly-Heaviside layer, has moderate electron density (Kelley, 2009). The ionization sources are solar UV radiation, ionizes molecular oxygen and nitrogen (Brekke, 2012). It reflects medium-frequency radio waves and supports shortwave radio communication.

- **F- Layer:** The F-layer is the most significant and complex layer of the ionosphere, consisting of two sublayers during the day:

- **F1-Layer:** Occurs at lower altitudes (150-250 km) and is present only during the daytime.

- **F2-Layer:** Is the main ionospheric layer (250-500 km), it persists during both day and night and has the highest electron density. The F-Layer is crucial for high-frequency (HF) radio communication and satellite-based navigation systems. The formation of the F-Layer is mainly due to the ionization of oxygen atoms by solar extreme UV radiation (Baumjohann and Treumann, 2012; Hargreaves, 1992).

  Ionosphere is also classified based on its composition. The ionic composition of the ionosphere is shown in Fig. 2.1 and Table 2.2. The molecular ions O_2^+ and NO^+ dominate in the lower ionosphere, which is certainly surprising for the case of the NO^+ ions. In the region of the maximum and in the upper ionosphere, the primary ion is O^+, which seems reasonable in view of the dominance of thermospheric atomic oxygen in this region. Again surprising are the absence of larger He^+ densities and the direct transition from $O^+$to H^+ as primary ion in the upper ionosphere (Jursa, 1985). The lower region of the ionosphere dominated by O_2^+ and NO^+ ions is denoted the E-region; the atomic oxygen ion region above this is called the F-region. Continuing upward, we come to the region of dominant H^+ ions, the protonosphere or plasmasphere, which, perhaps somewhat arbitrarily, is not considered as part of the ionosphere.

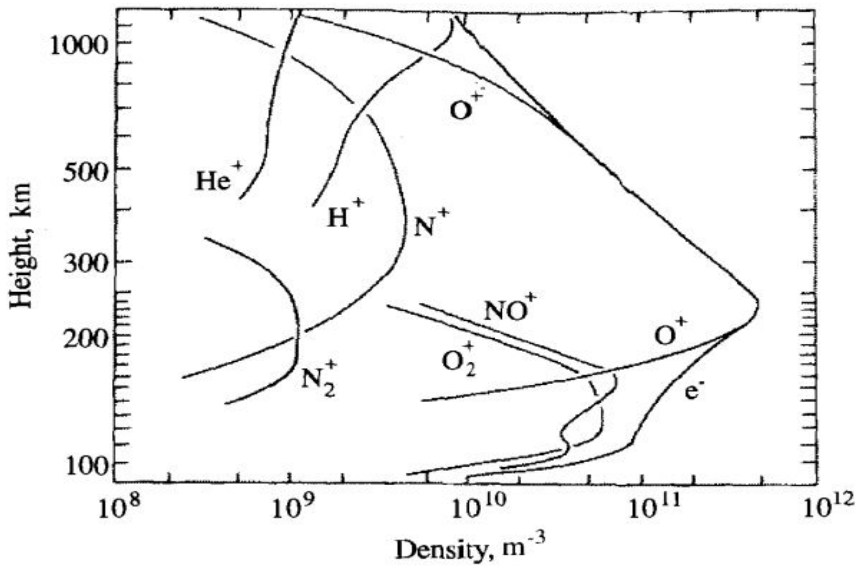

Figure 2.1: The composition of the ionosphere as observed during the day at mid-latitudes for low solar activity (Jursa, 1985)

Table 2.2: Classification of the ionosphere according to composition

Ionosphere	D-region	$\lambda < 90$ km	$H_3O^+, (H_2O)n, N_O3^-$
	E-region	$90 < \lambda < 170$km	O^+, N_O^+
	F-region	$170 < \lambda < 1000$ km	O^+
Plasmasphere	Beyond F-region	$\lambda > 1000$km	H^+

2.4.2 Types of Ionospheric Variations

The structure of the ionosphere at any given location is complex because the intensity of EUV radiation from the sun varies across different wavelengths. This variation depends on the type of atom emitting the radiation. The height and structure of the ionosphere change based on several factors, including the time of day, season, geographic and geomagnetic location, and solar activity (Brekke, 1998). The ionosphere is a dynamic and unstable region that experiences both predictable (periodic) and unpredictable (random) variations over short time scales. Periodic changes include daily (diurnal) and seasonal variations, while random variations are mostly driven by solar and geomagnetic activity. One important measurement used to monitor ionospheric behavior is GPS-derived TEC, which shows significant day to day variability (Brekke, 1998; Kockarts, 1981; Rao et al., 2013). This variability affects the accuracy and reliability of GPS based communication, forecasting and navigation systems. The main factors contributing to GPS-TEC variability are: changes in solar activity and the intensity of solar radiation reaching Earth, the angle at which solar radiation enters the Earth's upper atmosphere, and fluctuations in Earth's magnetic field, the strength of the EEJ, which impacts the behavior of the EIA and North-south (meridional) neutral winds, which influence the distribution of ionized particles. Additionally, daily changes in GPS-TEC can also be caused by the movement of ionized particles across the geomagnetic field due to tidal winds. The ionosphere is highly dynamic and experiences various types of variations due to several influencing factors:

2.4.2.1 Diurnal Variations

As we can observe form Fig 2.2, diurnal variations occurs due to the Earth's rotation, leading to alternating periods of solar radiation day and night. During the day, UV and X-ray radiation ionize atmospheric gases, increasing electron densities across all ionospheric layers. At night, in the absence of sunlight, ionization decrease, and the layers begin to recombine, significantly reducing electron densities. The D-layer disappears at night, leading to reduced absorption of low-frequency waves but F2 layer remains active at night due to slower recombination rates at higher altitudes (Pyšek and Richardson, 2010).

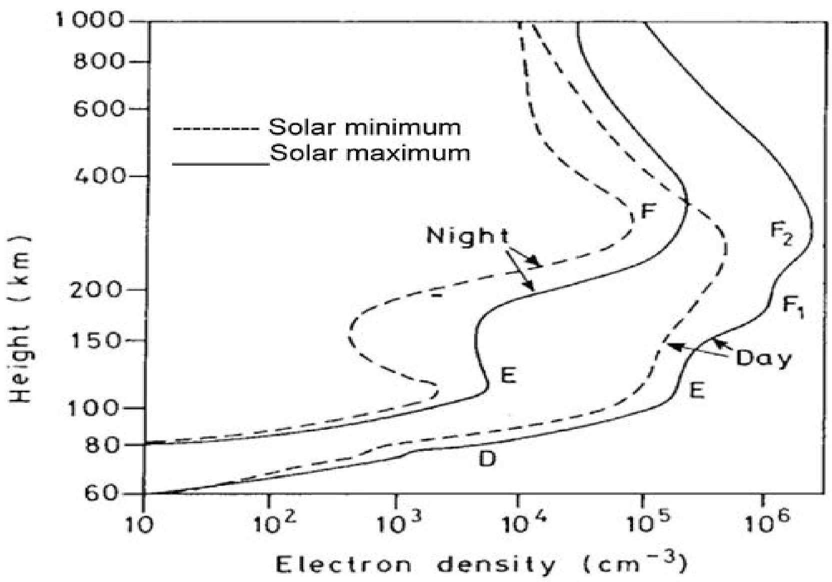

Figure 2.2: Representative electron density profiles of the ionosphere during daytime and nighttime across different phases of the solar cycle. Solid lines indicate conditions during solar maximum, showing significantly higher electron densities, particularly in the F2 layer. Dashed lines represent solar minimum, with reduced ionization throughout the profile. Daytime profiles exhibit well-defined D, E, and F layers, while nighttime profiles show diminished lower layers and a reduced, though persistent, F2 layer (Hunsucker and Hargreaves, 2007)

2.4.2.2 Seasonal Variations

The seasonal variation of the ionosphere is affected by changes in the solar zenith angle, which shifts as the Earth orbits the Sun. When the Sun is directly overhead, the solar zenith angle is at its lowest, resulting in maximum photo ionization during summer, the solar zenith angle at noon is smaller than in winter, leading to higher electron densities in the D, E, and F-layers. Consequently, these layers are more pronounced in summer compared to winter (Brekke, 2012). The seasonal variations of ionospheric TEC are due to the earth's tilt and rotation around the Sun; the relative position of the Sun moves from one hemisphere to the other with the seasonal variation of solar zenith angle and radiation intensity at any given geographical location (Woldemariam and Gogie, 2024). Months in a year conventionally often grouped into four seasons, these are December solstice (November, December, and January), March equinox (February, March, and April), June solstice (May, June, and July) and September equinox (August, September, and October). In general, the maximum electron density and the TEC of the daytime F-region are higher in March equinox and September equinox at low latitude.

2.4.2.3 Latitudinal Variation

The Earths ionosphere is not uniform and is mostly concentrated on the side of the planet facing the sun. As a result, it shows noticeable variation with latitude. Near the equator, the ionospheric density tends to be higher because the suns rays hit this region more directly, meaning the solar zenith angle is at its approach to zero. As you move toward higher latitudes, the suns UV radiation hits the atmosphere at a more slanted angle, decrease the intensity of solar energy. This leads to a minimum in ion production, or photo ionization, as you close the poles. Based on geomagnetic latitudes, the ionosphere can be characterized broadly into the low-latitude, mid-latitude and high-latitude ionospheres (Zolesi and Cander, 2014).

At equatorial latitudes, between $\pm 20^\circ$ of the magnetic equator, the ionosphere shows unique behavior, most notably the EIA. Here, the electron density is lower directly at the equator and higher at about $\pm 15^\circ$ magnetic latitude, forming two ionization crests. This is due to the fountain effect, where the ionized plasma is lifted by an upward $E \times B$ drift and redistributed along magnetic field lines to higher latitudes. The equatorial ionosphere is highly dynamic, with strong diurnal variations and frequent irregularities such as equatorial spread-F, which can severely affect radio signals and GPS accuracy.

At mid-latitudes, from ±20° to ±60°, the ionosphere becomes more stable and predictable. This region experiences moderate levels of ionization and is less affected by the geomagnetic disturbances typical of polar regions. Seasonal and diurnal variations are evident, with higher electron densities during the daytime and summer months(Sibanda and McKinnell, 2011). The F_2 layer in mid-latitudes often exhibits peak ionization during the day and slowly decays at night. Although generally more stable, mid-latitude regions can experience traveling ionospheric disturbances ($TIDs$) caused by atmospheric gravity waves.

At high latitudes, beyond ±60° magnetic latitude, the ionosphere is highly influenced by solar wind and magneto-spheric interactions. The auroral and polar cap regions are characterized by significant spatial and temporal variability, due to phenomena such as particle precipitation, which enhances ionization. This region often experiences polar cap patchesdense blobs of plasma drifting across the polar sky and ionospheric troughs, where electron density decreases significantly during the night(Kelley, 2009). Irregularities and scintillations are frequent, particularly during geomagnetic storms, which can lead to communication outages and GPS errors.

Generally, the ionospheric electron density and structure vary substantially with latitude. Equatorial regions are dominated by electrodynamic processes like the fountain effect and plasma drift, mid-latitudes show more stable and gradual variations, and polar regions are subject to dynamic space weather influences (McNamara, 1991). The Earths magnetic field geometry, which is horizontal at the equator and vertical at the poles, plays a key role in shaping these latitudinal patterns. Understanding these variations is critical for improving ionospheric models, enhancing communication systems, and mitigating the impacts of space weather on technological infrastructure.

Sunspot Number (SSN)

Sunspots are cooler regions on the suns surface that appear as dark spots due to their lower temperatures compared to the surrounding areas. The SSN, which counts individual sunspots and groups of sunspots, serves as a key indicator of solar activity. This number fluctuates in accordance with the 11-year solar cycle, reflecting the dynamic nature of the Sun's magnetic behavior over time (Dieminger et al., 2012). Sunspots are relatively cooler regions on the suns surface that appear as dark spots due to their lower temperatures compared to the surrounding photosphere. This number fluctuates in accordance with the 11-year solar cycle, increasing during solar maximum and decreasing during solar minimum. The SSN can be expressed using the following equation:

$$R = k(10g + s) \tag{2.1}$$

where R is sunspot activity, K is an observatory scaling factor (always < 1), g is the number of sunspot groups on the solar disk, and s is the total number of individual spots.

Solar radio flux (F10.7 cm)

Solar radio flux, most commonly represented by the F10.7 index, is a key measure of solar activity that has been observed daily since 1947. It refers to the intensity of the sun's radio emission at a wavelength of 10.7 cm and frequency of 2800 MHz. It is expressed in solar flux units (sfu), where $1suf = 10^{-22}Wm^{-2}Hz^{-1}$ (D'ujanga et al., 2016; Opio et al., 2015). These emissions originate from the upper chromosphere and lower corona of the sun. The F10.7 index serves as a reliable proxy for solar UV and EUV radiation, which are more difficult to measure directly but are important for understanding the Earths ionosphere, thermosphere, and space weather conditions (Tapping, 2013). F10.7 is widely used in space weather probing because it closely tracks the solar cycle and correlates strongly with other indicators of solar activity, such as SSN, solar irradiance, and geomagnetic activity. As figure 2.3 shows us, during periods of low solar activity (solar minimum), the F10.7 values can drop below 70 sfu, while during solar maximum, they often exceed 200 sfu and can reach over 300 sfu. Since it is not significantly affected by the Earths atmosphere or weather, F10.7 provides a consistent and uninterrupted dataset that is essential for forecasting satellite drag, radio signal propagation, and GPS signal quality.

2.4.2.4 Kp index

The Kp index is a globally recognized geomagnetic index introduced by Julius Bartels in 1938, designed to quantify the level of geomagnetic activity over the entire Earth in 3-hour intervals based on UT. It is derived from the standardized local K indices (Ks) recorded at geomagnetic observatories globally and has become frequently used of all geomagnetic indices (Mayaud, 1973). It is determined by identifying the largest range of variation in the magnetic field components specifically X, Y, D, or H, depending on the representation system. These components can be expressed either as XYZ (geographic components) or HDZ (horizontal, declination, and vertical components) (Campbell, 2003). The index ranges from 0 to 9, where 0 indicates extremely quiet geomagnetic condi-

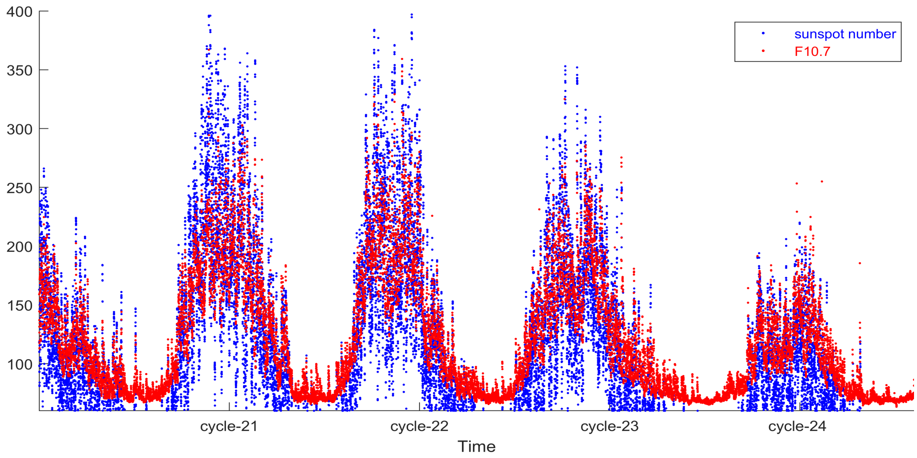

Figure 2.3: The yearly mean sunspot number and solar radio flux (F10.7) for the last four solar cycles (source author)

tions, and 9 corresponds to severe geomagnetic storming, making it a important tool in space weather monitoring and forecasting process.

Table 2.3: Kp-index values and typically represent in terms of geomagnetic activity.

Kp-Index values	Level of Activity
0	Quiet
1	Quiet
2	Quiet
3	Unsettled
4	Active
5	Minor Storm
6	Moderate Storm
7	Strong storm
8	Severe Storm
9	Extreme Storm

2.4.2.5 Dst index

The Dst index is a key in space weather studies to quantify geomagnetic activity and assess the intensity of geomagnetic storms. It gives valuable insight into the strength and properties of the ring current, a major component of Earth's magnetosphere that significantly impacts the planet's magnetic environment. During geomagnetic stormsoften triggered by disturbances from solar events such as coronal mass ejections $(CMEs)$ or high-speed solar wind streams-charged particles such as solar protons and electrons are injected into the near-Earth space environment. These particles are trapped in the Earth's magnetosphere, forming a circular flow around the planet known as the ring current. The ring current generates its own magnetic field, which opposes Earth's magnetic field.

If the intensity of the ring current increases, it effectively reduces the overall strength of the Earth's magnetic field, particularly near the equator. This reduction is precisely what the Dst index measures.

The Dst index is expressed in nano-tesla (nT), with negative values indicating a weakening of the Earth's magnetic field. The more negative the Dst value, the more intense the magnetic disturbance. Therefore, the Dst index serves as a direct indicator of the severity of geomagnetic storms.

Table 2.4: Classification of Geomagnetic Storms Based on Dst Index Values.

Dst values	storm types
0-30	Quiet to Weak
-30 to -50	Moderate
-50 to -100	Strong
>-100	Severe

2.4.3 The Influence of the Ionosphere on Radio Waves

The influence of the ionosphere on radio waves is multifaceted, encompassing reflection, refraction, absorption, scattering, and time delay. These effects are important for long-distance communication and satellite navigation. One of the most crucial effects of the ionosphere is its ability to reflect and refract radio waves. The ionospheres refractive properties permit radio waves to skip between the ionosphere and the Earths surface, extending their range beyond the horizon. However, the effectiveness of this reflection depends on the frequency of the wave and the ionization levels in the ionosphere, which vary with time of day, season, and solar activity (Basu et al., 2002; Ratcliffe, 1972).

In addition to reflection and refraction, the ionosphere can absorb radio waves, particularly at lower frequencies. The D region, the lowest layer of the ionosphere, is primarily responsible for this absorption due to collisions between free electrons and neutral particles. During the daytime, increased solar radiation enhances ionization, leading to higher absorption rates and reduced signal strength for low frequency waves (Basu et al., 2002; Klobuchar, 1987). This absorption effect diminishes at night when ionization levels decrease, allowing for improved propagation of these frequencies. The ionospheres irregularities also influence radio waves by causing scattering and signal degradation. Small-scale fluctuations in electron density, often referred to as plasma irregularities, can scatter radio waves, leading to phenomena such as scintillation and fading. Scintillation is particularly common in equatorial and polar regions, where the ionosphere is more dynamic. This effect can disrupt satellite communication and navigation systems, including GPS, by introducing rapid fluctuations in signal strength and phase. Engineers often employ dual frequency systems and predictive modeling to mitigate these disruptions and enhance signal reliability (Hargreaves, 1992).

Another significant impact of the ionosphere on radio waves is the introduction of time delays and dispersion. As radio waves travel through the ionosphere, their group velocity decreases due to interactions with free electrons. This effect, known as ionospheric delay, is particularly pronounced for trans-ionospheric signals such as those used by GPS and other satellite based systems. Dispersion, where different frequencies travel at slightly different speeds, further complicates signal transmission. These delays can affect the accuracy of positioning and timing systems, making ionospheric correction models an essential component of modern satellite navigation.

2.4.4 Ionospheric Scintillation

Ionospheric scintillation is the rapid fluctuations in the amplitude and phase of radio signals occurred by irregularities in the Earth's ionosphere. These irregularities result from variations in electron density within the ionospheric plasma, leading to signal scattering and distortion (Davies and Hartmann, 1997). The phenomenon is particularly frequent in equatorial and low-latitude regions, with its intensity influenced by factors such as solar activity, geomagnetic storms, and the 11-year solar cycle (Aarons, 1997). Scintillation events are more recurring during the post-sunset hours in equatorial regions, where EPBs form due to the Rayleigh-Taylor instability. These large-scale depletions in electron density are the primary drivers of scintillation in low-latitude regions. Similarly, geomagnetic storms, often triggered by solar flares and coronal mass ejections, induce disturbances that aggravate scintillation activity (Hernández-Pajares et al., 2011).

Scintillation is typically characterized by two metrics: the amplitude scintillation index (S_4), which measures signal intensity fluctuations, and the phase scintillation index ($\delta\phi$), which quantifies variations in signal phase. The amplitude scintillation index can be expressed by:

$$S_4 = \sqrt{\frac{< I^2 > - < I >^2}{< I >^2}} \tag{2.2}$$

where I is the average power of the incoming signals. On the other hand phase scintillation index is given by:

$$\delta_\phi = \sqrt{< \phi^2 > - < \phi >^2} \tag{2.3}$$

where ϕ is the phase of signals in degree. These index have significant impacts on satellite communication and navigation systems, such as GNSS, causing signal degradation, loss of lock on satellites, and increased positioning errors. To mitigate these impacts, researchers employ various strategies, including real-time monitoring of ionospheric conditions using GNSS networks and ionosondes, as well as predictive modeling to forecast scintillation events (Coster and Komjathy, 2008). Error correction algorithms, signal processing techniques, and the use of multiple-frequency systems also help reduce the adverse effects of scintillation.

The study of ionospheric scintillation is important for improving the reliability of satellite-based communication and navigation systems. Research efforts focus on understanding regional and temporal variations in scintillation, with advanced measurement techniques such as dense GNSS networks and space-based observations providing valuable insights. Predictive models that integrate data from solar activity, geomagnetic indices, and ionospheric measurements are instrumental in forecasting scintillation events (Rezende et al., 2010). In regions like the East African sector, where unique ionospheric dynamics prevail, detailed characterization of scintillation is essential for developing region-specific mitigation strategies. As reliance on satellite technology grows, understanding and managing ionospheric scintillation remain vital for ensuring robust and reliable global communication and navigation systems.

2.4.5 GPS signal propagation in the ionosphere

GPS is a satellite-based navigation system that provides users with real-time position, velocity, and timing information anywhere on the Earth's surface. It's developed by the United States Department of Defense for military purposes. GPS has become an important tool in various civilian applications like navigation, surveying, remote sensing, geodesy, and atmospheric studies Kaplan and Hegarty (2006). It can be classified into three segments: the space segment, control segment, and user segment. The space segment includes a constellation of at least 24 Medium Earth Orbit (MEO) satellites, each transmitting radio signals with information about the satellite's position and the precise time of transmission. The control segment consists of ground stations that monitor the health and status of the satellites, update their navigation messages, and ensure system integrity. The user segment includes receivers that use signals from multiple satellites to calculate their position Misra and Enge (2011). GPS receivers determine position by measuring the time it takes for signals from at least four satellites to reach them. This time delay is used to calculate the distance from each satellite, allowing the receiver to determine its location in three-dimensional space and synchronize its clock. However, the accuracy of GPS can be affected by various factors such as atmospheric delays, particularly in the ionosphere and troposphere, multi-path effects that means signal reflections from surfaces, and satellite clock or orbital errors. It has a wide range of applications in both scientific and practical domains. In geosciences, it is used to monitor tectonic plate movements and earthquake activity. In meteorology and space weather, GPS signals help analyze ionospheric TEC and atmospheric water vapor distribution. Also, in modern society, GPS plays vital role in transportation, agriculture, disaster management, and mobile technology. Each GPS satellite transmits the same two L-band signals at frequencies $f_1 = 1.5754$ GHz and $f_2 = 1.2276$ GHz. Pseudo-Random Noise (PRN) codes and navigation message are modulated on the signals and transmitted by the GPS satellite. As GPS signals travel through the ionosphere, their behavior is significantly changed due to the dispersive nature of the medium. The group velocity (associated with the code or pseudo-range measurements) experiences a delay, while the phase velocity (related to the carrier signal) undergoes an advance compared to their velocities in a vacuum. This contrasting effect introduces a measurable discrepancy between the code and carrier signals. Consequently, the ionosphere becomes one of the primary sources of error in GPS positioning and timing applications, particularly for single-frequency receivers. The group and phase velocities of the GPS signal are given by:

$$V_g = \frac{c}{n_g} = \frac{c}{\left(1 + \frac{e^2 N}{8\pi^2 \epsilon_o m f^2}\right)} \tag{2.4}$$

$$V_\phi = \frac{c}{n_\phi} = \frac{c}{\left(1 - \frac{e^2 N}{8\pi^2 \epsilon_o m f^2}\right)} \tag{2.5}$$

The transit time of the GPS code signal differs depending on the medium through which it travels. In a vacuum, the code propagates at the speed of light, and the total travel time is expressed as $t_v = \int \frac{ds}{c}$ where ds is an infinitesimal segment along the signal path and c is the speed of light in free space. However, when the signal passes through the ionosphere, it experiences a reduction in group velocity due to the presence of free electrons. The corresponding travel time in the ionized medium becomes becomes $t_I = \int \frac{ds}{v_g}$, where v_g is the group velocity in the ionosphere. The ionospheric time delay of the code signal is then the difference between these two integrals, quantifying the extra time the signal takes to traverse the ionosphere compared to free space. The group velocity $v_g$of a radio signal in a plasma (ionosphere) is less than the speed of light c, causing the signal to be delayed. The time delay of the code signal in the ionosphere compared to free space is:

$$\Delta t = \int_s \left(\frac{1}{v_g} - \frac{1}{c}\right) ds \tag{2.6}$$

Where: s is the signal path, v_g is the group velocity in the ionosphere,c is the speed of light in vacuum. The group velocity of an electromagnetic wave in a plasma is given by:

$$v_g = c\left(1 - \frac{f_p^2}{2f^2}\right) \tag{2.7}$$

Where f_p is the plasma frequency given by $f_p = 8.98 \times 10^3\sqrt{Ne}$ with Ne in electrons/m^3 and f is the frequency of the GPS signal. Assuming $f_p << f$, we substitute and simplify:

$$\Delta t = \int_s \frac{f_p^2}{2cf^2} ds \tag{2.8}$$

Substitute $f_p^2 = 80.6 \times N_e$

$$\Delta t = \frac{40.3}{f^2}\int_s N_e(s)ds \tag{2.9}$$

Δt is ionospheric time delay (in seconds), and $TEC = \int_s N_e(s)ds$. Then the final formula of ionosphere time delay is given by:

$$\Delta t = \frac{40.3}{f^2}.TEC \tag{2.10}$$

2.4.6 Radio wave propagation in the ionosphere

The effect of the ionosphere can be described by characterizing its radio wave reflecting capability. The ability of the ionosphere in refracting a radio wave is given by Appleton-Hartree equation. According to Hunsucker and Hargreaves (2007) the refractive index, n, of an ionized propagation medium is given by

$$n^2 = \left(1 - \frac{X}{1 - jZ - \frac{Y_T^2}{2(1-X-iZ)}}\right) \pm \left(\frac{Y_T^4}{4(1-X-iZ)^2} + Y_L^2\right)^{\frac{1}{2}} \tag{2.11}$$

where $X = \frac{Ne^2}{\epsilon o m\omega^2}$, $Y_L = \frac{eB_L}{m\omega}$, $Y_T = \frac{eB_T}{m\omega}$, $Z = \frac{V}{\omega}$, N is the electron density, e is the electron charge, m is the electron mass ϵo is the permittivity of free space, ω is the angular frequency of the wave and V is the electron collision frequency. The plus and minus sign in equation 2.11 correspond to the ordinary and extraordinary waves, respectively. When a radio wave propagates perpendicular to the geomagnetic field, the electric field of the wave has a component along the direction of the geomagnetic field, causing the free electrons in the ionosphere to move along the field lines. In this scenario, the electrons are accelerated primarily by the electric field of the wave, and since the magnetic force is perpendicular to both the velocity of the electrons and the magnetic field, it does not significantly influence the electrons motion along the magnetic field lines. As a result, the electrons move parallel to the geomagnetic field without feeling a strong magnetic force, allowing them to drift along the field without significant interference from the geomagnetic field. This interaction highlights the dominance of the electric field in driving electron motion along the magnetic lines in this particular orientation.

2.4.7 Ionization and Recombination

The electron density in the ionosphere results from a dynamic balance between ionization, the process by which solar radiation generates ions and free electrons, and recombination, where these charged particles merge back into neutral atoms (Kelley, 2009). Ionization occurs exclusively during the daytime, as it requires solar X-rays and EUV radiation (Schunk and Nagy, 2009), while recombination occurs continuously, both day and night. As a result, ionospheric electron and ion concentrations peak during the day and gradually decline overnight, reaching a minimum just before sunrise (Hargreaves, 1992). As we can see from figure 2.4 ions are created in the atmosphere by high energy solar radiation, and EUV. Electrons are separated from atoms to create a positively charged ion and a free electron. When the two recombine a neutrally charged atom is again constituted. Solar radiation ionizes var-

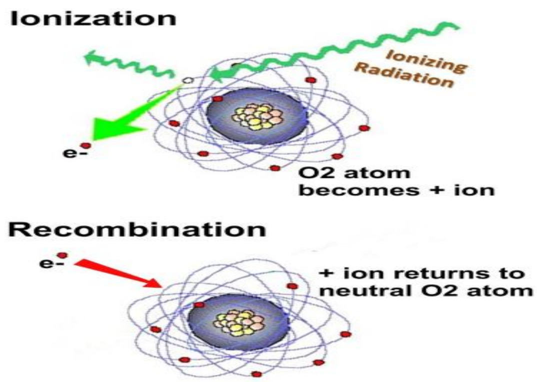

Figure 2.4: Attachment and detachment of electrons to/from atoms and molecules (https://www.hamradioschool.com/post/d-layer-absorption)

ious atmospheric species, primarily molecular oxygen (O), nitric oxide (NO), atomic oxygen (O), atomic nitrogen (N), hydrogen (H), and helium (He). Recombination of electrons and ions reduces free electron density, making it a major electron loss process. In the upper ionosphere, where the atmospheric density is extremely low, diffusion becomes a dominant mechanism. Electrons and ions drift into adjacent altitude layers, often resulting in greater electron loss through diffusion than recombination (Kelley, 2009). However, diffusion can also lead to electron gain if charged particles migrate into a region from higher or lower layers. Thus, the interplay of ionization, recombination, and diffusion collectively defines the electron density structure of the ionosphere.

2.4.8 Chapman production function

The Chapman production function gives the rate of electron production per unit volume at a given height h and is expressed as:

$$q = q_{m,0} exp \left[-secX exp \left(-\frac{z - z_m, 0}{H} \right) \right] \tag{2.12}$$

The height of maximum ion production in the ionosphere is strongly influenced by the position of the sun, specifically the solar zenith angle, which is the angle between the sun and the vertical direction (Schaer and helvétique des sciences naturelles. Commission géodésique, 1999). When the sun is directly overhead (i.e., at a zenith angle of zero degrees), solar radiation travels the shortest possible path through the atmosphere, allowing the solar photons to penetrate deeper before being absorbed. As a result, the maximum ionization occurs at a lower altitude, referred to as the minimum height of maximum production $(z_m, 0)$ (Chapman, 1931). However, as the zenith angle increases (i.e., the s un moves away from the vertical and approaches the horizon), the path length of solar radiation through the atmosphere increases proportionally to the secant of the zenith angle $(secX)$. This longer path causes

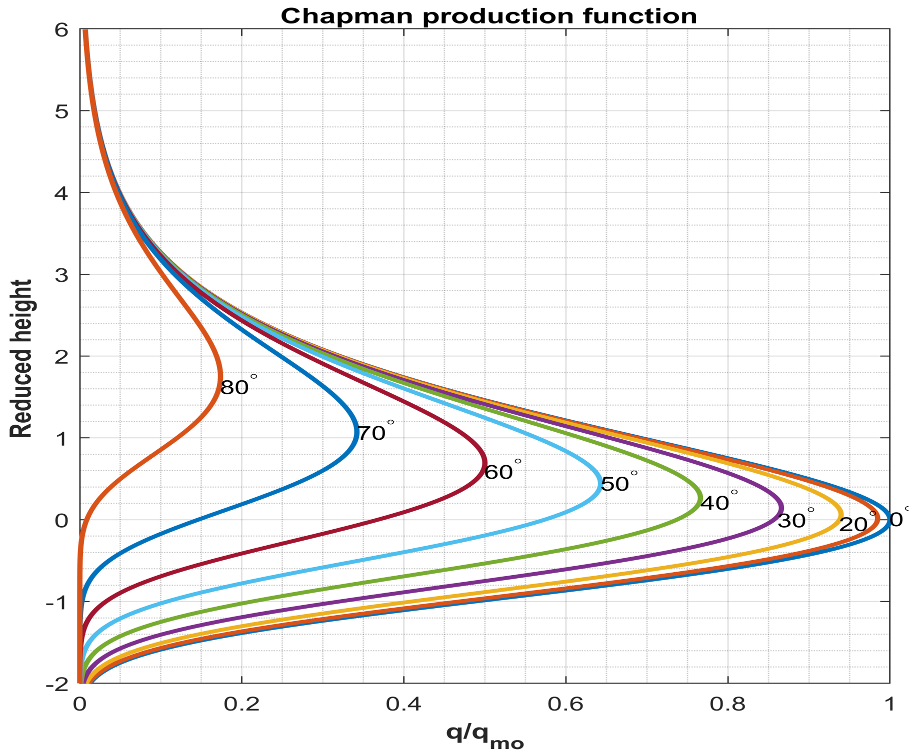

Figure 2.5: Chapman production profiles for different solar zenith angles.

solar energy to be absorbed higher up in the atmosphere. Consequently, the height at which maximum ionization occurs also increases. This relationship is mathematically described by the Chapman production function, which models the ionization profile as a function of solar radiation and atmospheric density. Figure 2.5 illustrates the ionization profiles for different zenith angles between 0 and 80. At a solar zenith angle of zero degrees,that means when the Sun is directly overhead, the Chapman production function reaches its maximum value, and the ionization peak occurs at the lowest possible height (Brekke, 2012).

2.4.9 Ionospheric Conductivity

Ionospheric conductivity varies significantly with altitude, latitude,longitude, time and is especially active in the E-region. This region is often referred to as the E-region dynamo, where electric fields and currents are generated due to interactions between neutral winds, the geomagnetic field, and charged particles (Walt, 1994). The conductivity in the ionosphere arises from the motion of charged particles in the presence of the Earth's magnetic field and frequent collisions with neutral particles. These collisions affect how freely particles can move, and therefore, how well the ionosphere conducts electricity. Ionospheric conductivity is strongly dependent on space (altitude, latitude, longitude), time (diurnal, seasonal variations, annual), and solar activity (sunspots, flares, solar EUV and X-rays). There are three primary types of ionospheric conductivity, each corresponding to different directions relative to the Earth's magnetic field and the electric field. These are Pedersen, Hall and Parallel conductivity (Zalesak et al., 1982). To calculate conductivity, we start with the force balance equations for electrons and ions in the ionosphere. In the absence of pressure gradients, and assuming no acceleration, the motion is governed by the following equation:

$$m_s \nu_s v_s = q_s (E + v_s \times B) \tag{2.13}$$

Where

- m_s =mass of species
- q_s = charge of species
- v_s = collision frequency
- ν_s = drift velocity
- E = electric field
- B = magnetic filed

By calculating those equations separately for electrons and ions we get conductivity expressions. Parallel Conductivity(σ_o): This occurs along the magnetic field, where the Lorentz force component is zero.

$$\sigma_o = \frac{n_e e^2}{m_e v_e} \tag{2.14}$$

Where

- n_e =electron density
- e = electron charge
- m_e = electron mass
- v_e = electron-neutral collision frequency

This conductivity is highest because electrons move freely along the magnetic field with minimal deflection. Pedersen Conductivity (σP): This occurs in the direction of the electric field but perpendicular to the magnetic field.

$$\sigma P = \frac{n_e e^2}{m_e} . \frac{v_e}{v_e^2 + \omega_{ce}^2} \tag{2.15}$$

Hall Conductivity (σH): This occurs perpendicular to both electric field and magnetic field.

$$\sigma H = \frac{n_e e^2}{m_e} . \frac{\omega_{ce}^2}{v_e^2 + \omega_{ce}^2} \tag{2.16}$$

2.4.10 The recombination process

The newly created ionization quickly undergoes chemical reactions to restore the ionospheric equilibrium that existed prior to ionization. Additionally, a portion of the ionized particles is redistributed through transport processes, including diffusion, neutral atmospheric winds, and the influence of electric fields. The time rate of change in electron density at any given altitude h is described by the continuity equation.

$$\frac{dN_e}{dt} = q - L(N_e) - div(N_e V) \tag{2.17}$$

where
N_e = electron density
q = electron production rate due primarily to photo-ionization
L= electron loss rate through recombination

$div(_e)$ = electron loss rate due to diffusion
div = the vector divergence operator

V = electron drift velocity
In the ionosphere electron drift in the vertical direction is far greater than horizontal drift, allowing the divergence operator to be replaced by d/dh. Making this simplification the continuity equation becomes

$$\frac{dN_e}{dt} = q - L(N_e) - \frac{d(N_eV_h)}{d_h} \tag{2.18}$$

where
V_h = electron drift velocity in the vertical direction. This equation states that over time the change in electron density (N_e) at any given altitude h is equal to

- The rate of electron production (q)
- Minus electron loss due to recombination (L)
- Minus electron loss due to electrons diffusing to a higher or lower altitude $\frac{d(N_eV)}{d_h}$

By neglecting the transport term and assume photochemical equilibrium

$$q = L$$

Let us further assume that electrons (e) recombine directly with positive ions X^+ to form a neutral species together with an accompanying radiation of a photon, hv the so-called radiative recombination process.

$$X^+ + e \longrightarrow X + hv$$

Another possibility for reducing the number of free electrons is by dissociative recombination of a molecule XY^+ as follows:

$$XY^+ + e \longrightarrow X + Y$$

The radiative recombination process or the dissociative recombination process is dominant, we will in both cases for simplicity assume charge neutrality so that the number density of positive ions X^+ or XY^+ are equal to the number density ne of free electrons, that means $X^+ = n_e$ or $XY^+ = n_e$. The loss rate will be proportional to the product of the electron and ion densities (Brekke, 2012). The proportionality factor α is called the "recombination coefficient", thus

$$L = \alpha n_e^2/300\ .\ 3$$

2.5 Growth rate of the RTI due to gravity

The RTI instability occurs at the interface between two fluids of different densities when a heavier fluid is positioned above a lighter one in the presence of a gravitational field. This configuration is inherently unstable. Even small perturbations at the interface allow gravity to act on the heavier fluid, pulling it downward while the lighter fluid rises to take its place. This results in an interpenetration of the two fluids, leading to complex mixing patterns. Figure 2.6 illustrates the classical and simplified configuration commonly used to study this instability. The phenomenon has been extensively studied since the foundational works of RTI instability (Getahun et al., 2022). The primary driver of RTI is gravity acting on an inverted density gradient specifically, when a heavier fluid is supported by a lighter one. In this setup, gravity acts downward, opposite to the direction of the density gradient, while the magnetic field is oriented horizontally (into the page), as shown in Figure 2.6. When a small perturbation occurs in this system, an electric field $\overrightarrow{E}$ is generated due to the $\overrightarrow{g} \times \overrightarrow{B}$ interaction. This leads to $\overrightarrow{E} \times \overrightarrow{B}$ plasma drifts upward in regions of low plasma density and downward in regions of high density. As a result, low-density plasma moves upward and high-density plasma moves downward, amplifying the initial disturbance and triggering instability.

In the ionospheric context, the lighter fluid is the low-density plasma, which carries a gravity-driven current. This current produces a $\overrightarrow{J} \times \overrightarrow{B}$ force that helps support the plasma, preventing it from simply falling under gravity. Furthermore, the development of equatorial spread-F (ESF) can also be influenced by other factors, such as the breaking of gravity waves rising from lower altitudes, and by electric field disturbances originating from high latitudes during geomagnetically active periods. The current $(\overrightarrow{J})$ due to gravitational gradient is given by

$$\overrightarrow{J_x} = \frac{nMg}{B} = \frac{nMg \times B}{B^2} \tag{2.19}$$

The velocity of ion (V_i) due to electric and gravitational filed is given by:

$$V_i \perp = \frac{1}{1+k_i^2} w_i \perp + \frac{k_i}{1+k^2 i} wi \perp \times B \tag{2.20}$$

Where, $w_i = \frac{q}{Miv_{in}} E - Di\frac{\Delta n}{n} + \frac{\delta}{v_{in}}$. The system is unstable when g and ∇n are oppositely directed. The velocity of electron is given by

$$V_e = \frac{E \times B}{B} + \frac{kbTe}{enB^2}(\Delta E \times B) - \frac{meVen}{eB^2} g \times B \tag{2.21}$$

In the F-region, $k_i >> 1$, and the term $1 + k^2 i \approx k^2 i$, then the velocity of ion can be written in the from of

$$Vi \perp = \frac{1}{k^2 i} wi \perp + \frac{1}{ki} wi \times B \tag{2.22}$$

Inserting wi into the above equation and rearranging

$$V_i \perp = \frac{eE}{K^2 i m_i v_{in}} + \frac{g}{v_{in} k^2 i} - \frac{D_i}{k^2 i}(\frac{\Delta n}{n}) + \frac{E \times B}{B^2} + M(\frac{g \times B}{eB^2}) - \frac{kbT_i}{enB^2}(\Delta E \times B) \quad (2.23)$$

From equation (3) $g \times B$ term can be zero because m_e is small, in the same way equation (5) 2nd and 3rd terms are small due to $k_i >> 1$, then $n_i = n_e = n$. The $E \times B$ terms are identical for ions and electrons, therefore no current flow, then the current is given by

$$J = ne(V_i - V_e) \quad (2.24)$$

Using this term for velocity and yields

$$J = \frac{ne^2}{k^2 imv_i} E + \frac{ne}{\Omega} g \times B - \frac{Kb}{B^2}(T_i + T_e)(\Delta \times B) \quad (2.25)$$

Where, $\Omega = \frac{eB}{m}$. The ion continuity equation at the F-region during post sun set is given by

$$\frac{\partial n}{\partial t} + V.\Delta n + n(\Delta.V) = 0 \quad (2.26)$$

From equation 5 $E = 0$, k_i is large and $M > m$ Considering the compressibility term and velocity of ion, we can have

$$\Delta.V = \Delta.\left\{ \frac{M}{eB^2}(g \times B) - (\frac{k_b T_i}{enB^2})(\Delta \times B) \right\} \quad (2.27)$$

since g and B do not varying in the $g \times B$, the first term vanishes. Also $\Delta.(\Delta n \times B) = 0$ and $(\Delta n \times B).\Delta n = 0$. This equation shows plasma flow is incompressible. Now the continuity and divergence of the current are given by

$$\frac{\partial n}{\partial t} + V.\Delta n = 0 \quad (2.28)$$

$$\Delta.J = 0 \quad (2.29)$$

From equation 11 and equation 7 and replacing E by ΔE

$$\Delta.J = \Delta.\left\{ \frac{ne^2 V_{in}}{M\Omega^2} \Delta E + \frac{ne}{\Omega} g \times B - \frac{k_b}{B^2}(T_i + T_e)(\Delta \times B) \right\} \quad (2.30)$$

But $\Delta.(\Delta \times B) = 0$

$$\Delta.J = \Delta.\left\{ \frac{ne^2 v_{in}}{M\Omega^2 i} \Delta E + \frac{ne}{\Omega} g \times B \right\} = 0 \quad (2.31)$$

For the current is owing along x and z, the continuity equation becomes

$$\frac{\partial n}{\partial t} + V_x \frac{\partial n}{\partial x} + v_z \frac{\partial n}{\partial z} = 0 \quad (2.32)$$

Where $v_x = \frac{Mg}{eB} = \frac{Q}{e}$ and $v_z = \frac{\Delta E_x}{B}$

Now the linearized continuity equation becomes

$$\frac{\partial n}{\partial t} + \frac{Q}{e}\frac{\partial n}{\partial x} - \frac{1}{B}\frac{\partial \phi}{\partial x}\frac{\partial n}{\partial z} = 0 \quad (2.33)$$

After certain rearrangement

$$w_i = -\frac{g}{v_{in}}(\frac{1}{n_o})(\frac{\partial n_o}{\partial z}) \quad (2.34)$$

When $\frac{\partial n_o}{\partial z}$ is positive corresponding to the density gradient anti parallel to g, w_i is negative and $e^{iwt} = e^{iw_r t} e^{\gamma t}$, where γ is positive and thus yields a growing solution. The parameter γ is the growth rate of the instability and is given by $\gamma = \frac{g}{L v_{in}}$ where, L is the gradient scale length.When γ is increase the instability is also increase. Gravity is not the only destabilizing influence in the equatorial ionosphere.The following can also affect the growthr ate Eastward electric field enhance RT-instability while the west ward quench it and the neutral wind are the other parametrizes. According to Sultan (1996) the generalized growth rate can be given by

$$\gamma = \frac{\sum_P^F}{\sum_P^E + \sum_P^F}(Vp - U_n^p - \frac{gL}{U_{in}^{eff}})\frac{1}{Ln} - RT \quad (2.35)$$

where, gL is the downw arda ccelerarion due to gravity, $Vp = \frac{E \times B}{B^2}$ is the vertical component of plasma drift due to the zonal component of the electric field E at the magnetic equator, U^{p_n} is the vertical component of the neutral wind velocity perpendicular to B. $u^{eff_{in}}$ is the effective flux-tube integrated F-region ion neutral collision frequency weighted by the number density in the flux tube, Ln is the scale length of the vertical gradient of the flux-tube integrated plasma density measured at the equator, RT is the flux-tube integrated recombination rate.

The commonly accepted scenario for the formation of spread F and plasma bubbles is, during the day, the atmospheric wind generates a dynamo electric field in the lower ionosphere that is eastward, and this field is mapped to F-region altitudes along magnetic filed. The current $(\vec{J_x})$ is along $g \times \vec{B}$ which is horizontal to the surface, and has divergence that pile up charges on the edges of the small initial perturbation, as a result perturbed electric filed (ΔE) is generated and force plasma to drift with $\Delta E \times B$ velocity. As we can observe from Figure 2.6, initial small

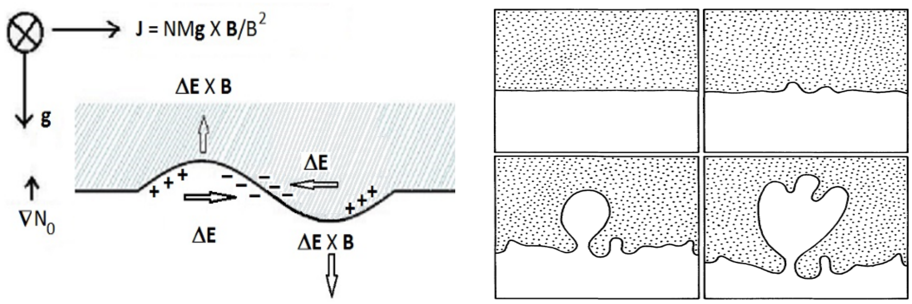

Figure 2.6: Schematic diagram of the plasma analog of the Rayleigh-Taylor instability when the heavy fluid is initially supported by a transparent lighter fluid geometry (Bhattacharyya, 2022).

oscillations in the surface grow "in place," pushing the lighter fluid upward. In the ionospheric case the "light fluid" is the low-density plasma, which carries a gravity-driven current that provides the $\vec{J} \times \vec{B}$ force, preventing the plasma from freely falling (Kelley, 2009). The eastward electric field, in combination with the northward magnetic field, produces an upward $\vec{E} \times \vec{B}$ drift of the F-region plasma (Schunk and Nagy, 2009). As the ionosphere co-rotates with the Earth toward dusk, the eastward component of the neutral wind increases, with the wind blowing predominantly across the terminator from the dusk side to the down side. The increased eastward wind component, in combination with the sharp day and night conductivity gradient across the terminator, leads to the pre-reversal enhancement in the eastward electric field. The RTI is initiated by the larger upward vertical drift and notable F-regions, on contrary, both down ward vertical and pole ward meridional winds makes the F-region more stable and preventing bubbles formation. There is thus a divergence, and charge will pile up on the edges of the small initial perturbation. As a result, ΔE build up in the directions shown. These fields in turn cause an upward $\Delta E \times B$ drift of the plasma in the region of plasma depletion and a downward drift in the region where the density is high. When a heavier fluid is supported by a lighter fluid against gravity, the equilibrium is unstable to any perturbations of the interface (Isobe et al., 2005; Piriz et al., 2006; Sultan, 1996). For if a parcel of heavier fluid is displaced downward with an equal volume of lighter fluid displaced upwards, the potential energy of the configuration is lower than that in the initial state, and the process goes on (Liu, 2019; Taylor, 1950). This instability is called the RTI. These have been derived from photographs of the hydrodynamic RTI when a light fluid supports a heavier fluid against gravity. Therefore during the night, the lower ionosphere rapidly decays and the vertical density gradient develops on the bottom side of the raised F layer (Sahai et al., 2000). This produces the classical configuration for the RTI, in which a heavy fluid is situated above a light one. A density perturbation can trigger the RTI on the bottom side of the F-layer under certain conditions(Garcia et al., 2000; Kelley et al., 1996). Once triggered, density irregularities develop, and the field-aligned depletions then bubble up through the F layer (Huba and Ossakow, 1981). However, the F-layer height and bottom side density gradient are not the only conditions necessary for the RTI and spread F, upward propagating gravity waves, which induce vertical winds, can trigger the RTI both by providing an initial perturbation and by affecting the instability condition (Schunk and Nagy, 2009). It also formed during the rapid Dst changes. The generation of the plasma bubbles are more frequent in equatorial and low latitude regions than in mid-latitude and high latitude regions. In the equatorial and low latitude, ionosphere irregularities mostly affects the amplitude and less frequently affect the phase of the plasma signals. The post sunset equatorial irregularities are generated primarily due to the R-T plasma instability mechanism. The study by (Mendillo et al., 2001) showed that the strength of electron density gradient between the crest and the trough of the EIA correlated with the strength of the electro dynamical vertical drift near sunset which controls the onset of the ESF or plasma bubble irregularities. At low latitude regions the EIA is formed by combined effects of $\vec{E} \times \vec{B}$ drift and ambipolar diffusion (Giday et al., 2020).

2.5.1 Equatorial Ionization Anomaly (EIA)

EIA is one of the most prominent features of the Earth's ionosphere. It is characterized by two bands of increased electron density located approximately 20° to 20° north and south of the magnetic equator. The anomaly plays a critical role in ionospheric science and has significant implications for satellite communications, navigation systems, and radio wave propagation (Kelley, 2009). The EIA forms due to a process known as the equatorial fountain effect. During the daytime, the Earth's magnetic field interacts with the eastward electric field in the ionosphere, causing plasma at the equator to experience a vertical uplift via the $E \times B$ drift. Once elevated to higher altitudes, the plasma diffuses along the Earth's magnetic field lines under the influence of gravity and pressure gradients, resulting in two highdensity ionization regions on either side of the magnetic equator (Anderson, 1973; Kelley, 2009). At the geomagnetic equator, the magnetic field lines extend horizontally in a north-south direction (Mendillo et al., 2001). Within the E-region ionosphere, tidal winds generate daytime currents, leading to the accumulation of positive and negative charges at the dawn and dusk terminators, respectively. This phenomenon is most pronounced during periods of high solar activity when increased solar radiation ionizes the Earth's upper atmosphere more effectively. Seasonal and diurnal variations also influence the intensity of the EIA. For instance, it tends to be stronger during the equinox months due to the alignment of the Earth's magnetic and geographic equators, which maximizes the fountain effect (Patel et al., 2017).

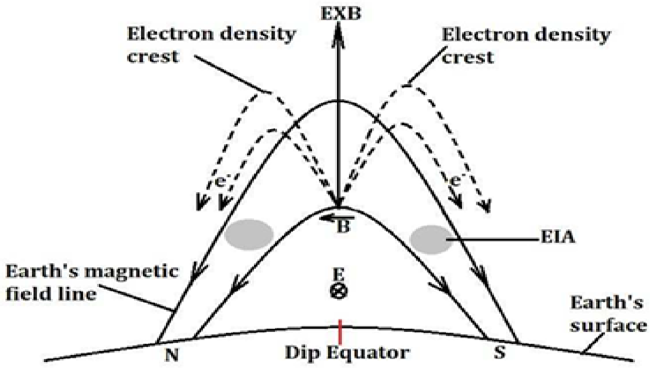

Figure 2.7: A schematic diagram illustrating the equatorial fountain effect and upward plasma drift due to $E \times B$ (Ngwira, 2011)

The EIA impacts several technologies that rely on the ionosphere. For example, the variability in ionospheric electron density caused by the anomaly can introduce errors in GNSS, such as GPS, by causing signal delays. Moreover, the presence of plasma irregularities within the EIA region can lead to scintillation, or rapid signal fluctuations, which degrade communication and navigation system performance (Appleton, 1946).

2.5.2 Equatorial plasma bubbles (EPBs)

EPBs are large-scale ionospheric irregularities that occur in the Earth's equatorial ionosphere, primarily in the F-region, which is the highest ionized layer of the atmosphere. EPBs are characterized by a depletion of plasma density, and they play important role in space weather phenomena, influencing radio wave propagation, GPS signals, and satellite communications. These bubbles are important for understanding ionospheric processes and their impact on technological systems that rely on the ionosphere. EPBs form as a result of a combination of processes driven by the equatorial electrojet and the dynamics of ionospheric plasma. EIA, a phenomenon where the ionospheric plasma concentration peaks at latitudes slightly off the magnetic equator, creating an enhanced ionization region. This structure is influenced by solar and geomagnetic activity. At sunset, the ionosphere experiences a reduction in solar radiation, and the vertical plasma drift due to the electric field causes plasma to concentrate in the equatorial region. This accumulation of plasma becomes unstable and leads to the development of EPBs (Balan et al., 2018). The primary driving force for the formation of EPBs is the vertical drift of ionization, induced by the electric field in the ionosphere. This drift leads to the growth of plasma instabilities, particularly the RTI, which causes the plasma to bubble upward, forming regions of depleted electron density. These bubbles are typically generated during the post-sunset period, between 18:00 and 00:00 local time (Yokoyama et al., 2014). The

EPBs grow and expand with altitude, often reaching heights of over 1000 km and sometimes covering extensive horizontal distances, spanning hundreds to thousands of kilometers. EPBs exhibit a characteristic plasma density depletion at their center, surrounded by a region of enhanced electron density. These bubbles can cause severe radio signal scintillations, which are rapid fluctuations in the amplitude and phase of radio signals transmitted through the ionosphere. These scintillations can disrupt HF communications and degrade the accuracy of GPS signals, leading to navigation errors. The severity of EPBs and their effects on communication systems depend on the intensity of the plasma depletion and their size (Abdu, 2005).

The spatial extent and intensity of EPBs can vary depending on several factors, including the level of solar activity, geomagnetic conditions, and local ionospheric dynamics. During periods of high solar activity (solar maximum), the occurrence of EPBs tends to increase, as enhanced solar radiation affects the ionization processes and the vertical drift (Yokoyama et al., 2014). Conversely, during the solar minimum, when solar radiation is lower, EPBs are less frequent and less intense. EPBs are influenced by space weather events, particularly geomagnetic storms and solar flares. These events can alter the electric field and neutral wind patterns in the ionosphere, which can enhance the vertical drift and increase the likelihood of EPB formation. Studies have shown that geomagnetic storms often lead to an increase in the occurrence and size of EPBs (Abdu, 2005).

Solar activity, through the modulation of the ionospheric conditions, plays a significant role in determining the occurrence and behavior of EPBs. During periods of high solar activity, the increased solar radiation leads to stronger ionization in the equatorial region, increasing the probability of plasma bubble formation. In contrast, during low solar activity, such as the solar minimum, the reduced solar radiation results in fewer EPBs. The study of EPBs is critical for understanding their effects on space weather and communication systems. Various techniques are employed to detect and characterize EPBs, including ground-based ionosondes, radar systems, and satellite observations. One of the most widely used methods is the measurement of TEC using GPS signals, which can provide detailed information on the ionospheric electron density distribution and the presence of plasma irregularities. In particular, the sTEC and ROTI are often used to detect and quantify EPBs (Balan et al., 2018). Advanced geostatistical methods, such as Kriging, have also been applied to model and analyze TEC variations over regions like East Africa, helping to identify and characterize EPBs more accurately (Balan et al., 2018). These techniques allow researchers to map the spatial and temporal evolution of EPBs and better understand their behavior.

The formation and evolution of EPBs are primarily governed by the generalized RTI, which occurs when a region of low plasma density underlies a region of higher plasma density in the presence of gravity and a background electric field (Klenzing et al., 2023). The onset of this instability depends on a delicate balance between gravitational, collisional, and electrodynamic forces. At the equator, these dynamics are strongly modulated by neutral winds and ionospheric electric fields, which together determine the background conditions under which plasma instabilities either grow or depleted (Bhattacharyya, 2022). Thus, understanding EPB behavior requires a comprehensive treatment of the coupled ionosphere-thermosphere system.

Neutral winds in the thermosphere play important role in regulating EPB dynamics through both direct and indirect mechanisms. In the equatorial region, the zonal (east-west) and meridional (north-south) components of neutral winds interact with the ionospheric plasma through ion-neutral collisions, driving dynamo electric fields (Klenzing et al., 2023). During the evening hours, the PRE of the eastward electric field is one of the most important factors controlling EPB initiation. This enhancement results from the combined action of the F-region dynamo, which is influenced by the eastward neutral wind, and the upward plasma drifts that develop around sunset (Huba, 2024). When the eastward electric field intensifies, the F-layer is lifted to higher altitudes where recombination rates are lower, making the plasma more susceptible to RTI (Bhattacharyya, 2022). As a result, strong eastward neutral winds during the evening can enhance the probability of EPB formation, while westward winds tend to suppress it by reducing the magnitude of the PRE.

The meridional component of the neutral wind also contributes significantly to the development and evolution of EPBs. Meridional winds can cause hemispheric asymmetries in plasma distribution by pushing plasma along geomagnetic field lines from one hemisphere to the other. This redistribution modifies the background electron density gradient and can create longitudinal and latitudinal variations in EPB occurrence. Moreover, changes in meridional wind patterns can shift the apex height of the F-region, altering the local electrodynamic conditions that control instability growth. For instance, poleward winds can lift the F-layer and favor bubble development, whereas equatorward winds can lower it, suppressing instability growth (Huba, 2024).

Once EPBs are initiated, their nonlinear evolution becomes strongly coupled to ionospheric electrodynamics. As the instability grows, charge separation occurs within the developing plasma depletions, generating polarization electric fields that amplify the original perturbations. These polarization fields drive $E \times B$ drifts, lifting depleted plasma regions further upward and deepening the bubbles. Because geomagnetic field lines are equipotentials, these localized electric field perturbations map along magnetic field lines to higher latitudes, effectively coupling the equatorial and off equatorial regions. This mapping allows disturbances generated near the magnetic equator to influence ionospheric currents and plasma structures several degrees away, creating large-scale coherence in EPB structures observed in satellite and radar data (Bhattacharyya, 2022).

The coupling between plasma and neutral dynamics does not end with the initiation of EPBs. As bubbles rise through the ionosphere, they displace plasma and neutral particles, generating gravity and acoustic waves that propagate through the thermosphere. These waves can modify the background wind field, creating secondary perturbations that may either enhance or suppress further EPB development (Yokoyama et al., 2019). For example, gravity waves generated by existing bubbles can modulate the local wind field and seeding conditions for subsequent instabilities, contributing to the observed variability and intermittent of EPBs across different longitudes and nights. This feedback mechanism highlights the self-organizing nature of the ionosphere-thermosphere system, where plasma instabilities can dynamically alter the very background conditions that control their growth (Bhattacharyya, 2022; Huba, 2024).

Electrodynamic coupling also plays a central role in the longitudinal and temporal variability of EPBs. The intensity and timing of the PRE, the background electric field configuration, and the thermospheric wind patterns vary significantly with longitude, season, and geomagnetic activity (Klenzing et al., 2023). These variations explain why EPBs are more frequent in certain regions, such as the Atlantic or African sectors, compared to others. Additionally, magnetospheric inputs, such as prompt penetration electric fields or disturbance dynamo effects during geomagnetic storms, can alter the electrodynamic environment, influencing both the onset and suppression of EPBs (Bhattacharyya, 2022).

In general, the development of equatorial plasma bubbles represents a highly coupled process involving interactions between neutral atmospheric dynamics and ionospheric electrodynamics (Yokoyama et al., 2019). Neutral winds modulate the background electric fields through dynamo action, controlling the altitude and stability of the F-layer, while electrodynamic feedback mechanisms within the plasma amplify initial perturbations into large-scale structures. The resulting thermospheric responses, including gravity wave generation and momentum transfer, further feed back into the system, creating a dynamic equilibrium that governs EPB occurrence and morphology. A full understanding of EPB dynamics therefore requires a holistic view that integrates neutral wind effects, electrodynamic processes, and the nonlinear feedbacks inherent in the coupled ionosphere-thermosphere system (Otsuka, 2018; Yokoyama et al., 2019).

Chapter 3

Data Sources and Methodology

3.1 Data Source

A lot of scientists use observation techniques to locate EPBs in the ionosphere. We have used the detrended curve technique involves subtracting the moving average of the sTEC from the sTEC values. This results in a detrended curve that can be analyzed to identify sTEC depletions and distinguish the irregularities associated with EPBs (Portillo et al., 2008). Using the sTEC derivative curve, which was developed from GPS measurements, this study investigated the ionospheric plasma bubbles that occurred in 2015 (Kumar and Chen, 2016). The geographic and geomagnetic coordinates of these GPS stations, along with the data availability period, are listed in Table 3.1 and locations of the stations are clearly observed from figure 3.1. The GNSS data form `htpp://www.unavco.org/data/data.html`, Kp information, and Dst index information were obtained from `https://omniweb.gsfc.nasa.gov/form/dx1.html` and `https://wdc.kugi.kyoto-u.ac.jp/wdc/Sec1.html` respectively.

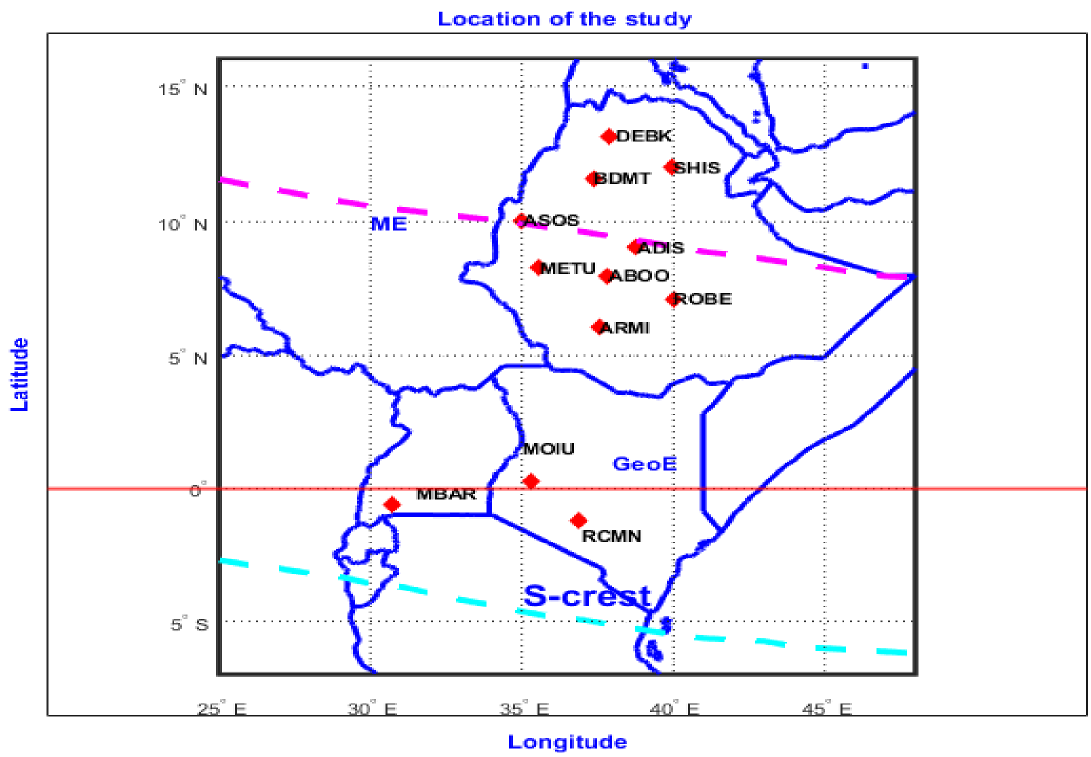

Figure 3.1: Locations of all GPS receiver stations used in study.

Table 3.1: The geographic and geomagnetic coordinates of the GNSS stations.

Stations	Geog.Lat (°N)	Geog.Lon (°E)	Geom.Lat (°N)	Geom.Lon (°E
DEBK	13.08	37.89	4	109.2
BDMT	11.55	37.35	2.5	109.7
ADIS	9.035	38.766	0.15	111.1
ASOS	10.067	34.53	5.3	102.0
ABOO	8.59	37.51	0.8	109.7
ROBE	7.12	39.99	-1.09	112.5
METU	8.3	35.58	-1.2	107.4
SHIS	7.27	37.76	-0.9	110.6
ARMI	6.0	38.766	-1.4	111.3
MOIU	0.29	35.3	-8.8	106.7
MBAR	-0.6	30.75	-15.9	99.7
RCMN	-1.221	36.893	-10.85	106.5

3.2 Methodology

We use the RINEX data from twelve GPS stations. The Gopi v3.02 software, created by Seemala and Valladares (2011), was used to extract the sTEC values, the azimuth, and the elevation angles of the satellites from the receiver station. Elevation angles of 30° and above were used to prevent the multi-path impacts of the chosen data (Abiriga et al., 2020). we have used the MatLab Programming Language to analysis the data. TEC data derived from GPS pseudorange measurements are subject to uncertainties due to the high noise levels inherent in the pseudorange. However, this does not mean that the electron distribution across the ionosphere is random. To address areas where direct measurements are lacking, spatial inter polation methods like Kriging are used. Kriging allows us to estimate variations and depletions in the vertical total electron content (VTEC), providing a more accurate and continuous representation of electron density across the ionosphere. It is a method of constructing new data point with in a rangeof a discrete set of known data points (Kastelec and Košmelj, 2002). The concept of the interpolation is that the points which are close together in space are more likely to have similar values and attributes as compared to points which are far apart. Mostly the interpolation is divided into two stochastic and deterministic kinds of interpolation. Stochastic interpolation methods incorporate the concept of randomness, meaning some data points are thought of as being random, and deterministic methods do not use probability theory, that means all the points are thought as being accurate (Meijering, 2002). In this study, we apply Ordinary Kriging interpolation techniques to estimate the spatial distribution of TEC across the chosen area (Maglambayan and Macalalad, 2022). The first step in interpolation using kriging is the for mation of a semi-variogram, this is a diagram of the spatial dependence of samples and is a function of all possible separations and semi-variance.

3.2.1 Measurement of Total Electron Content (TEC)

TEC is an important quantity to study the ionosphere of the Earth. It is the total number of electrons present along a path between GPS reciver to satellite potions, with units of electrons per square meter, where 10^{16} electrons/m^2 = 1 TEC unit (TECU). TEC is also a key parameter not only for ionospheric studies but also for the correction of ionospheric effects which degrade GNSS positioning accuracy, navigation and communication. IT is significant in determining the scintillation and group delay of a radio wave through a medium. Ionospheric TEC is characterized by observing carrier phase delays of received radio signals transmitted from satellites located above the ionosphere, often using GPS satellites (Ya'acon et al., 2012).

3.2.2 Slant TEC (sTEC)

First, the sTEC was extracted from the dual-frequency GPS phase and pseudorange observables by utilizing the frequency-dependent dispersive characteristics of the ionosphere (Vankadara et al., 2022). The sTEC represents the total number of electrons along the ray path from the satellite to the receiver, measured in units of TECU.

$$sTEC = \frac{f_1^2 \times f_2^2}{40.3\,(f_1^2 - f_2^2)}\,(p_2 - p_1) \tag{3.1}$$

where $f_1 = 1575.42MHz$ and $f_2 = 1227.60MHz$ are the dual frequencies transmitted by GPS satellites and P_1 and P_2 are the respective pseudo range observations.

3.2.3 Vertical TEC (VTEC)

VTEC is the main focusing area in the ionosphere research. Therefore, the sTEC obtained from GPS observable are converted to vertical using a suitable mapping function. However this conversion introduces a few errors in the middle latitude where electron density is small. But it may result in obvious errors at low latitude with large electron density and great gradient (Wanninger, 1993).

In order to refer to the vertical TEC, the single layer thin-shell model was employed to determine the absolute VTEC. TEC measurement is based on the assumption that the ionosphere can be modeled as a thin spherical shell located at a fixed altitude, typically around 700 km above the Earth's surface corresponding to the center of mass of the ionospheric electron density profile. To estimate the VTEC from the measured sTEC, a mapping function (MF) is used. This function accounts for the increased path length through the ionosphere at oblique angles. The point at which the satellite signal intersects the ionospheric shell is known as the Ionospheric Pierce Point (IPP). The angle between the local zenith at the IPP and the line of sight to the satellite is the zenith angle, and it determines the correction factor.

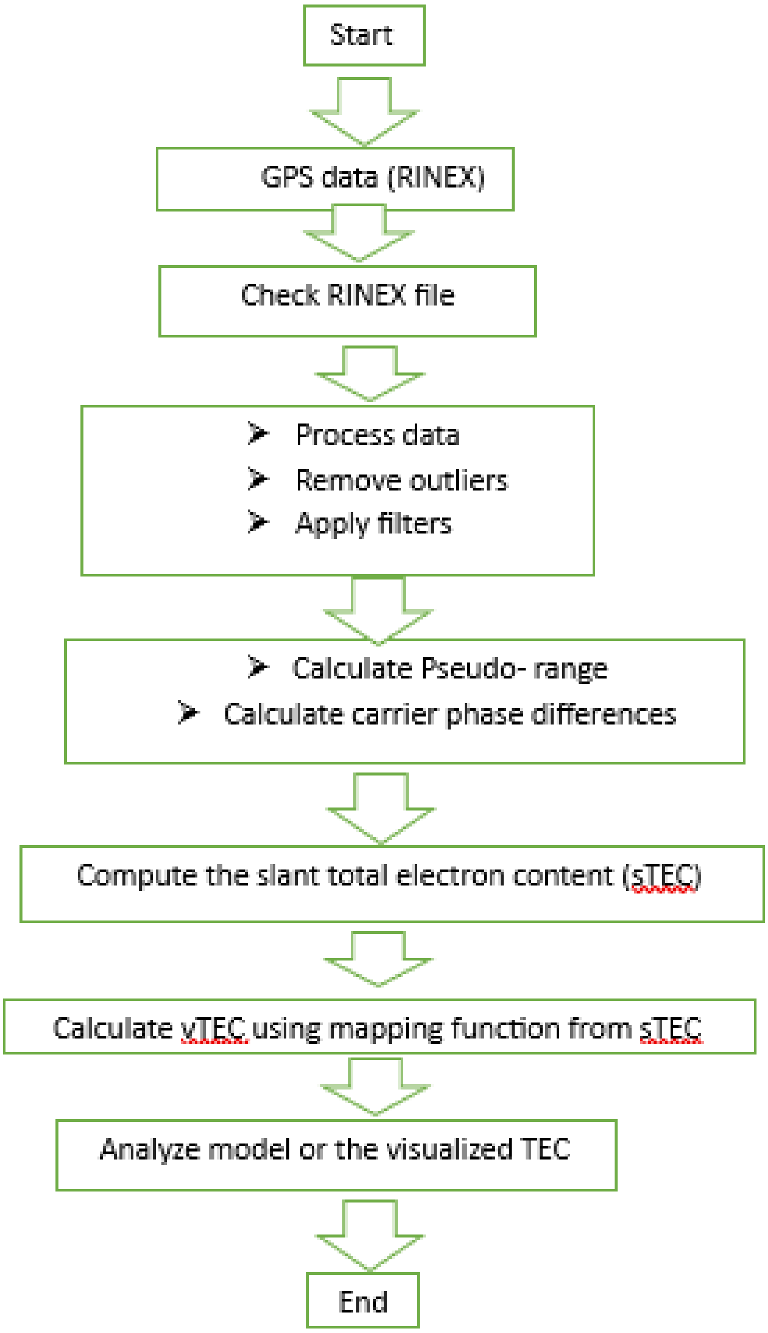

Figure 3.2: Flowchart to calculate the GPS-TEC data and processing.

$$VTEC = sTEC(cosX') \tag{3.2}$$

The most commonly used MF is the so called Single-Layer order to verify the new MF concept we modified the Bernese software Model (SLM), which assumes that the electron density field over one GNSS station is spherically symmetric.

$$F(X) = \frac{TEC(X)}{TEC(0)} = \frac{1}{cosX'(orsin\beta')} = \frac{1}{\sqrt{1 - sin^2X'}} \tag{3.3}$$

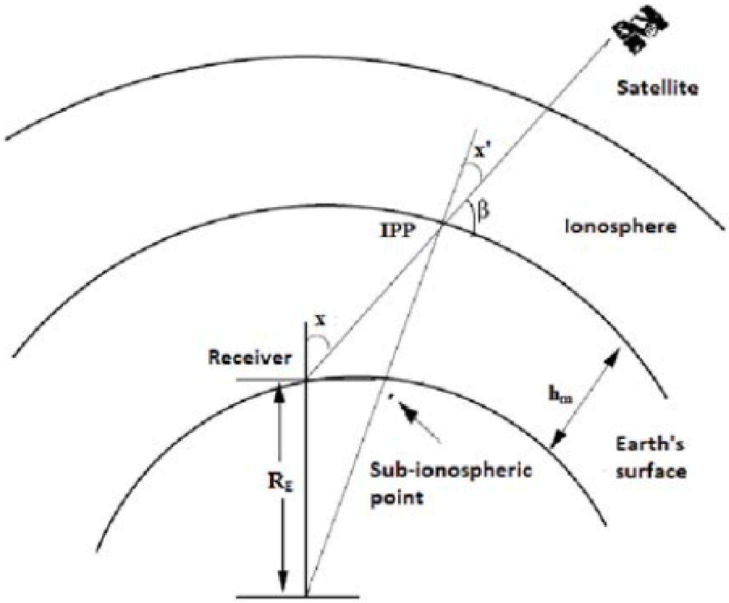

Figure 3.3: Ionospheric single layer model (Hofmann-Wellenhof et al., 1994; Mannucci et al., 1998; Yaacob et al., 2010).

Where $SinX' = \frac{R_E}{R_E+h_m}sinX$
R_E = the mean earth radius
h_m = the height of a maximum electron density, and X and X' =the zenith angles at the receivers site and at the ionospheric pierce point IPP, with value of Re is typically set to 6371 km and hm is at 350 km.

3.2.4 Interpolation techniques

Interpolation techniques are generally classified into two main categories: deterministic and geostatistical methods. Deterministic interpolation techniques generate surfaces from measured data points based on mathematical relationships, such as the degree of similarity. In contrast, geostatistical interpolation techniques, rely on the statistical properties of the measured data. These methods quantify spatial autocorrelation among sample points and consider the spatial arrangement of those points relative to the location being predicted. Spatial interpolation is a key technique in geostatistics used to estimate values at locations where data has not been collected, based on measurements from known points. According to Miranda (2005), interpolation is the process of determining unknown or unsampled values of a continuous variable using known or sampled data. Similarly, Molin et al. (2015) explain that interpolation relies on the assumption that samples located close to each other are more likely to have similar values than those that are farther apart. There are a number of interposition techniques, such as Inverse Distance Weighted (IDW), Multiqufric function (MQ), Cubic B-spline, Kriging (KR) and Neural Network (NN). Deterministic interpolation methods, such as IDW, MQ, NN, and Cubic B-spline, are relatively straightforward to implement. However, they do not account for the spatial structure within the data and are therefore less effective when dealing with sparsely or unevenly distributed datasets (Grynyshyna-Poliuga et al., 2014). In contrast, geostatistical techniques notably Kriging methods incorporate both the distance between observations and the underlying spatial structure of the data. Moreover, these methods allow for the generation of error maps, which help identify areas where predictions are either reliable or uncertain (Blanch and Walter, 2002). Owing to its robustness and ability to model spatial dependence, Kriging interpolation has become one of the most widely used techniques to map TEC distribution and variability (Cressie, 2015).

3.2.5 Ordinary Kriging (OK)

These kriging technique is a linear interpolator that belongs to the best linear unbiased estimator family estimators (Cosentino et al., 2023; Grynyshyna-Poliuga et al., 2014; Zimmerman et al., 1999). The main purpose is to estimate a certain unknown variable (Z^*) as a linear combination of the known values (Z_i) (Li et al., 2022).

$$Z^* = \sum_i \omega_i Z_i \tag{3.4}$$

, ω_i being the weights computed by the kriging equations, that are applied to each value $Z(x_i) = Z_i$. In order to apply the ordinary kriging technique, it is necessary to assume that the random function Z_i belongs to the stationary random functions family, which means that the mean values and the standard deviation of Z_i have to be independent of the location, moreover, the unbiased condition over the weights ($\sum \omega_i = 1$) is imposed. Then, the variance is minimized with the help of the Lagrange multipliers in order to impose the unbiased condition for details:

$$L = \frac{1}{2} E[(z^* - z)^2] - \lambda(\sum_i \omega_i - 1) \tag{3.5}$$

, $E[(z^* - z)^2]$ being the z^* variance that can be expressed as a function of the semivariogram:

$$E[(z^* - z)^2] = 2 \sum_i \omega_i \gamma_{io} - \sum_i \sum_j \omega_i \omega_j \gamma_{ij} \tag{3.6}$$

Therefore, in order to get the weights (ω_i), the following equation, that is expressed in matrix notation, has to be solved:

$$\sum_i \omega_i \gamma_{ij} + \lambda = \gamma_{io} \tag{3.7}$$

After differencing Eq. (3.7) with respect to λ and ω_i , and equating to zero (0), the ordinary kriging equations are obtained in compact form:

$$\Omega = \Gamma\Gamma_o \tag{3.8}$$

$$\Omega = \begin{bmatrix} \omega_1 \\ \omega_2 \\ \vdots \\ \omega_n \end{bmatrix}, \Gamma_o = \begin{bmatrix} \gamma_{10} \\ \gamma_{20} \\ \vdots \\ \gamma_{no} \\ 1 \end{bmatrix}, \Gamma = \begin{bmatrix} \gamma_{11} & \cdots \gamma_{1n} & 1 \\ \gamma_{21} & \cdots \gamma_{2n} & 1 \\ \vdots & \vdots & \vdots \\ \gamma_{n1} & \cdots \gamma_{nn} & 1 \\ 1 & \cdots 1 & 0 \end{bmatrix}$$

where, Ω being the vector that contains the weights ω, λ, Γ is the matrix that contains the semivariogram estimations for the known values and locations, and Γ_o is the vector that contains the semivariogram estimations for the unknown values but with known locations (Ali et al., 2006).

3.2.6 Semivariogram

The semivariogram is a fundamental tool in spatial statistics and geo-statistics. It describes the spatial correlation of a dataset by measuring how similar values are at increasing distances. It is widely used in Kriging interpolation, spatial variability analysis, depletion of electron density and TEC mapping in ionospheric studies. The semivariogram function $\gamma(h)$ is given by:

$$\gamma(h) = \frac{1}{2N(h)} \sum_{i=1}^{N(h)} \Big(Z(x_i) - Z(x_i + h) \Big)^2 \tag{3.9}$$

where $\gamma(h)$ = Semi-variance at lag distance h.
$Z(x_i) + Z(x_i + h)$ = Observed values at locations separated by distance h.
$N(h)$ = Number of data pairs at distances h. A theoretical semivariogram model was fitted to the experimental semivariogram to ensure continuity in the semivariogram values. The key semivariogram parameters are the sill, range, and nugget effect were then estimated to characterize the spatial variability and correlation structure of the dataset.

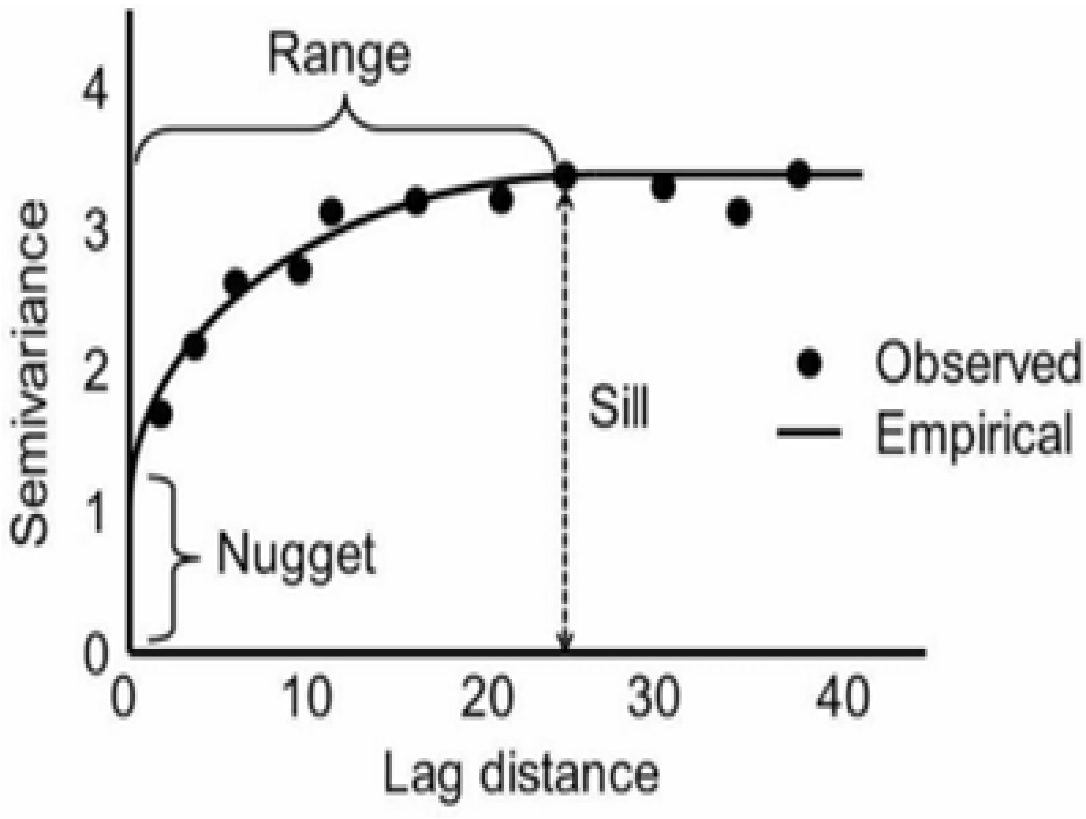

Figure 3.4: Semi-variogram illustrating the spatial structure of a regionalized variable. The Nugget represents the semi-variance at zero distance, reflecting measurement error or micro-scale variability. The Sill indicates the total variance, reached when spatial dependence levels off. The Range is the distance beyond which data points become uncorrelated, marking the extent of spatial autocorrelation (Biswas and Si, 2013).

Nugget effect

Theoretically, at zero separation distance or lag distance zero, the semivariogram value is also zero (Morgan, 2011). However, at an infinitesimally small separation distance, the semivariogram often exhibits a nugget effect, which is some value greater than zero. For instance, if the semivariogram model intercepts the y-axis at 3, then the nugget is also 3. It's effect can be attributed to measurement errors or spatial sources of variation at distances smaller than the sampling interval. Measurement error occurs because of the error inherent in measuring devices. Natural phenomena can vary spatially over a range of scales. Variation at micro-scales smaller than the sampling distances will appear as part of the nugget effect (Carrasco, 2010; Kelkar et al., 2002).

Sill

The sill is the total variance where the empirical variogram models appears to level off, and is the sum of the nugget plus the sills of each nested structure. The Variogram models points above the sill indicate negative spatial correlation, while points below the sill indicate positive correlation (Cameron and Hunter, 2002). We can use the variance of data as a reasonable default. The variogram may not exhibit a sill if trends are present in the data. In that case, geostatistical analysis should proceed with caution, and at the least, ordinary kriging should be used for mapping (Deutsch et al., 1992).

Range

The lag distance at which the semivariogram (or semivariogram component) reaches the sill value. Presumably, autocorrelation is essentially zero beyond the range.

To choice the best model, that have best performance of the semi variogram models: Exponential, Gaussian and Spherical was analyzed by fitting each model to the experimental semivariogram. These semi variogram models were further investigated using a random variable Q_1 statistical test (Pignalberi et al., 2018). The Q_1 statistical test quantifies the residuals between the values of the model and those of the experimental semivariances. The Q_1 test was carried out on all the three semivariogram models for selected during quiet days. The values of Q_1 were calculated from the residues using the Equation below.

$$Q_1 = \frac{1}{n}\sum_{k=2}^{n}\frac{\delta k}{Sk} \tag{3.10}$$

where n is the number of observations, $\frac{\delta k}{Sk}$ are the normalized residues, δk are the residues and δS is the variance of the observations. If the value of Q_1 is close to zero, the performance of the model is confirmed well (Kitanidis, 1997).

The other method is the Root-Mean-Squared Residuals (RMSRes) is a statistical measure that quantifies the average magnitude of the error between predicted values and observed values. It is commonly used to evaluate the accuracy of a prediction model. The RMSRes method is given by:

$$RMSRes = \sqrt{\frac{1}{n}\sum_{i=1}^{n}(TEC_{predicted,i} - TEC_{observed,i})^2} \tag{3.11}$$

Where: **n** is total number of data points, and **i** is the index of each data point in the dataset.

Gaussian Semivarogram Model

The Gaussian model assumes a smooth transition in spatial correlation and is best suited for continuous spatial processes with gradual changes.

$$\gamma(h) = C_o + C\left[1 - e^{-}\left(\frac{h}{a}\right)\right]^2, h > 0. \tag{3.12}$$

where C_o = nugget effect
C = Partial sill (total variance minus the nugget)
$C_o + C$ = sill (maximum semi-variance)
a = range

Spherical Semivariogram Model

The Spherical model assumes that spatial correlation increases linearly before leveling off at the range.

$$\gamma(h) = C_O + C\left[\frac{3h}{2a} - \frac{1}{2}\left(\frac{h}{3}\right)^3\right], 0 \leq h \leq a \tag{3.13}$$

where a =range beyond which spatial correlation is zero.

Exponential Semivariogram Model

The Exponential model assumes an exponentially decreasing spatial correlation, making it suitable for rapid variations over short distances.

$$\gamma(h) = C_o + C\left(1 - e^{-\frac{h}{a}}\right), h > 0 \tag{3.14}$$

3.2.7 ROTI index

ROTI is the ionospheric index used to indicate the existence of ionospheric irregularity Pi et al. (1997).

$$ROT(t) = \frac{sTEC_{t_2} - sTEC_{t_1}}{t_2 - t_1} = \frac{\triangle sTEC}{\triangle t} \tag{3.15}$$

where Δt is the time difference, t_2 and t_1 are time interval between the subsequent epochs in minute.

$$ROTI = \sqrt{< ROT^2 > - < ROT >^2} \tag{3.16}$$

ROTI is defined as the standard deviation rate of ROT over a 5- minute period. Always, ROTI $\geq 0.5TECU$ indicates the occurrence of ionospheric irregularities at a length of a few kilometers in the nighttime (Lan et al., 2016).

3.2.8 Depletion depth and duration of the depletion

EPB is identified when depletion located on the detrended time curve (original series minus the calculated trend). The depletion of sTEC can be calculated as:

$$Depletion = sTEC - mvgsTEC \tag{3.17}$$

where, $sTEC$ = original sTEC and $mvgsTEC$ = 5 minute moving average of the sTEC.

The depletion depth of EPBs are identified by the formula

$$Dd = \frac{Lmax + Rmax}{2} - Min \tag{3.18}$$

$$Duration = t(Rmax - Lmax) \tag{3.19}$$

Where Dd is depletion depth, $Lmax$ and $Rmax$ the left hand and right hand maximum values of slant total electron content whose minimum electron density is Min respectively.

3.2.9 Percentage occurrence of EPBs

To study the percentage occurrences of EPB, we have used the following formula respectively.

$$MEPBO = \frac{NEPBM}{TNEPBY} \times 100 \tag{3.20}$$

where, $MEPBO$ is monthly EPB occurrence, $NEPBM$ is number of EPB observed during the month and $TNEPBY$ is total number of EPB during the year (Kumar and Chen, 2016).

$$SEPBO = \frac{NEPBS}{TNEPBY} \times 100 \tag{3.21}$$

where, $SEPBO$ is seasonal EPB occurrence, $NEPBS$ is the number of EPB during the season and $TNEPBY$ is total number of EPB in the year used.

3.2.10 Determining the optimal window

To determining the optimal window size for detecting EPB using GPS-TEC data can be approached by relating it to the typical temporal scale (duration) of EPB and the sampling rate of the data. Mathematically given by:

$$N_W = \frac{T_{EPB}}{\Delta t} \tag{3.22}$$

T_{EPB} is duration of an EPB event, Δt is the sampled interval of the data and N_W is optimal window size in number of samples. Determining the optimal window size for detecting EPBs using GPS-TEC data is important for ensuring accurate and reliable identification of these ionospheric irregularities. GPS-TEC measurements inherently contain noise arising from satellite motion, multipath effects, and background ionospheric variability, making it necessary to apply an appropriate averaging or filtering window during data processing. When the window size is too small, the data remains highly noisy. This can increases the likelihood of false EPB detections. In contrast, if the window size is too large, significant TEC variations associated with EPBs may be overly smoothed. This may leads to missed detections of EPBs. Thus, determining the optimal window size requires balancing effective noise reduction with the preservation of the sharp TEC gradients that characterize EPBs. Achieving this balance enhances detection accuracy, improves temporal and spatial resolution, and provides a clearer representation of EPB structures factors that are essential for ionospheric research, space-weather monitoring, and mitigating disruptions to communication and navigation systems.

Chapter 4

Study of Total Electron Content Variations over the Ethiopia Region Using Kriging Technique

4.1 Introduction

Kriging is a geostatistical interpolation method mostly used for spatial prediction of environmental variables such as soil properties, atmospheric parameters, and ionospheric quantities like TEC. It's named after South African mining engineer Danie Krige, the method was later formalized by Matheron (1963), who introduced its theoretical basis as part of regionalized variable theory. Kriging stands out as a primary technique in geostatistics, leveraging spatial correlation to interpolate between data points within a determined range. By utilizing a semivariogram, unbiased and optimal estimations of attribute values are achieved within a defined distance. This method integrates correlation analysis to effectively correlate variables over specified ranges, thereby generating linear unbiased estimates based on both real data and semivariogram structural traits (Maglambayan and Macalalad, 2022). In this work Kriging is used to predict the spatial distribution of VTEC for the international quiet days during the solar maxima year of solar cycle 24 in Ethiopia region and check the performances of semiVariogram models. A key advantage of Kriging is its ability to capture and incorporate spatial correlations, which are repre sented through the variogram. The primary aim of this paper is to investigate the spatial distribution of TEC across the region using the Kriging interpolation technique. Specifically, OK is employed to interpolate TEC variations in unsampled areas and to determine the optimal variogram model for the dataset.

4.2 Results and Discussion

Kriging stands out as a primary technique in geo statistics, leveraging spatial correlation to interpolate between data points within a determined range. By utilizing a semi-variogram, unbiased and optimal esti mations of attribute values are achieved within a defined distance. This method integrates correlation analysis to effectively correlate variables over specified ranges, thereby generating linear unbiased estimates based on both real data and semi-variogram structural traits (Maglambayan and Macalalad, 2022). One of krigings key advantages lies in its ability to minimize calculation variances, distinguishing it from other interpolation methods. In this work Kriging is used to predict the spatial distribution of VTEC for the inter national quiet days during the solar maxima year of solar cycle 24 in Ethiopia region. Figures 4.1a-4.4a illus trates the percentile distribution of VTEC within and around the region, Figs. 4.1b-4.4b showcases the spatial distribution of ionospheric VTEC predicted around the region, and exhibits interpolated VTEC over the region during quiet days, while Figs. 4.1c-4.4c displays the variogram estimator enclosed in a black dot along side the variogram model, predicting TEC variation. In Fig. 4.1a, manifest shift in the percentile distribution of VTEC towards the North-East direction is notice able. Meanwhile, Fig. 4.1b demonstrates the commend able predictive capability of the variogram in capturing this distribution. Similarly, Fig. 4.1c unveil a robust spa tial distribution of VTEC, particularly concentrated between latitudes of 10 and 15 degrees, with TEC val ues peaking at 65 TECU during this period. Upon examining Fig. 4.2, a similar spatial distribution of TEC across the region during nighttime is observed, although with significantly reduced TEC values, around 25 TECU. Both Figs. 4.1 and 4.2 utilize a spherical variogram kriging model to incorporate additional sample points and estimate the remainder of the region, demonstrating good model performance. Maximum total electron content (TECmax) typically occurs during day time, increasing from 30 TECU to 65 TECU in 2012, while minimum total electron con tent (TECmin) rises from 5 TECU to 25 TECU over the same period for the night time. Daytime VTEC values surpass nighttime values, resulting in nighttime depletion. The maximum TEC depletion of 10 TECU is observed between longitudes 30° E to 45° E and latitudes 5° N to 8° N. The spatial resolution and range of the

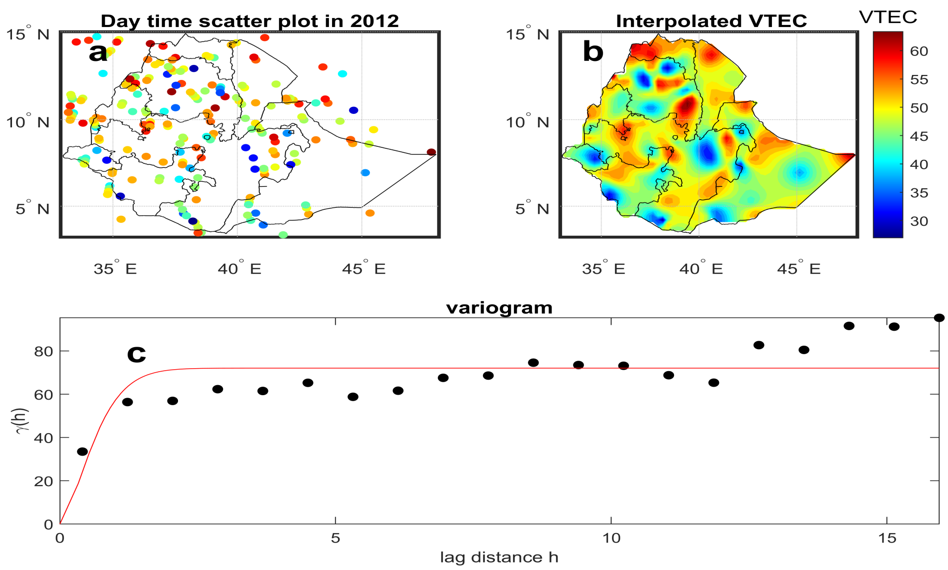

Figure 4.1: Day time VTEC variation estimated by Kriging plot of the average VTEC values during the year 2012. (a) the scattered VTEC observed over Ethiopia ionosphere, (b) the map obtained from Ordinary Kriging interpolation, and (c) the spherical var iogram model.

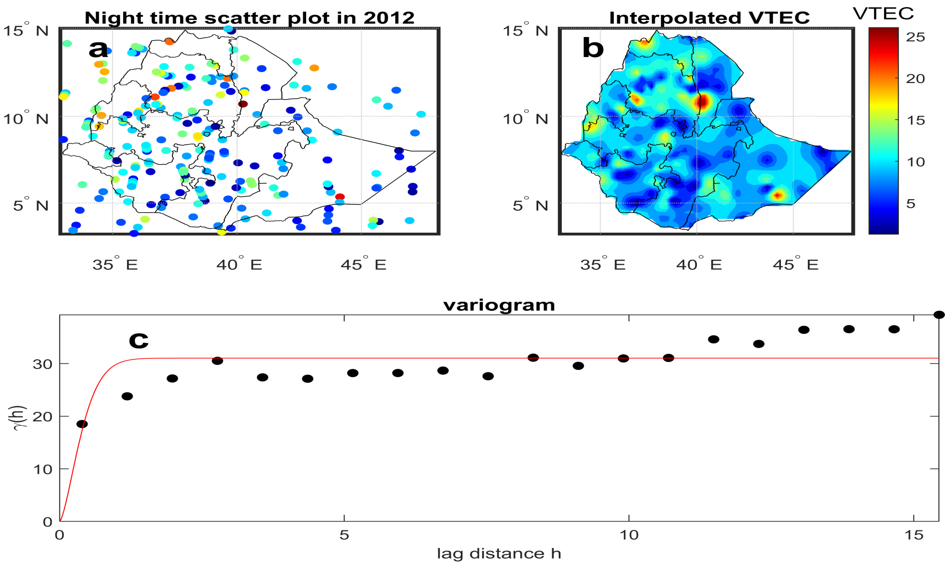

Figure 4.2: Night time VTEC variation estimated by Kriging plot of the average VTEC values during the year 2012. (a) the scattered VTEC observed over Ethiopia ionosphere, (b) the map obtained from Ordinary Kriging interpolation and (c) the spherical var iogram model.

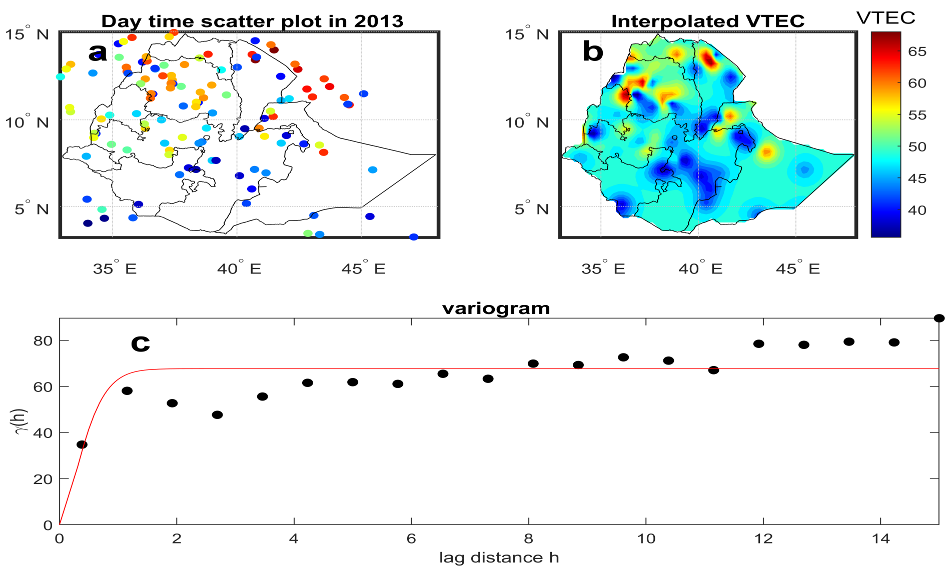

Figure 4.3: Day time VTEC variation estimated by Kriging plot of the average VTEC values during the year 2013. (a) the scattered VTEC observed over Ethiopia ionosphere, (b) the map obtained from Ordinary Kriging interpolation and (c) the spherical var iogram model.

maps pre sented in Figs. 4.3 and 4.4 are consistent with those in the previous section. In Fig. 4.3a, the percentage distribu tion of TEC shows a clear northward trend, especially between latitudes 10° and 13°. Figure 4.3b predicts the spatial distribution of VTEC and interpolated VTEC across the region during daytime in 2013, using

Krig ing interpolation. Additionally, Fig. 4.3c presents the variogram estimate distribution of TEC, highlighting semi-variances. These figures reveal a strong spatial distribution of TEC, particularly pronounced at higher latitudes in Ethiopia, gradually decreasing towards lower latitudes. Figure 4.4 depicts a similar sce nario, albeit with different TEC values. While Fig. 4.3 represents daytime conditions with a peak TEC value of 70 TECU, Fig. 4.4 reflects nighttime conditions, showing a lower TEC value of around 20 TECU for the same year, 2013. Figure 4.4b also illustrates signifi cant latitudinal and longitudinal variations in VTEC, with VTEC decreasing westward during daytime in 2013. The peak values are observed between latitudes 8° N to 13° N and longitudes 35° E to 42° E. TEC increases from 30 TECU during the day to 70 TECU, with nighttime TEC values (TECmin) rising from 2 TECU to 16 TECU. Minor enhancements in night time VTEC variation, as shown in Fig. 4.4b, are attributed to the dominance of recombination pro cesses during nighttime, leading to depletion in the region between longitudes 35° E and 40° E and latitudes 7° N to 10° N. The diurnal VTEC pattern follows a consistent trend, rising steadily from sunrise to a maximum in the afternoon, followed by a decline before the next sunrise. This pattern, observed in Ethi opia, reflects typical low-latitude ionospheric charac teristics, with a pre-dawn VTEC minimum and gradual increase throughout the day until reaching a peak in the afternoon, followed by a gradual decrease post-sunset. The predictive capabilities of the Kriging ionospheric model and the spherical variogram effectively capture the spatial distribution of TEC across the region, pro viding valuable insights into ionospheric behavior.

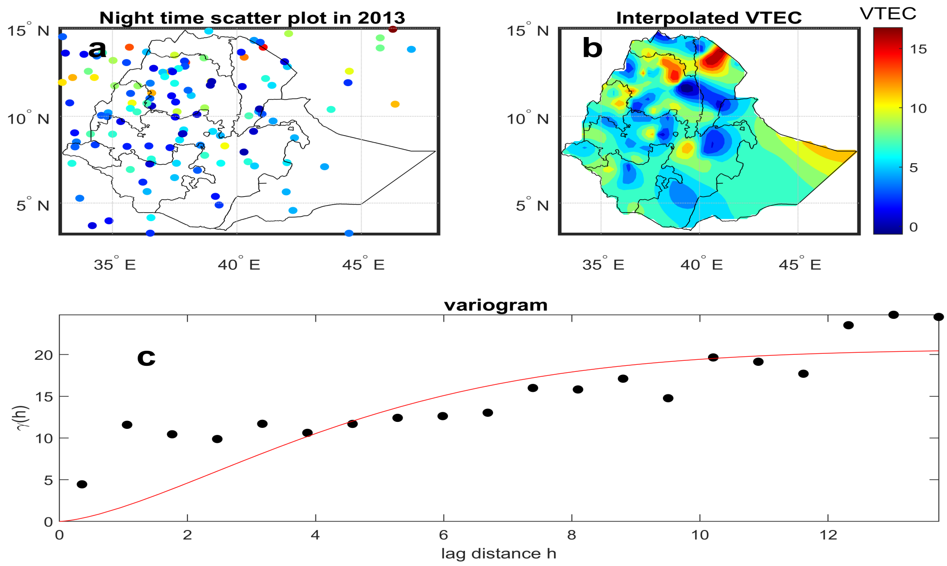

Figure 4.4: Night time VTEC variation estimated by Kriging plot of the average VTEC values during the year 2013. (a) the scattered VTEC observed over Ethiopia ionosphere, (b) the map obtained from Ordinary Kriging interpolation and (c) the spherical var iogram model.

4.2.1 Spatial Variation of TEC and Semivariogram Model Performance

The figure 4.5 presents a series of VTEC contour maps over the Ethiopian sector for selected times in 2012 and 2013 during the quite time. Panels (a) to (c) display TEC distributions for the year 2012 at 6 UT, 12 UT, and 18 UT, respectively, while panels (d) to (f) correspond to the same UT times for the year 2013. A clear diurnal pattern emerges in both years, with VTEC values peaking around local noon (12 UT) and decreasing toward the evening (18 UT) and early morning (6 UT). Specifically, panel (b) for 2012 at 12 UT shows the highest TEC values, exceeding 70 TECU, and a well-defined equatorial ionization anomaly (EIA) structure, particularly evident north of the magnetic equator (Abe et al., 2018). Similarly, panel (e) for 2013 at 12 UT indicates enhanced ionospheric activity, although with slightly lower intensity compared to 2012, reflecting possible variations in solar flux or geomagnetic conditions.

At 6 UT in both years (panels a and d), moderate VTEC levels are observed, indicating residual ionization from the previous day and the early stages of diurnal ionospheric buildup. Panel (a) reveals a localized enhancement over central Ethiopia, while panel (d) shows a more uniform distribution. By 18 UT (panels c and f), the TEC significantly decreases, likely due to post-sunset recombination processes. These evening maps also exhibit patchy low-VTEC regions and irregular structures, which may indicate the presence of equatorial plasma bubbles (EPBs) or ionospheric irregularities common during post-sunset hours. Overall, the 2012 maps suggest slightly higher TEC magnitudes and a more pronounced EIA structure compared to 2013. The spatial variability and evening-time TEC depletion patterns observed in both years are consistent with the expected equatorial ionospheric behavior driven by solar radiation and electrodynamic processes. These findings highlight not only the diurnal evolution of ionospheric TEC but also year-to-year variability likely influenced by changes in solar and geomagnetic activity.

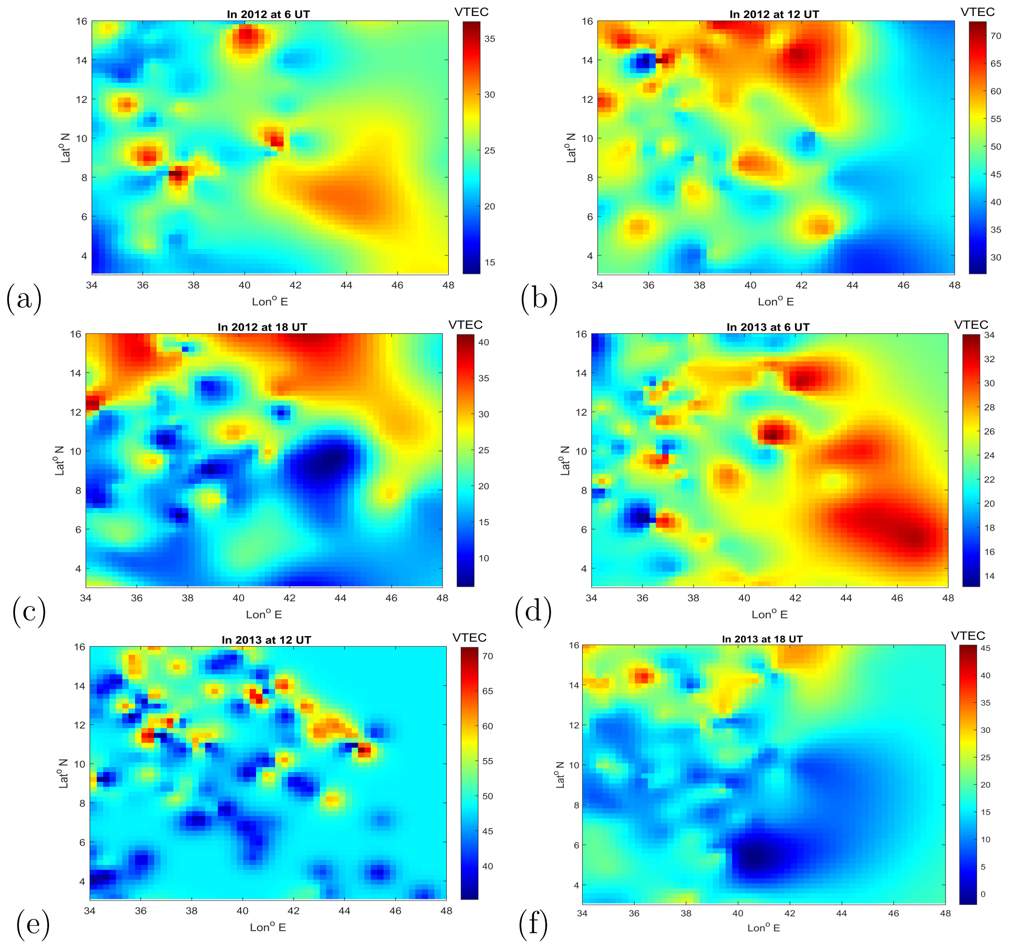

Figure 4.5: The kriging interpolation method was employed to generate latitude and longitude profiles depicting the average VTEC predictions on quiet days throughout the year 2012 at 06:00, 12:00 and 18:00 UT respectively.

Figure 4.6 presents a comparative evaluation of three theoretical semivariogram models Exponential, Gaussian, and Spherical used to fit TEC spatial variances over the region during quiet geomagnetic conditions in 2012 and 2013, at 06:00 UT, 12:00 UT, and 18:00 UT. Each row in the figure corresponds to a specific year, and each column corresponds to a specific time of day. The blue circles represent the observed (empirical) semivariance values, while the red curves represent the modeled fits. The effectiveness of semivariogram models in fitting the experimental semivariogram derived from TEC data was observed. Table 4.1 and 4.2 presents a comparative evaluation of

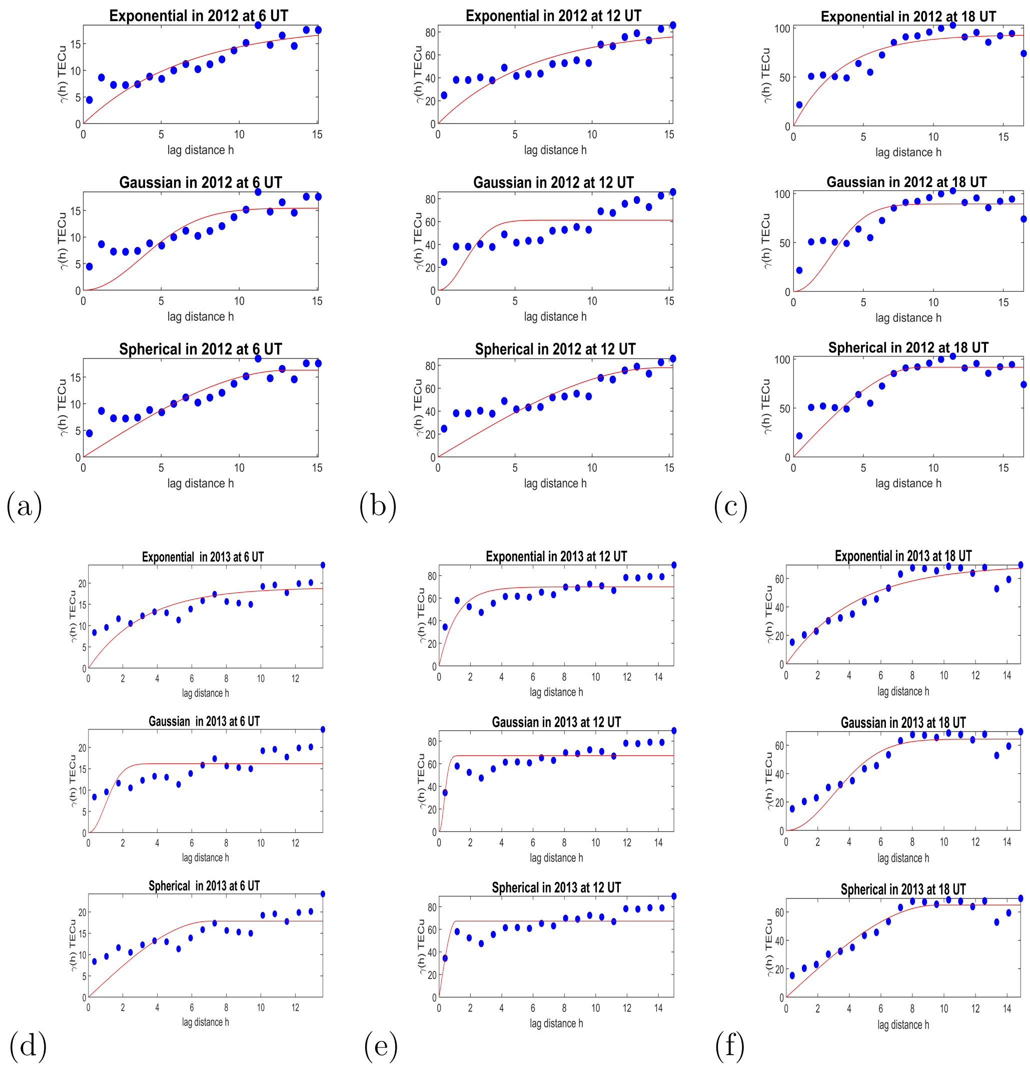

Figure 4.6: Exponential, Gaussian and Spherical semivariogram models used to fit the TEC variances over the region on a quiet days. The blue circles are the observational values and the red curves represents the modeled values at different time in the year 2012 and 2013.

Table 4.1: Comparison of Semivariogram Model Parameters for VTEC Interpolation at 12:00 UT in 2012.

Model	Nugget	Sill	Range (deg)	RMSRes	$\|Q_1\|$
Exponential	0.0452	8.39	6.85	0.1627	0.0081
Gaussian	0.0397	8.65	7.20	0.1453	0.0029
Spherrical	0.0413	8.57	7.10	0.1294	0.0007

three mostly used semivariogram models, Exponential, Gaussian, and Spherical based on their performance in modeling the spatial distribution of VTEC over Ethiopia at 12:00 UT for the year 2012 and 2013. The importance of this comparison is to choice which model provides the most accurate spatial interpolation for VTEC using geostatistical Kriging method. The Range, Sill and Nugget effect, commonly known as the semivariogram parameters, play a key role in the Kriging interpolation process (Cele et al., 2023). Nugget represents the measurement error or micro-scale variation at zero distance. A smaller nugget value suggests higher spatial autocorrelation at small distances. All the three models, shows more closed values as we can observed from table 4.1 and 4.2. The seconde parameter is Sill, it's the value at which the semivariogram levels off, representing the total spatial variability (Amabayo et al., 2021). All three models have similar sill values, indicating similar overall variance captured across the models. The third parameter is Range, it is the distance over which spatial correlation is significant. Beyond this range, spatial locations are no longer correlated. Range is it may be given in degrees of latitude or longitude and want to convert that to kilometers 1 degree of latitude ≈ 111 kilometers. So, to convert degrees latitude to km we have use the formula distance (Range)= $degree \times 111km$. The fourth parameter is Root Mean Square Residual (RMSRes) which measures the residual error between observed and predicted values. A small RMSRes in TEC prediction indicates good predictive performance, accurate modeling, and high agreement between predicted and observed TEC values. As shown in Tables 4.1 and 4.2, the spherical model achieves the lowest RMSRes values among the three models, with 0.1294 in 2012 and 0.1289 in 2013. These minimal residuals indicate that the spherical model provides the most accurate TEC predictions and demonstrates the highest agreement with observed data across both years. The last one is Q1 statistical test. This is a statistical indicator used to validate the model by comparing observed and predicted semivariance values. Smaller Q1 values reflect a better match between experimental and modeled semivariograms. The Spherical model again outperforms the others with the lowest Q1 (0.0007, 0.0008), followed by Gaussian (0.0029, 0.0026) and Exponential (0.0081, 0.0079). Considering all five parameters, especially the RMSRes and $|Q_1|$, which are the most indicative of interpolation accuracy and model fit, the Spherical model emerges as the best-performing semivariogram model for interpolating VTEC data at 12:00 UT in 2012 and 2013. It demonstrates the lowest prediction error and the best alignment with the observed spatial structure of the ionospheric TEC values. This makes it the most suitable choice for geostatistical modeling and analysis in this context. Fig 4.7 shows the results of the correlation analysis of Krig-

Table 4.2: Comparison of Semivariogram Model Parameters for VTEC Interpolation at 12:00 UT in 2013.

Model	Nugget	Sill	Range (deg)	RMSRes	$\|Q_1\|$
Exponential	0.0481	8.34	6.92	0.1592	0.0079
Gaussian	0.0415	8.59	7.18	0.1438	0.0026
Spherrical	0.0432	8.55	7.15	0.1289	0.0008

ing and GPS VTEC for the year 2012 and 2013 respectively. The VTEC values interpolated using the Kriging method exhibit a very strong positive correlation with the GPS-measured VTEC, with correlation coefficients of 0.94 and 0.96. This strong correlation indicates that the generated TEC maps accurately estimate VTEC at locations where direct measurements are unavailable across the region. For this model we have get Root Mean Square Error (RMSE) 2.15 and Mean Absolute Error (MAE) 1.13 TECU. The RMSE and MAE values are relatively low. Errors $\leq$ 3 TECU are often considered acceptable in ionospheric models using GPS, so kriging model approach is working effectively for spatial interpolation of VTEC. This indicates a strong predictive performance and kriging is a reliable method for estimating VTEC spatial distribution in this dataset. Overall, the Kriging method provides a strong predictive model for GPS-VTEC in the analysis.

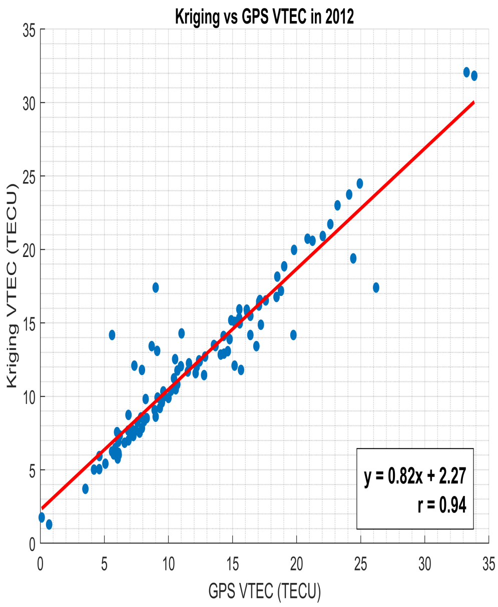

(a)

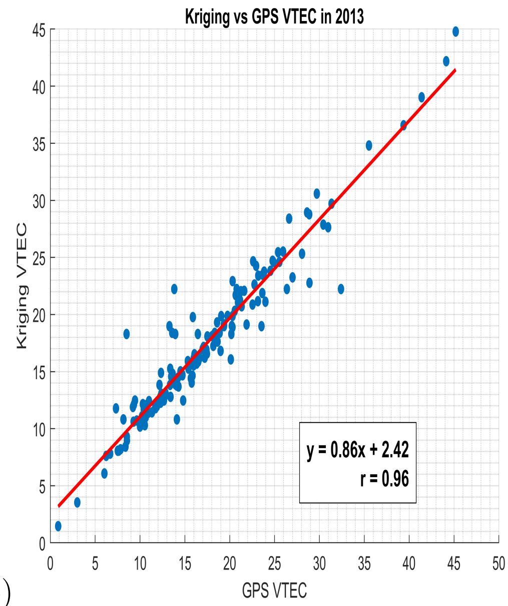

(b)

Figure 4.7: Correlation analysis between Kriging-estimated VTEC and GPS-observed VTEC for the years 2012 and 2013. Scatter plots show the relationship between GPS-VTEC values and Kriging predictions, along with the fitted linear regression lines. The correlation coefficient (r), slope, and intercept of each regression are displayed within the plots, indicating the strength and accuracy of the Kriging interpolation compared to the GPS measurements.

4.2.2 Diurnal Variation of Vertical Electron Content in Ionosphere during the Quiet Days

Figures 4.8a-4.8d present the mass plots of VTEC diurnal variations for the years 2012 and 2013. These plots specifically illustrate the VTEC variations at sev eral stations Asosa, Debark, Shis, Aboo, Metu, Robe, Bdmt, and Armi on days 93, 99, and 270 of each year. The data reveal a clear diurnal pattern, with VTEC values peaking around noon and decreasing during the nighttime hours. This behavior is consistent across the different stations. The sun plays a crucial role in ionospheric dynam ics by emitting a broad spectrum of electromagnetic radiation, along with high-energy particles (Bagiya et al., 2009). According to Sharma et al. (2012), solar activity exerts a direct influence on the ionization lev els in the ionosphere, with higher ionization and thus higher VTEC values occurring during periods of intense solar activity, and lower values during periods of low solar activity. The diurnal variation of VTEC is influenced by several factors, including the time of day, the level of solar activity, and the geographic location specifically the latitude and longitude of the observation stations. Since the stations in question are geomagnetically conjugate, they exhibit similar ionospheric behavior, meaning that the diurnal VTEC patterns observed at these locations are consistent with each other. Figure 4.8 VTEC reaches its maximum value around noon, when solar radiation is most intense and the ionization level in the ionosphere is at its peak. Conversely, the mini mum VTEC values are observed during the nighttime when the absence of solar radiation leads to reduced ionization. This pattern underscores the strong depen dence of VTEC on solar activity and the time of day. This is happened due an Eastward electric field is established in the equator region which creates an upward moving E B plasma flows. The plasma insta bility phenomena occurring in the equatorial region are usually grouped under the generic name ESF. These phenomena happened at night time, and the F-region dynamo drift to Eastward this can affect the VTEC variability and depletion. During the daytime, the dynamo electric fields are Eastward, which causes an upward $E \times B$ plasma drift.

4.2.3 Seasonal Variation of Vertical Total Electron

Content in Ethiopia Ionosphere Figure 4.9 shows the seasonal variation of VTEC at different place over Ethiopia ionosphere in two years 2012 and 2013 at different station namely (Bahir Dar, Debark, Robe, Shis, Arba Minch and Addis). The seasonal mean TEC values are used to study the sea sonal variations of VTEC for each year by grouping a year into four seasons i.e. December solstice, March equinox, June and September equinox. Figure 4.9a is Bahir Dar Station and VTEC is maximum in March and September equinox and minimum in both solstice in the year 2012 and Fig. 4.9b is at Debark for the same year 2012 and VTEC is maximum in September equi nox and June solstice, but the minimum one is observed in March equinox and December solstice. Figure 4.9c is data recorded on Debark in 2013 and the maximum VTEC is occurred in the season of Septem ber equinox and December solstice and mini- mum VTEC is happened in June solstice and March equi nox, but Fig. 4.9d is at Robe for the year 2013 and the maximum VTEC are seen in March equinox and June solstice the minimum is recorded in September equi nox and December solstice. Figure 4.9e is at Shis which recorded in the year 2012 and VTEC is maxi- mum in

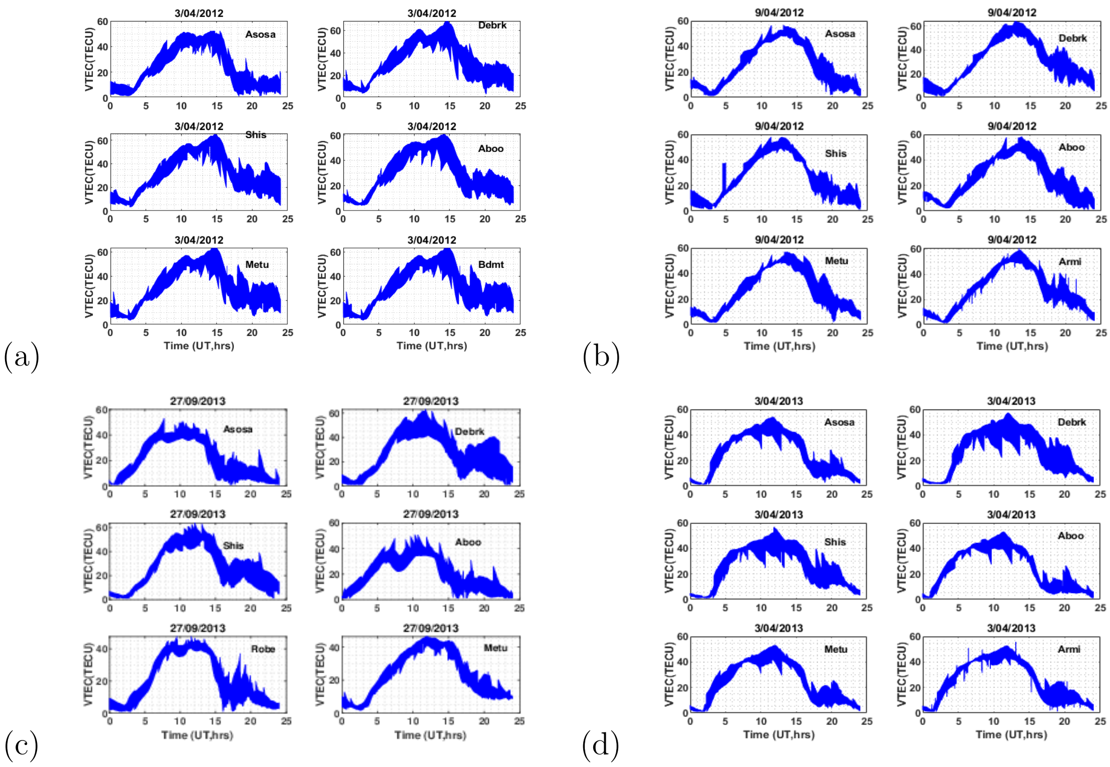

Figure 4.8: . Mass plot of Diurnal variation of Vertical Total Electron Content. The figure shows the VTEC variation over Ethiopias ionosphere during the maximum solar cycle 24 on day 099, 001, 011 and 270 in the years 2012 and 2013. Dates are presented in DD/MM/YYYY format.

September equinox and December solstice for the cause of minimum vTEC March equinox and June solstice are observed. Figure 4.9f is the VTEC observed at Arba Minch in 2013, for this one March equinox and June solstice are the maximum VTEC observed and December solstice and September equinox are the mini- mum VTEC is seen. Figure 4.9g is at Arba Minch in 2012 and the value of VTEC is maximum in the sea son of March equinox and June solstice, but the min imum one is in the season of September equinox and December solstice and the last Fig. 4.9h is at Adis in the year 2012 for this one VTEC is maximum in both sol stices and minimum in both equinoxes. The figure indicates that there is a strong semi-annual variation of VTEC all over the interval. On average the plots depict maxim VTEC in March equinox followed by September equinox and minim in December solstice followed by June solstice.

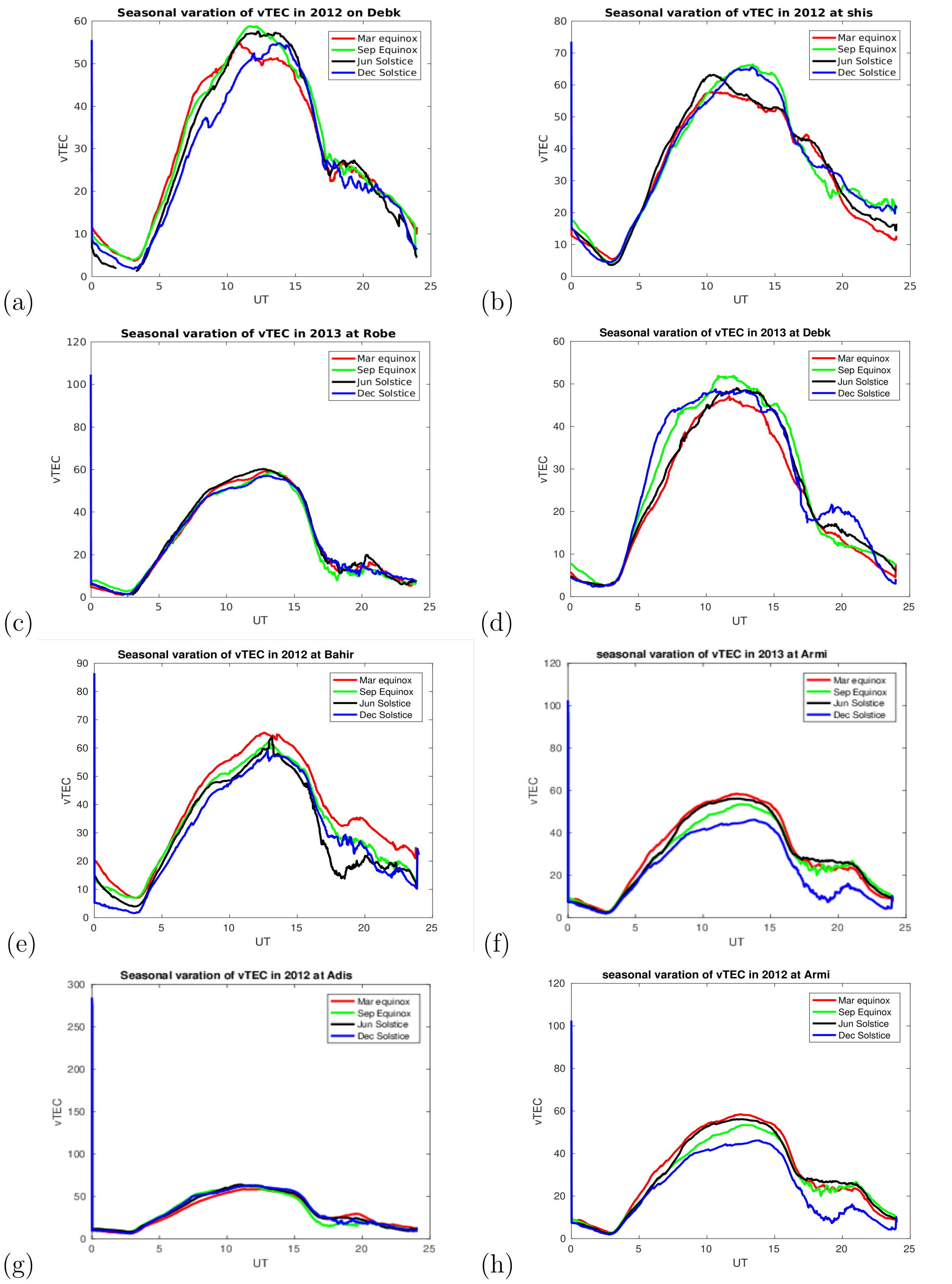

Figure 4.9: Seasonal variation of TEC over different regions of Ethiopia during key solar periods: March Equinox, September Equinox, December Solstice, and June Solstice.

4.3 Summary

1. In this thesis, we studied the modeling of the ionosphere in Ethiopia and its spatial distribution TEC characteristics during the geomagnetic quiet days. It aims to comprehensively study the spatial distribution of VTEC variations in Ethiopia and provide guidance for the study of other regions.

2. Our study meticulously examined the fluctuations of VTEC in Ethiopias ionosphere, spanning various time scales and geographical regions. By employing the OK interpolation technique over two years o f data from 2012 to 2013, we gain ed com pre hen-sive insights.

3. Our observations highlighted a clear pattern:VTEC peaks around noon and dips during nighttime,influenced by an Eastward electric field in the F-region.Through VTEC maps, we illustrated the enhancement during the day (up to 70 TECU) and its decline at night (14 TECU).

4. We pinpointed maximum VTEC concentration in the northeast (between 10° to 13° latitude and 36° to 45° longitude) and reverse depletion in specific areas(5° to 8° latitude and 30° to 46° longitude). Our use of the OK interpolation method proved effective in cap-turing these nuances, particularly suited for short distance data.

5. The diurnal variation of VTEC in the ionosphere during quiet days disclose consistent TEC distribution across all nine stations, as they are geomagnetically conjugate to each other in the region.

6. In essence, our study sheds light on the intricate dynamics of VTEC in Ethiopias ionosphere, offering valuable insights for future research and practical applications in understanding space weather phenomena

Chapter 5

Characterization of equatorial plasma bubbles over the East African Sector using the ROTI and sTEC depletion depth

5.1 Introduction

The Earth's ionosphere is significantly influenced by space weather conditions, and the resulting changes play a crucial role in understanding the harmful effects on the ionosphere (Seif and Panda, 2023). Consequently, researchers studying the ionosphere find the propagation of ionospheric irregularities during space weather events to be an intriguing subject (Vankadara et al., 2022). During the night, the lower ionosphere quickly decays, and the raised F-layer's bottom side experiences a vertical density gradient (Kelley, 2009). At the magnetic equator, the electron density in the F_2 ionospheric region rapidly rises to higher altitudes in the evening sector due to an upward plasma $E \times B$ drift, known as the PRE (Farley et al., 1986; Haerendel et al., 1992; Heelis, 2004; Heelis et al., 1974). This plasma drift also triggers plasma instability on the bottom side of the F-region through the well-known RTI mechanism (Huba and Ossakow, 1981; Sultan, 1996). This creates the standard configuration for RTI, where a heavy fluid is positioned on top of a lighter one. However, the F-layer height and bottom side density gradient are not the only conditions necessary for RTI. Driven by the RTI, large-scale EPBs manifest as post-sunset ionospheric irregularities in the equatorial F-region (Gentile et al., 2006; Li et al., 2021). These EPBs possess the potential to disrupt the propagation of radio waves, leading to fluctuations in signal strength, phase, and arrival time (Pedatella et al., 2024). Consequently, they can introduce inaccuracies in navigation systems and disrupt radio wave communication, affecting applications such as GPS navigation, satellite communication, and terrestrial broadcasting. These disruptions caused by EPBs, known as scintillations, present challenges for the reliable and efficient operation of these systems, especially in regions where EPBs are prevalent, such as the equatorial and low-latitude ionosphere (Chen et al., 2008). These scintillation levels in the ionosphere are commonly identified using the amplitude and phase scintillation indices to detect ionospheric irregularities (Acharya and Majumdar, 2019; Carrano et al., 2019; Li et al., 2020a; Manga et al., 2021). Scintillation is more prominent after sunset and during midnight hours (Vankadara et al., 2022). It degrades the accuracy and reliability of space-based positioning and navigational operations, such as the GNSS, by causing signal fading, cycle slips, signal distortion, interruptions, or loss of lock (Carmo et al., 2021; Gentile et al., 2006; Magdaleno et al., 2017; Mendillo et al., 2001).

The ROTI is utilized to measure the level of irregularities because ROTI and S4 indices exhibit excellent agreement, both during quiet and disturbed geomagnetic conditions (Babu Sree Harsha et al., 2020; Seif and Panda, 2023; Seok et al., 2022; Vankadara et al., 2022). EPB occurrences are found to be dependent on various factors, including the time of day, month, season, latitude, longitude, solar cycle, and conductivity of the E-region (Kepkar et al., 2020; Kumar et al., 2016). It has been demonstrated that the frequency of EPB events varies with solar activity and is higher during years with high solar activity (Pimenta et al., 2001; Sahai et al., 2000; Smith and Heelis, 2017; Sobral et al., 2002). EPBs are considered to occur when the observed TEC depletions from a satellite exceed 5 TECU and exhibit an apparent duration between 10 minutes and 180 minutes (Portillo et al., 2008). Kumar and Chen (2016) examined the influence of solar and geomagnetic activity on the occurrence of equatorial plasma bubbles over Hong Kong from 2001 to 2011, utilizing GNSS data. They reported that plasma bubbles exhibited peak occurrences during the equinox months throughout the study period, except during the low solar activity phase from 2007 to 2009. Over the years, several techniques such as radar observation, ionogram analysis, in-situ satellite measurements, radio scintillation, airglow observation, and satellite-based measurements have been employed to study the characteristics of plasma bubbles (Abiriga et al., 2020; Kumar and Chen, 2016; Portillo et al., 2008).

The primary objective of this study is to characterize ionospheric irregularities and examine the occurrence rate of EPBs. Specifically, it focuses on utilizing ROTI and analyzing the depletion depth of sTEC as key indicators of EPB activity, exploring the diurnal, monthly, and seasonal variations of EPBs under quiet geomagnetic conditions ,and employing data from two stations located near the geomagnetic equator during the second phase of solar cycle 24 maximum year.

5.2 Results and discussion

Based on GPS data, ROTI, and solar index characteristics, we were able to identify the occurrence of ionospheric irregularities over ADIS and RCMN stations in 2015. The analysis of EPB occurrences in this work is for quiet days only for $kp < 3$ and $Dst > -30$ nT.

5.2.1 Diurnal depletion of sTEC and Occurrence of EPB

Fig. 5.1 from (a- d) shows the hourly average of sTEC, ROTI values, depletion depth of sTEC, Dst, and Kp index on March 30 in 2015 over ADIS station. In similar ways from Fig. 5.2 and Fig. 5.3, we have seen the original sTEC, ROTI, dsTEC, and the Dst with Kp index for RCMN and ADIS in 2015 from (a- d) respectively. Note that while sTEC, ROTI, and dsTEC are specific to the stations, the Dst and Kp indices represent global geomagnetic activity, and are not tied to individual locations. As shown in Fig. 5.1(a), sTEC fluctuations occur between 18:00 and 19:00 UT (21:00-22:00 LT), corresponding to the post-sunset to pre-midnight period. During this interval, a marked increase in ROTI is observed Fig. 5.1(b), accompanied by a TEC depletion reaching approximately 15 TECU, as illustrated in Fig. 5.1(c). Fig. 5.1d shows the Dst and Kp values also approximately -24 nT and 0.7, at 18:00 to 19:00 UT (21:00 to 22:00 LT) respectively. Fig. 5.2 and Fig. 5.3 also show the same behavior, which means perturbation of sTEC start at 20:00 UT (23:00 LT) ends up at 21: UT (24:00 LT) for Fig. 5.2 and more variable at 19:00 to 21:30 UT (22:00 to 00:30 LT for Fig. 5.3. For Fig 5.2 and Fig 5.3 the Dst and Kp values around -5 nT and 1.5 consecutively. As we can see from those figures dsTEC and ROTI values are the maximum and also minimum together in each case (Li et al., 2020b). The depletion with a magnitude greater than 5 TECU and apparent duration between 10 minute and above can be considered as a plasma bubble occurrence and below 5 TECU there is no plasma bubble observed (Mersha et al., 2020; Portillo et al., 2008). Similar to Fig 5.1-5.2 and 5.3, Fig. 5.4 depicts the sTEC, dsTEC, and ROTI computed by hourly average, from (a- d) for both ADIS and RCMN stations on March 13, and July 20 in 2015 using PRN 12 and PRN 27 respectively.

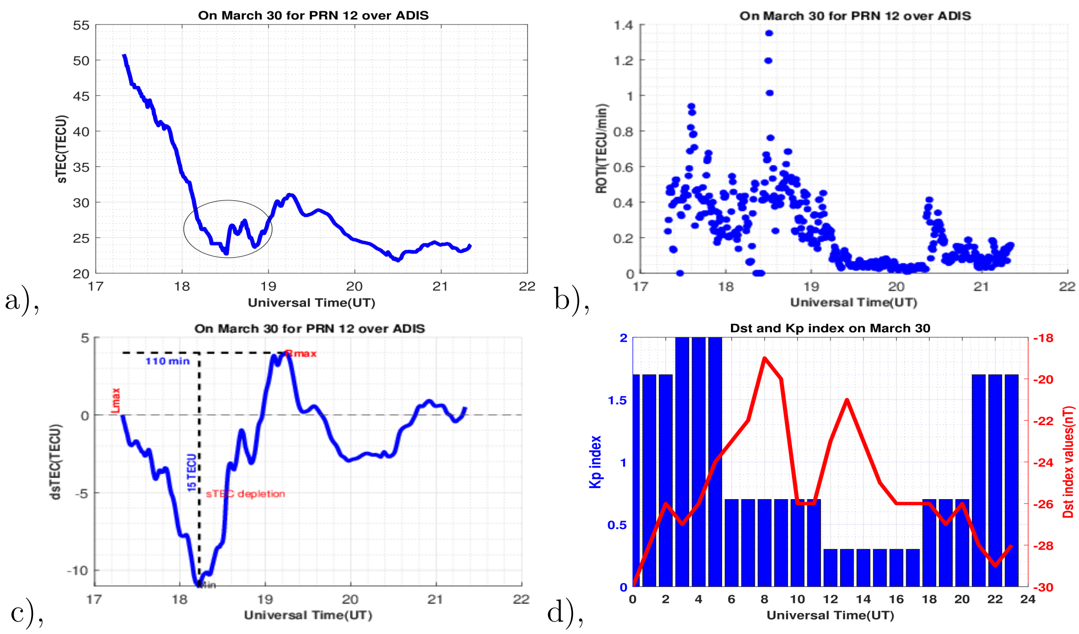

Figure 5.1: The study of diurnal ionospheric irregularities based on the ROTI and detrended sTEC values at ADIS station. (a) the observed sTEC, (b) the daily ROTI value, (c) the detrended sTEC in TEC unit, (d) Dst in nT and Kp index for the quiet days on March 30 in the year 2015 using PRN 12.

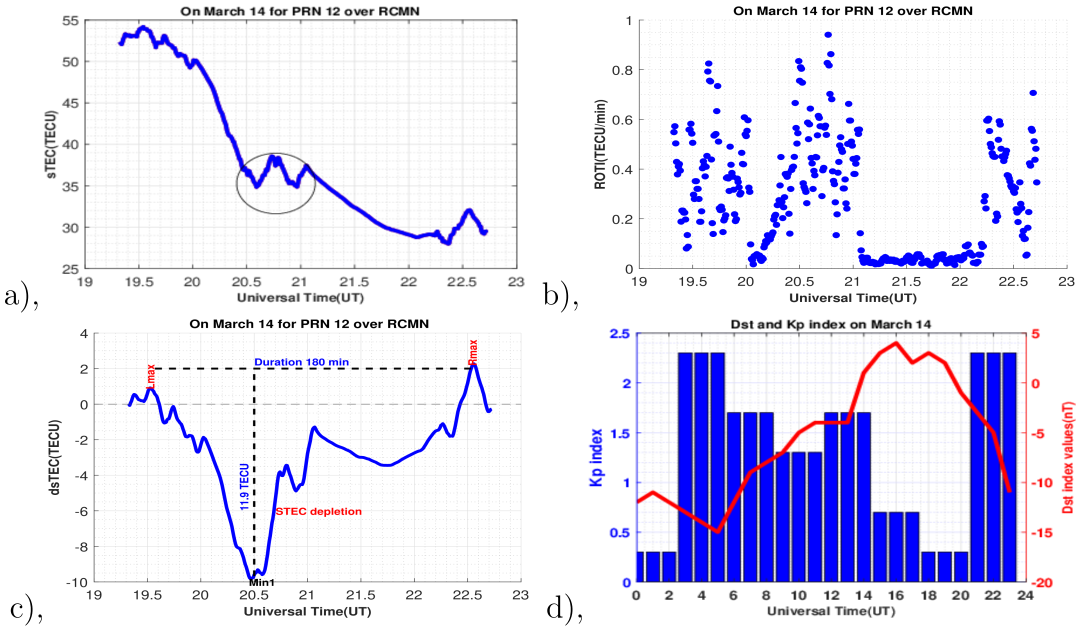

Figure 5.2: The study of diurnal ionospheric irregularities based on the ROTI and detrended sTEC values at RCMN station. (a) The observed sTEC, (b) the daily ROTI value, (c) the detrended sTEC in TEC unit, (d) Dst in nT and Kp index for the quiet days on March 14 in the year 2015 using PRN 12.

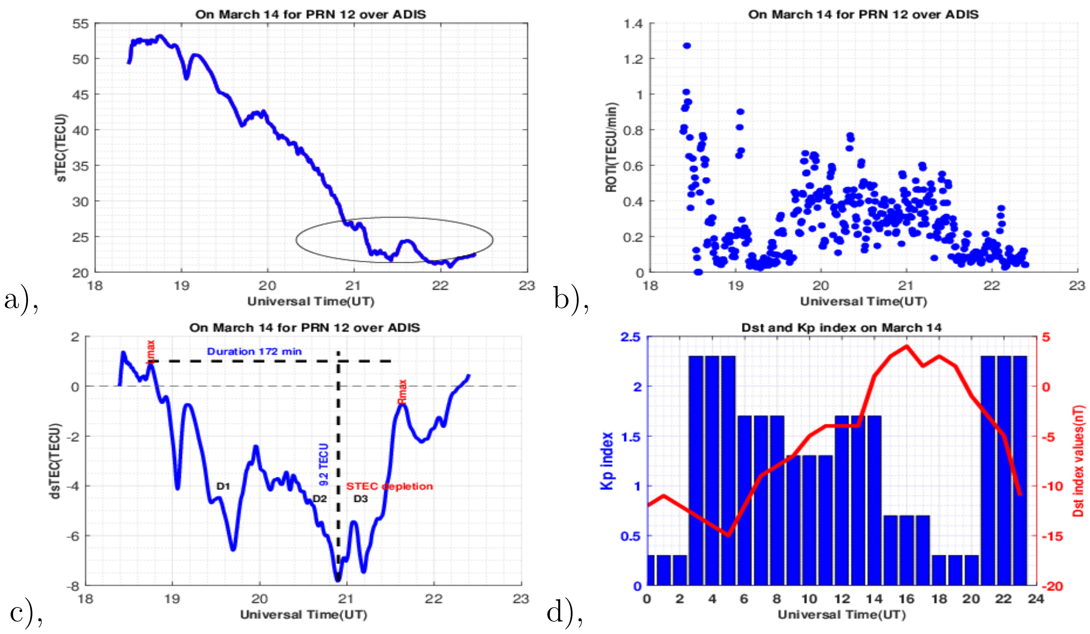

Figure 5.3: The study of diurnal ionospheric irregularities based on the ROTI and detrended sTEC values at ADIS station. (a) The observed sTEC, (b) the daily ROTI value, (c) the detrended sTEC in TEC unit, (d) Dst in nT and Kp index for the quiet days on March 14 in the year 2015 using PRN 12.

Fig. 5.4 (a) first panel shows the hourly average sTEC,the second panel dsTEC and the third panel ROTI. From this figure some fluctuation observed between 19:00 to 21:00 UT (22:00 to 24:00 LT) and Fig. 5.4, (b), (c), and (d) shows similar properties

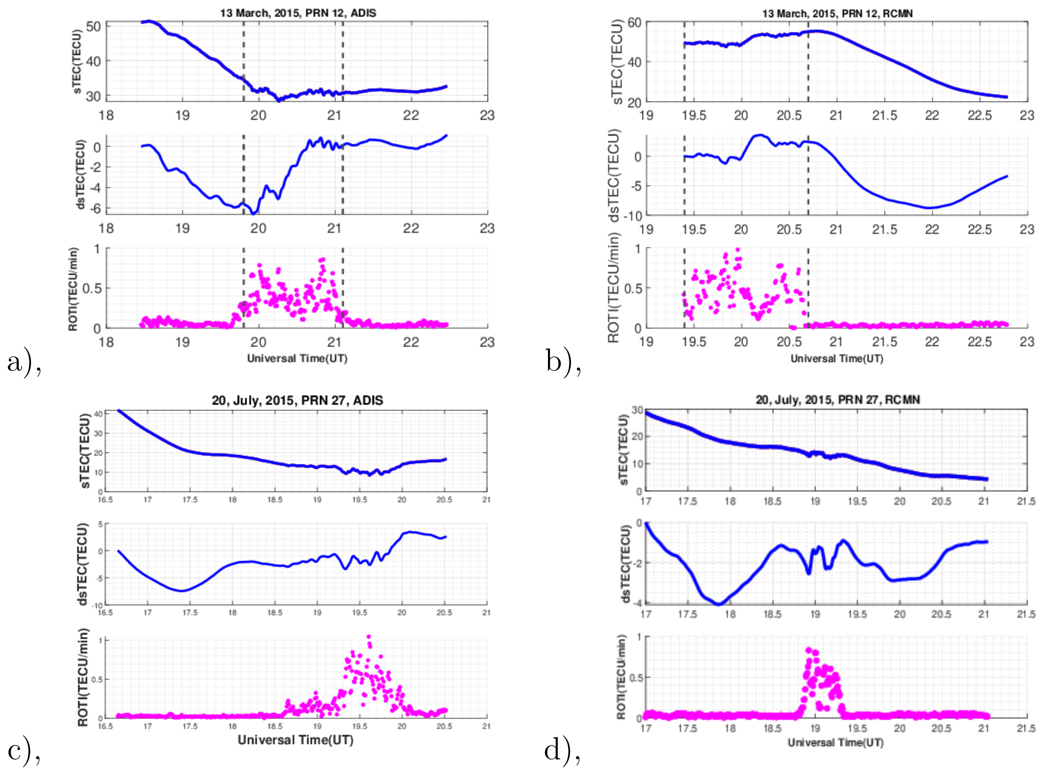

Figure 5.4: The time series of sTEC fluctuation observed, dsTEC and ROTI to detect ionospheric irregularities on March 13 at PRN 12, July 20 at PRN 27 for both ADIS and RCMN stations from (a- d) respectively.

with figure 5.4 (a). The TEC along the ray paths to these satellites showed strong evidence of TEC depletions during the nights of the days presented in Fig.5.2 to 5.4. TEC depletions are evident from 19:50 to 21:00 UT (22:50 to 24:00 LT) (Fig.5.4a), 19:20 to 20:40 UT (22:20 to 23:40 LT) (Fig.5.4b), 19:00 to 20:00 UT (22:00 to 23:00 LT) (Fig.5.4c) and 18:50 to 19:20 UT (18:50 to 23 LT) (Fig.5.4d). Increased fluctuation of ROTI was observed between 18:00 UT and 21:00 UT (21:00 LT and 24:00 LT), as shown in Figures 5.1, 5.2, 5.3, and 5.4. The selected days are considered geomagnetically quiet when the magnitude of the Dst index is < 50 nT and the Kp index ≤ 3. During these quiet periods, more EPBs were observed, as evidenced by the parameters ROTI, dsTEC, Dst, and Kp indices. The sTEC fluctuations, depletion depth of sTEC, and ROTI values exhibit consistency, aligning with each other over the same time period. These fluctuations corresponded with dsTEC and the average values of sTEC. The diurnal variability of ROTI is likely due to changes in sTEC, which are influenced by the intensity of incoming solar radiation. Higher solar activity results in increased ionization, leading to higher sTEC levels, whereas lower solar activity reduces ionization, resulting in lower sTEC levels. These TEC depletions confirm the presence of small scale irregularities trapped in large scale irregularities, which are responsible for scintillations over the different ray paths. At

GPS L-band frequencies, plasma irregularities with scale-sizes of a few hundred meters can be detected. However, under conducive ionospheric environments, small scale irregularities can grow along geomagnetic field lines to form the EPBs with dimension of few hundred kilometers. EPBs are generally regions of electrically charged particles which develop as flux tubes aligned vertically, and then rising slowly in the upper atmosphere. The dsTEC typically involves removing long-term variations from the sTEC data and can help in isolating short-term irregularities in the ionosphere, which are of interest for studying phenomena like ionospheric storms, scintillation, plasma bubbles or other dynamic processes. As the sTEC fluctuates, there are ionospheric irregularities, which are detected by ROTI in this work, and depletion of sTEC is observed because of the irregularities. The ionospheric density gradient around sunset hours is also observed to have a vital role in affecting the evolution of post-sunset ionospheric irregularities (Li et al., 2008; Tiwari et al., 2013). Because ROTI detects large-scale ionospheric irregularities structures and maximum when the ionospheric electron density depleted. The depletions usually occur after sunset with a duration of several tens of minutes (Paznukhov et al., 2012; Qiang et al., 2021).

5.2.2 Monthly occurrence of ionospheric irregularities

The monthly occurrence of ionospheric irregularities can be analyzed using ROTI. In this study, data from various PRN numbers were examined specifically between 17:00 and 23:00 UT (20:00 to 2:00 LT) peak values were observed. The analysis of monthly ROTI occurrences for both stations in the year 2015 has been shown in Fig.5.5 and Fig.5.6. The different colors in Fig 5.5 and 5.6 represent various PRNs are used in the analysis of ROTI values. The dashed lines indicate the minimum ROTI threshold values is 0.5 TECU. Fig 5.5 and 5.6 illustrate that the highest occurrence of ROTI is observed in February, March and April. This indicates that ionospheric irregularities are most frequent during these months, while other months exhibit relatively lower levels below ROTI ≤ 1 of ionospheric disturbances. These findings are consistent with previous studies on ionospheric scintillation, such as the report by Vankadara et al. (2023), which also highlighted increased occurrences of ionospheric irregularities during this period. The high occurrence of ionospheric irregularities in February, March and April can be attributed to its status as an equinoctial month, during which the magnetic meridian is closely aligned with the solar terminator. ROTI is an indicator for the occurrence of ionospheric irregularities, these ionospheric irregularity occur inside and around EPB. Table 2 delineates ionospheric irregularities by their corresponding ROTI values, systematically categorizing them into distinct levels (Vankadara et al., 2022). ROTI ≤ 0.25 is no irregularity, $0.25 <$ROTI< 0.5 is weak irregularity, $0.5 \leq$ ROTI < 1 is moderate irregularity and ROTI≥ 1 is strong irregularity (Vankadara et al., 2022). These classifications serve to clarify the varying degrees of ionospheric disturbances, providing a comprehensive depiction of the dynamic nature of the ionosphere. By employing this stratification based on ROTI values, the table offers valuable insights into the intensity and extent of ionospheric perturbations, aiding in the characterization and understanding of space weather phenomena. Ionospheric irregularities and their associated fluctuations in the ROTI occur most frequently during the post-sunset period due to a combination of electrodynamic and plasma instability processes. One of the key drivers is the PRE of the eastward electric field, which intensifies just before sunset, lifting ionospheric plasma to higher altitudes (Fejer et al., 1999). At these higher altitudes, recombination rates are lower, leading to a strong plasma density gradient between the bottomside and topside ionosphere. As the Sun sets, ionospheric plasma at lower altitudes rapidly recombines, while the higher-altitude plasma remains dense, setting the stage for the RTI, a key mechanism responsible for the development of EPBs (Kelley, 2009). These plasma bubbles rise and expand, creating regions of strong electron density variations that contribute to ROTI enhancements. Additionally, neutral winds and ion-neutral interactions play a crucial role in modifying electric fields and influencing the growth of ionospheric irregularities (Abdu, 2001). Zonal and meridional winds can either enhance or suppress the development of plasma depletions, affecting the spatial and temporal distribution of irregularities. The occurrence of these disturbances is also influenced by geophysical factors such as geomagnetic activity, solar flux, and seasonal variations. Increased solar activity and geomagnetic storms can intensify irregularities by increasing ionization levels and altering the electrodynamic environment. Since ROTI is a measure of the variability of TEC, it is highly sensitive to these irregularities, especially during the post-sunset period when plasma structuring is most pronounced.

Table 5.1: Determining level of ionospheric irregularities observed.

ROTI values	Strength of irregularities
ROTI ≤ 0.25	No irregularities
$0.25 <$ ROTI < 0.5	Weak irregularities
$0.5 \leq$ ROTI < 1	Moderate irregularities
ROTI ≥ 1	Strong irregularities

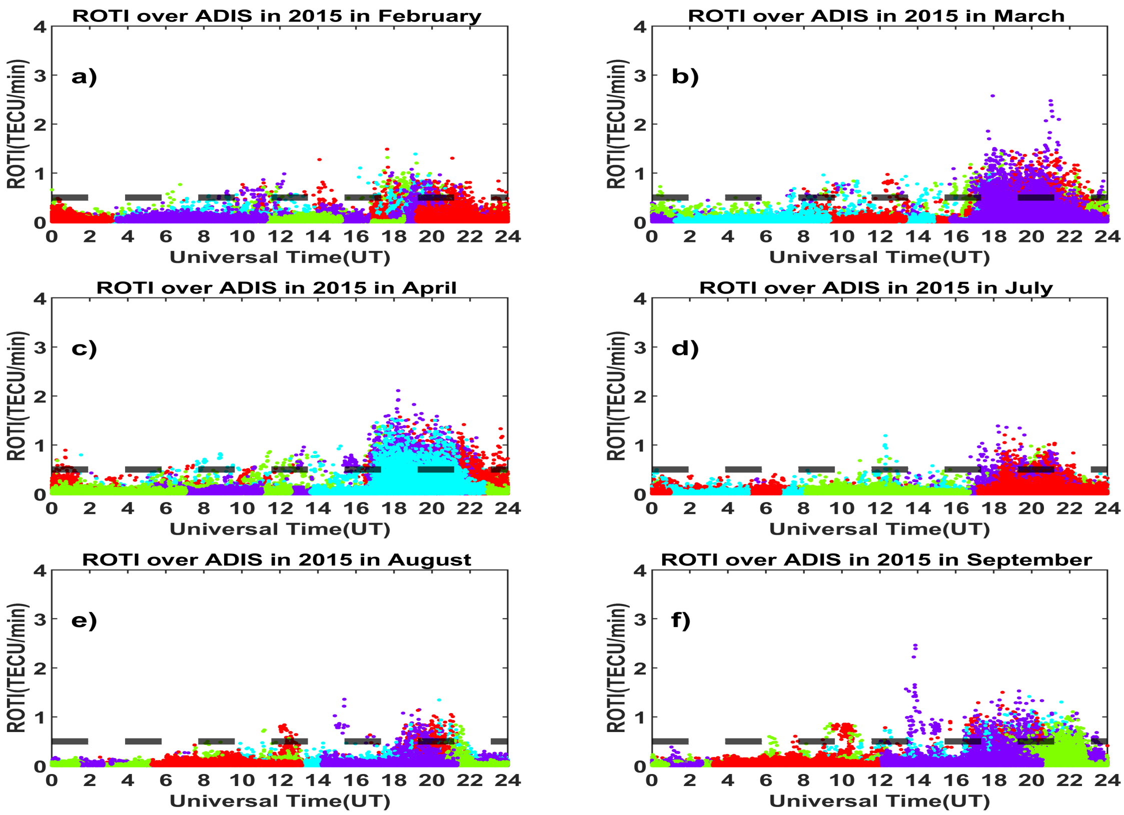

Figure 5.5: Monthly ROTI index proxy for ionospheric irregularities occurrences. The monthly computed ROTI fluctuations for ADIS GPS stations in 2015 in each months were, (a) February, (b) March, (c) April, (d) July, (e) August, and (f) September.

5.2.3 Monthly and seasonal occurrence of EPB during the quiet time.

The monthly distribution of EPBs over ADIS and RCMN exhibits a strong dependence on seasonal variations. Analysis of GNSS-derived ROTI and sTEC fluctuations indicates that peak EPB occurrences are observed during March equinox and September equinoxes. Lowest EPB occurrences are recorded during the June solstice and show minimal activity in December solstice months. As we can observe from Fig 5.7 (a) and (b) the sTEC value get maximum around 10 to 14 UT, because the increase in TEC during daytime is primarily driven by solar radiation, particularly in the form of UV and X-ray radiation, which ionizes neutral particles in the ionosphere, releasing free electrons and contributing to higher electron densities. The electron density is maximum during noon hours, due to the motion of charged particles in side ionosphere. In the reverse during night time they return to their original place and attached to atoms or molecules as result recombination is dominate the phenomena, then after EPBs triggered and ionospheric irregularities produced. Kumar et al. (2016) report that monthly EPB occurrences shows an equinoctial maximum. Fig.

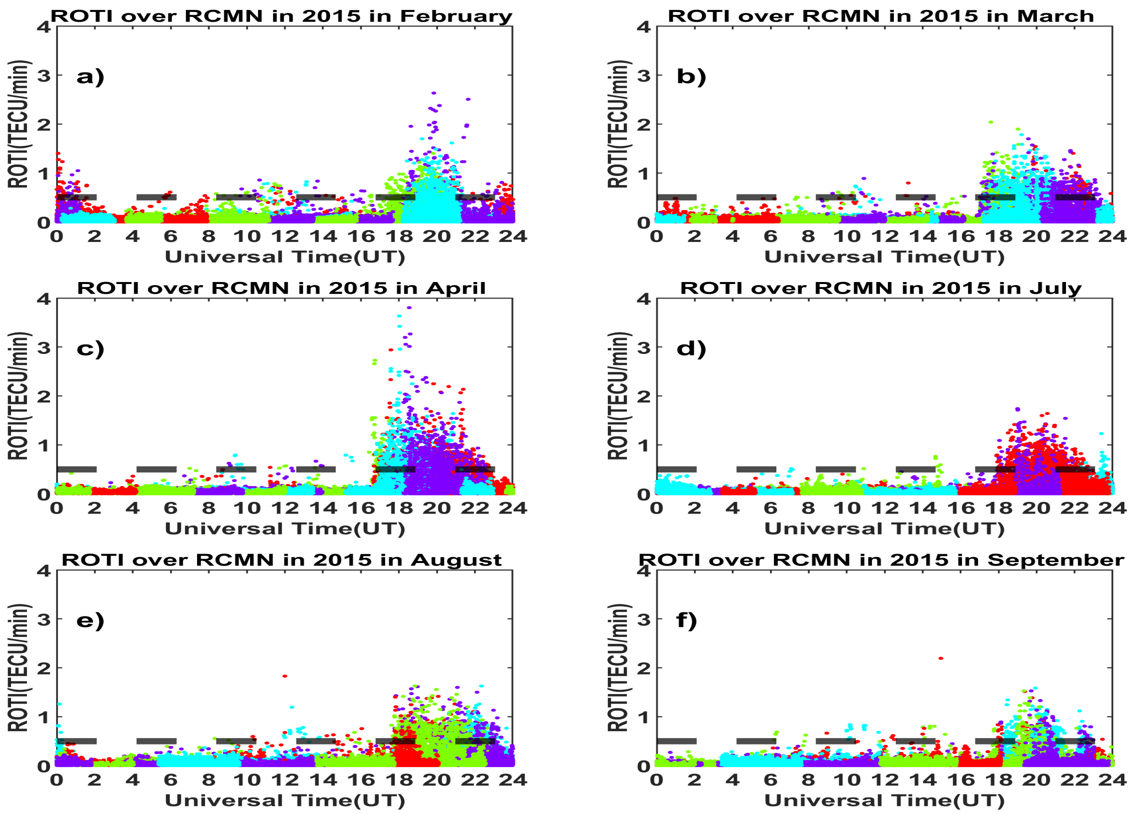

Figure 5.6: Montly ROTI index proxy for ionospheric irregularities occurrences. The monthly computed ROTI fluctuations for RCMN GPS stations in 2015 in each months were, (a) February, (b) March, (c) April, (d) July, (e) August, and (f) September.

5.8 (a) is the sTEC variation during the season, the seasonal depletion of sTEC and the percentage occurrence of plasma bubbles over ADIS in 2015 respectively. In the same way Fig. 5.8 (b) the first, the second and third panel over RCMN 2015 respectively. In this case, the depth of EPBs shows a maximum during March equinoxes and minimum during solstices. During periods of high solar activity, the occurrence of EPBs was significantly higher during equinoxes than solstices. This enhancement is attributed to the near zero solar zenith angle at the receiver stations, leading to increased ionization in the ionosphere (Huba and Ossakow, 1981). The enhanced ionization generates stronger daytime electric fields, which, after sunset, contribute to the PRE of the eastward electric field (Fejer et al., 1999). The PRE drives vertical plasma drifts in the equatorial region, creating favorable conditions for the development of RTI, which subsequently triggers EPB formation (Kelley, 2009; Woodman and La Hoz, 1976). As a result, equinox seasons provide the most suitable environment for plasma bubble generation due to the alignment of the solar terminator with the geomagnetic field, reinforcing ionospheric instabilities (Abdu, 2005; Yeboah et al., 2019). The seasonal values of EPB and scintillation activity is controlled by

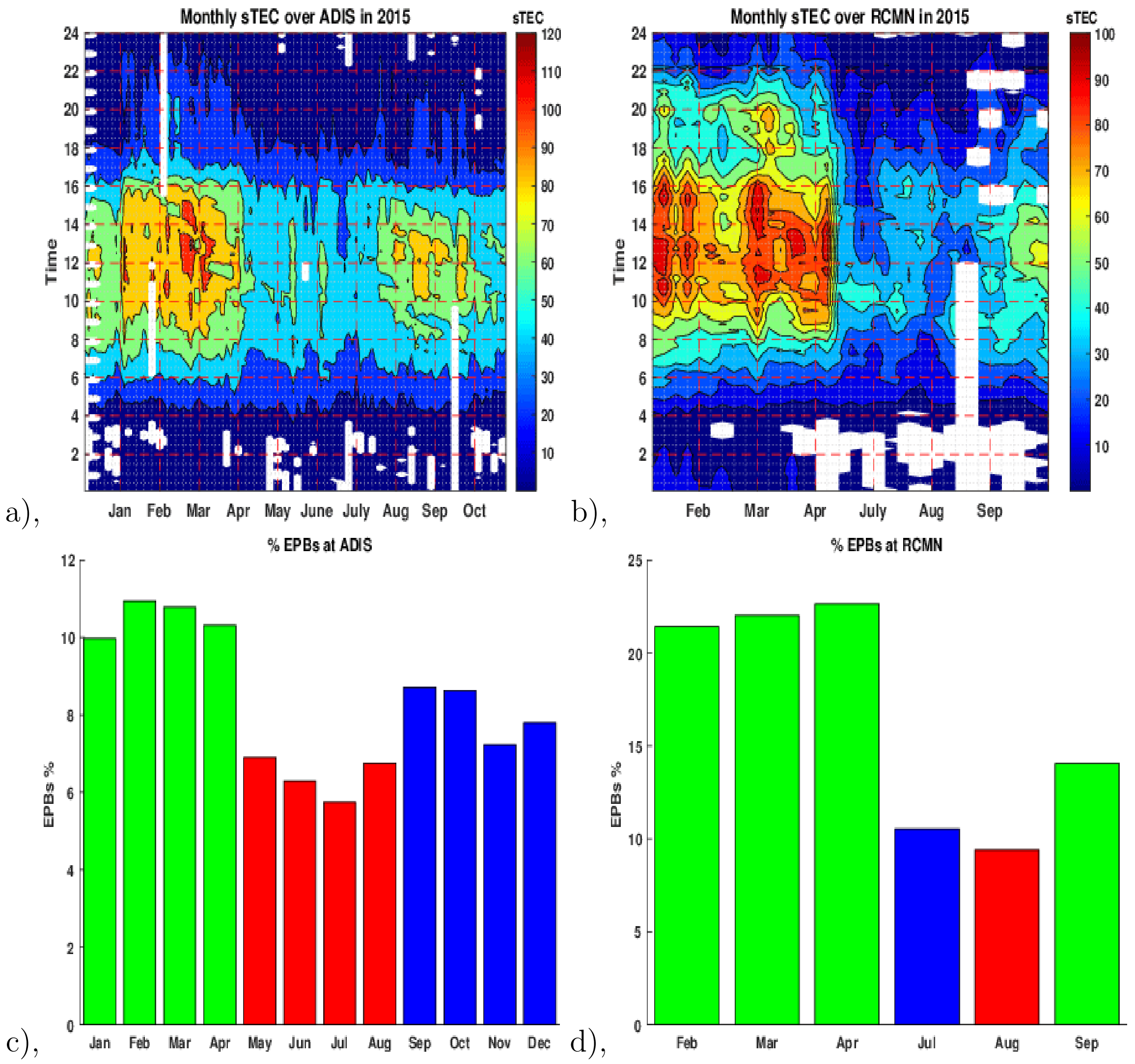

Figure 5.7: Figure 5.7a and 5.7b are the sTEC observed in each month, figure 5.7c and 5.7d were the occurrence of equatorial plasma bubbles in each month for ADIS and RCMN stations respectively.

the magnetic declination angle or the angle between magnetic meridian and solar terminator.

The percentage occurrence of EPBs during the equinoxes periods was high due to the alignment of the geomagnetic flux tubs with the solar terminator (Tsunoda, 1985). The statistical analysis of EPB made by different researchers have shown the occurrence probabilities of plasma bubbles has peaks at night but does not become zero until the morning sector. Kumar et al. (2016) said that the occurrence of plasma bubbles are maximum during the solar maximum years, however this may change due to the occurrence of geomagnetic storm and other sudden occurrences of solar activities. Fig. 5.8 is an illustration of the seasonal variation of EPBs for the couple of stations. The plot shows the plasma bubbles occurrence rates, in March equinox, June solstice, December solstice and September equinox seasons. The EPB occurrence is

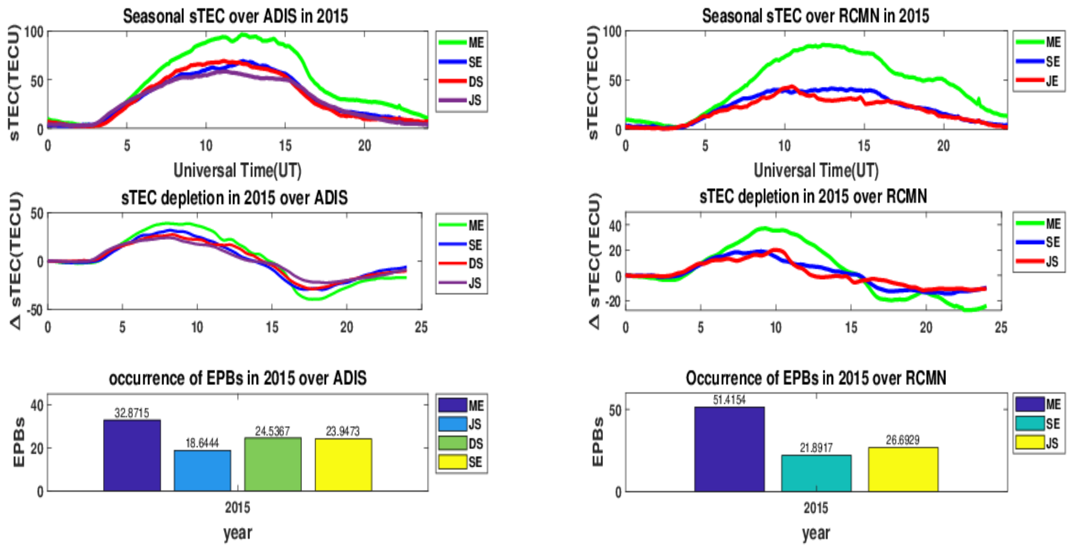

Figure 5.8: Seasonal variations of plasma bubbles for the two stations. The average percentage occurrence of EPB for the stations in March equinox, September equinox and June solstice are observed on the figures.

observed in March equinox with rates of over 33%, December solstice with rate 25%, September equinox 24% and June solstice with rate 19% for ADIS station and March equinox with rates of over 52%, September equinox 22% and June solstice with rate 27% for RCMN station respectively.

The EPBs at RCMN is more significant than ADIS as we can observe from the Fig 5.7 and Fig 5.8, because RCMN is located near the Equatorial Ionization Anomaly (EIA) crest, where the plasma density is significantly higher due to the fountain effect. EPBs originate at the magnetic equator due to the RTI, but their intensity and impact can sometimes be greater at EIA. This occurs due to several key factors.

First, EPBs propagate poleward along geomagnetic field lines, and as they move away from the equator, they can expand and intensify due to changes in plasma density and electrodynamic forces (Woodman and La Hoz, 1976). The growth rate of the RTI, which drives EPB formation, also varies with latitude, solar activity and geomagnetic conditions may have influenced the EPB dynamics. The thermospheric winds, meridional neutral winds, and geomagnetic disturbances could have enhance the latitudinal extent of EPBs, leading to stronger activity at RCMN compared to ADIS. At EIA, neutral wind effects, background ionization levels, and plasma density gradients can sometimes create more favorable conditions for EPB amplification (Basu et al., 2001).

Additionally, the geometry of Earth's magnetic field plays important role. Near the equator, EPBs drift vertically, but at EIA, they can spread more effectively along field lines, leading to larger and more structured plasma depletions (Tsunoda, 1985). The steep plasma density gradient at the EIA crest enhances EPB development. Since EPBs originate from RTI, regions with a stronger density gradient tend to experience more intense EPB activity than those near the geomagnetic equator (Fejer et al., 1999).

Seasonal and longitudinal variations also contribute to the enhancement of EPBs at EIA. Certain regions, such as the African and South American sectors, experience stronger EPBs due to unique geomagnetic and ionospheric conditions at EIA than equator. During periods of high solar activity, increased ionization can further amplify EPBs at EIA, sometimes exceeding their strength at the equator.

EPB is stronger at EIA due to favorable instability growth conditions, poleward expansion, magnetic field constraints, magnetospheric and thermospheric influences, plasma density gradient, post-sunset electrodynamics, and regional ionospheric variations. Overall, the integration of plasma density enhancement at the EIA crest, stronger instability growth, and favorable electrodynamic conditions contributed to greater EPB activity at RCMN than at ADIS in 2015. Understanding these dynamics is crucial for predicting space weather effects and mitigating EPB related disruptions in communication and navigation systems (Kelley, 2009).

5.3 Summary

In order to understand the phenomenon of ionospheric irregularity, the quiet-timed EPBs over East Africa stations are located at geographic coordinates: latitude 9.035°N, longitude 38.766°E for ADIS, and latitude −1.221°N, longitude 36.893°E for RCMN. In terms of geomagnetic coordinates, ADIS is at 5.35°N, 112.51°E, while RCMN is at 4.42°S, 109.06°E, were investigated in this study. The study's main findings are as follows:

1. EPBs and ionospheric irregularities are frequent in the East African region, significantly impacting space weather during 2015.

2. Parameters like dsTEC, ROTI, Dst, and Kp effectively identify EPBs in quiet geomagnetic conditions.

3. Detrended sTEC curves and depletion depths are key tools for identifying and characterizing EPBs with high precision.

4. Data from ADIS and RCMN reveal the influence of geographic and geomagnetic coordinates on EPB formation.

5. Solar terminator effects and geomagnetic conditions strongly influence EPB occurrence and behavior.

6. EPBs peak at night 17:00-22:00 UT (20:00 to 1:00 LT) and during equinoxes, especially March, due to solar terminator and geomagnetic meridian alignment.

7. EPBs disrupt GNSS signals, causing fluctuations that degrade communication and navigation in equatorial regions.

8. This study enriches the understanding of equatorial ionospheric dynamics and space weather in the East African sector.

9. The EPB occurrence varies daily, monthly, seasonally and is often more significant at EIA than at the equator due to favorable instability conditions, poleward expansion, and geomagnetic influences. The stronger EPBs at RCMN highlight the role of neutral winds, secondary instabilities, and seasonal variations in their growth. Understanding these dynamics is important for improving space weather predictions and mitigating communication disruptions systems.

Chapter 6

Assessment of Total Electron Content Responses to Equatorial Plasma Bubbles

6.1 Introduction

EPBs are regions of reduced electron density in the post-sunset equatorial and low-latitude ionosphere, typically surrounded by areas of enhanced electron density. This contrast gives rise to ionospheric electron density irregularities with scale sizes ranging from a few meters to several thousand kilometers (Lühr et al., 2014; Xiong et al., 2016).

Intermediate scale irregularities play a significant role in affecting very high-frequency (VHF) radio wave propagation, while small-scale irregularities are primarily responsible for disturbances in L-band transmissions. Understanding the characteristics of these irregularity scales is of particular importance, as they can significantly disrupt satellite-based communication and navigation systems, causing signal degradation or even complete loss of lock (Kintner et al., 2007; Pi et al., 1997; Spatz et al., 1988). EPB related plasma depletions and irregularities typically occur during nighttime, most often forming shortly after sunset and sometimes persisting for several hours past midnight (Vankadara et al., 2023). The general morphology of EPBs including their initiation mechanisms, evolution, spatial structure, and global distribution has been extensively studied using both ground and satellite based observations. Analyses of these observations indicate that EPBs are frequently triggered in the post-sunset period by the PRE of the zonal electric field, which rapidly lifts plasma to higher altitudes, creating a steep density gradient in the bottomside F-layer that favors instability growth. The EPB is plasma depleted region of the ionosphere which impact the trans-ionospheric communication and navigation system (Kumar and Chen, 2016). After sunset, E-region conductivity decreases, which enhances the eastward electric field, strengthening the PRE, that can generate suddenly vertical plasma density gradient toward the F-region of ionosphere (Kelley, 2009).

The EIA is a large-scale ionospheric feature characterized by a trough in electron density over the magnetic equator, flanked by two crests of enhanced electron density located approximately ±20° geomagnetic latitude north and south of the equator. This distinctive morphology arises primarily from the equatorial fountain effect, a process driven by $E \times B$ plasma drifts. During daytime, the eastward electric field in the equatorial ionosphere interacts with the Earth's geomagnetic field, producing an upward $E \times B$ drift of ionospheric plasma in the F-region. Once lifted to higher altitudes, plasma moves along geomagnetic field lines under the influence of gravity and pressure gradients, descending to lower latitudes in both hemispheres. This transport results in plasma accumulation at the anomaly crests and a corresponding electron density depletion over the equator (Appleton, 1946; Hanson and Moffett, 1966). The EIA is strongly influenced by solar EUV radiation, geomagnetic activity, and seasonal and longitudinal variations. It typically develops after sunrise, reaches its maximum intensity in the afternoon, and weakens toward sunset. Enhanced EIA development is often associated with increased PRE of the zonal electric field after sunset, which can precondition the ionosphere for the occurrence of equatorial plasma bubbles (Balan and Bailey, 1995).

EIA variability has significant implications for radio wave propagation, GNSS positioning accuracy, and space weather impacts over equatorial and low-latitude regions. Strong anomalies can increase the background ionospheric gradients, thereby modulating the growth rate and intensity of post-sunset ionospheric irregularities.

The plasma density gradient combines with the PRE of the zonal electric field, drives vertical $E \times B$ plasma drift. Their formation is most commonly explained by the RTI, which arises when a denser fluid overlays a lighter one. When disturbances occur at the interface between these layers, the instability grows, eventually leading to the development of EPBs (Haerendel and Eccles, 1992). A thorough understanding of EPBs is crucial, as these irregularities can disrupt radio wave propagation and degrade signals used in telecommunications and GNSS.

Pezzopane et al. (2021) highlighted that the GNSS loss of lock events is strongly correlated with well-defined values of both RODI and rate change of ROTI, suggesting their origin in the regions with high electron density gradients. Recent studies on EPB occurrence increasingly focus on analyses using GNSS-derived TEC depletions and the ROTI, owing to the direct relationship between ROTI, irregularity strength, and scintillation indices (Li et al., 2020b). Zakharenkova and Cherniak (2021) demonstrated a strong correlation between ROTI-derived phase fluctuation intensity and the degradation of precise GPS positioning under extreme EPB conditions. Similarly, Astafyeva et al. (2022) examined global ROTI maps in conjunction with other ground and space-based observations during a geomagnetic storm, providing a comprehensive multi-instrumental overview of ionospheric TEC and electron density irregularities.

One of the key advantages of ROTI-based studies is the extensive global coverage made possible by the dense network of conventional geodetic GNSS receivers, surpassing the spatial reach of most other ground-based monitoring systems (Qiang et al., 2021; Vital et al., 2025). This widespread availability of ROTI and TEC depletion data enables detailed investigations into the long-term global morphology and variability of EPBs.

Despite extensive studies on EPBs, there remains a lack of consensus on the optimal temporal window size for effectively capturing EPB signatures and accurately probing the response of TEC to these irregularities. This paper aims to address the equatorial ionospheric responses to several plasma bubbles events distributed along the period from 2013 to 2016 over the East African region and identifying the most suitable time window for EPB detection and characterizing the corresponding TEC dynamics.

6.2 Result and discussion

The Fig 6.1, 6.2 and 6.3 presents a comparative analysis of EPB events observed on three quiet days March 10, March 13, and March 31, 2013 using GPS-based ionospheric measurements from the ADIS, MOIU and MBAR stations respectively. Each row corresponds to one of the selected dates, and the columns display (from left to right) the sTEC variation, the ROTI, and the dSTEC (differential sTEC) derived using various smoothing window sizes.

In the first column, the sTEC plots show a clear post-sunset depletion trend, typically starting around 18:00 UT and lasting until about 22:00 UT, which is a signature of EPB occurrence. On March 10 and March 13, the depletion is deeper and more structured, while on March 31, the depletion appears shallower. The second column depicts the ROTI values, which indicate the level of ionospheric irregularities. All three days show elevated ROTI between 18:00 and 22:00 UT, line up well with the depletion periods seen in the sTEC plots. March 13 exhibits the most intense and high ROTI, suggesting highly irregular plasma behavior and the strongest EPB activity among the three days. March 31 also shows significant ROTI values, confirming moderate EPB development, while March 10 shows a more moderate and narrower irregularity region.

The third column compares dSTEC results using four different smoothing window sizes: 10, 30, 60, and 90 data points. These curves highlight how the smoothing window affects the clarity of depletion structures. The smallest window size is highly sensitive but noisy, making it difficult to distinguish true EPB features from random fluctuations. The second window size provides moderate smoothing but still exhibits noticeable noise. The third or 60 point window strikes the best balance it effectively suppresses noise while preserving the depth, structure, and timing of the depletions. The 90 point window size overly smooths the data, decrease important EPB features and making it less suitable for detailed characterization.

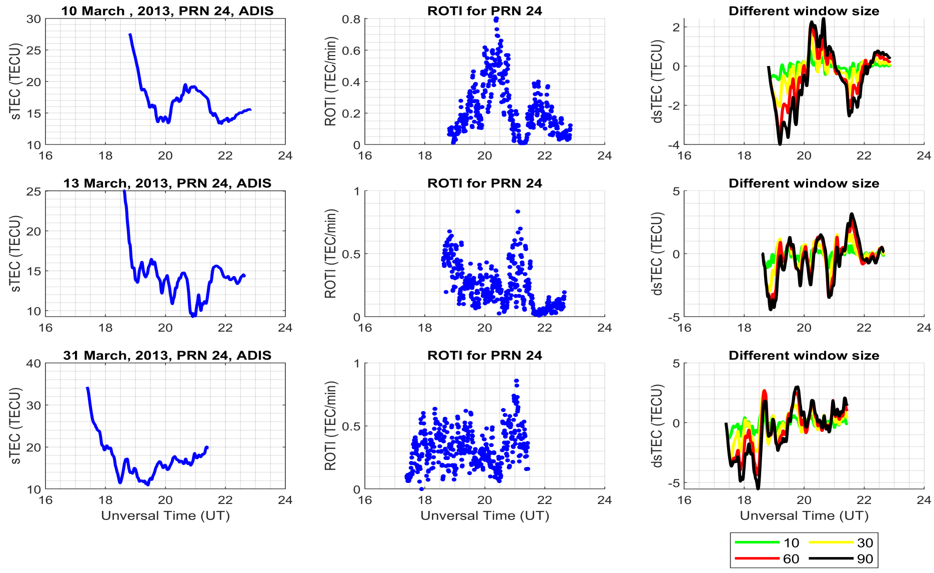

Figure 6.1: Variations in sTEC, ROTI, and filtered sTEC using different window sizes over ADIS station on 10, 13, and 31 March 2013 for PRN 24. The left column shows the raw sTEC measurements from 16:00 to 24:00 UT. The middle column displays the ROTI, highlighting ionospheric irregularities and potential EPB occurrences during the post-sunset period. The right column presents the dTEC variations obtained using different moving average window sizes (10, 30, 60, and 90 minutes), showing how window selection affects detection of fine scale TEC fluctuations. Higher ROTI values correspond with steeper gradients in dTEC, indicating the presence of plasma irregularities.

In general, the figure demonstrates the effectiveness of combining sTEC, ROTI, and dSTEC analyses for identifying and characterizing EPBs. It also shows that a 60-point smoothing window is optimal for highlighting EPB-induced depletions with sufficient clarity while minimizing noise. This comprehensive visualization reinforces the importance of selecting appropriate filtering parameters when analyzing TEC-based ionospheric disturbances.

Table 6.1: Comparison of smoothing window sizes for dSTEC analysis in detecting EPB. The table evaluates each window's sensitivity, noise level, and ability to preserve EPB structure. A 60-point window provides the best balance, offering clear depletion features with minimal noise, while smaller windows are overly sensitive and larger ones over-smooth the signal.

Window size	Sensitivity	Noise level	EPB	Verdict
10	High	Very high	poor (Noise)	Too sensitive
30	Moderate	Moderate	Fair	Jagged
60	Optimal	Low	Clear and accurate	Best
90	Low	Very low	Too smooth	Indistinct

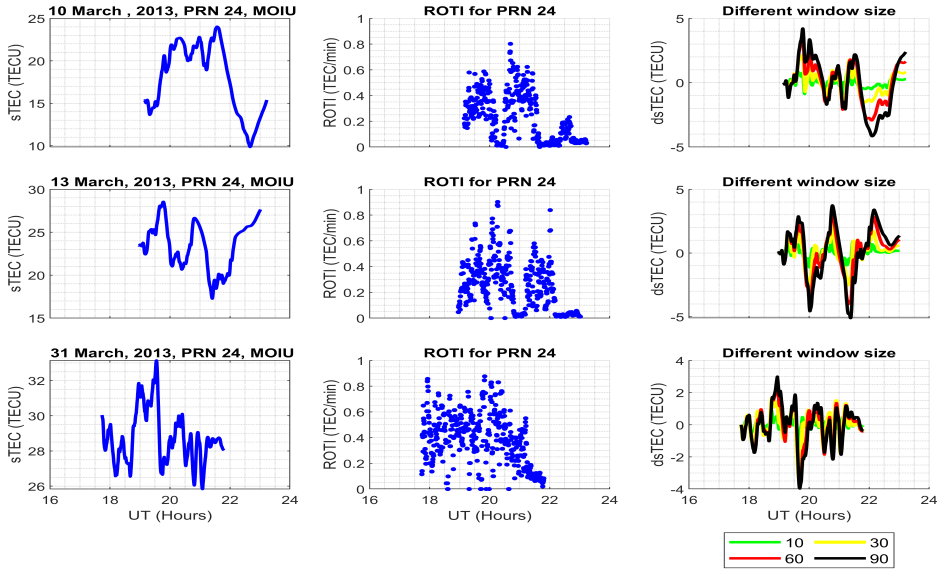

Figure 6.2: Variations in sTEC, ROTI, and filtered sTEC using different window sizes over MOIU station on 10, 13, and 31 March 2013 for PRN 24. The left column shows the raw sTEC measurements from 16:00 to 24:00 UT. The middle column displays the ROTI, highlighting ionospheric irregularities and potential EPB occurrences during the post-sunset period. The right column presents the dTEC variations obtained using different moving average window sizes (10, 30, 60, and 90 minutes), showing how window selection affects detection of fine scale TEC fluctuations. Higher ROTI values correspond with steeper gradients in dTEC, indicating the presence of plasma irregularities.

6.2.1 Seasonal Variations of Ionospheric Irregularities

The ROTI, which quantifies the rapid fluctuations in TEC, is a well-established proxy for characterizing ionospheric irregularities and the presence of EPBs (Pi et al., 1997). The seasonal and diurnal behavior of ROTI was investigated using GPS-derived ROTI data from multiple East African GNSS stations ADIS, RCMN, MOIU, and MBAR for the years 2014 and 2015. From Figure 6.4,6.5 and 6.6 each dataset is analyzed seasonally across the March equinox, June solstice, September equinox, and December solstice. During the March equinox, ROTI values reached their highest values across all stations and both years.

In 2014, ROTI values peaked at around 4.5-5.0 $TECU/min$ at RCMN and MBAR, especially between 18:00 and 22:00 UT, indicating intense post-sunset ionospheric irregularities. MOIU and ADIS also showed elevated activity in this time window, although slightly lower in amplitude, with maximum ROTI values ranging between 3.5 and 4.5 $TECU/min$. The 2015 March equinox mirrored this trend, particularly at MBAR and MOIU, where ROTI values again exceeded 4.5 $TECU/min$, confirming the consistent and repeatable nature of EPB activity during this season.

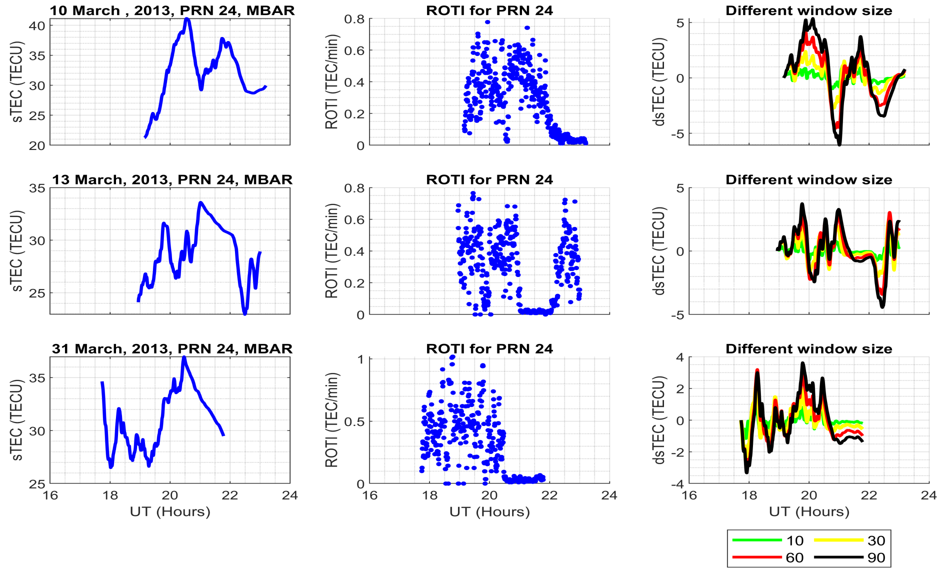

Figure 6.3: Variations in sTEC, ROTI, and filtered sTEC using different window sizes over MBAR station on 10, 13, and 31 March 2013 for PRN 24. The left column shows the raw sTEC measurements from 16:00 to 24:00 UT. The middle column displays the ROTI, highlighting ionospheric irregularities and potential EPB occurrences during the post-sunset period. The right column presents the dTEC variations obtained using different moving average window sizes (10, 30, 60, and 90 minutes), showing how window selection affects detection of fine scale TEC fluctuations. Higher ROTI values correspond with steeper gradients in dTEC, indicating the presence of plasma irregularities.

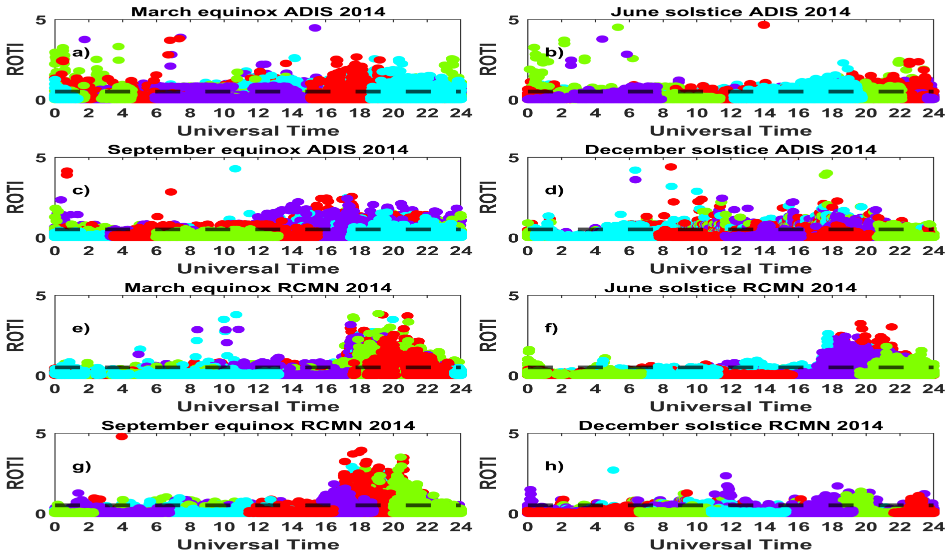

Figure 6.4: Seasonal variation ROTI as an indicator of ionospheric irregularity intensity over ADIS and RCMN in 2014. This figure presents the seasonal distribution of ROTI values, serving as a reliable proxy for detecting and assessing ionospheric irregularities in the equatorial region.

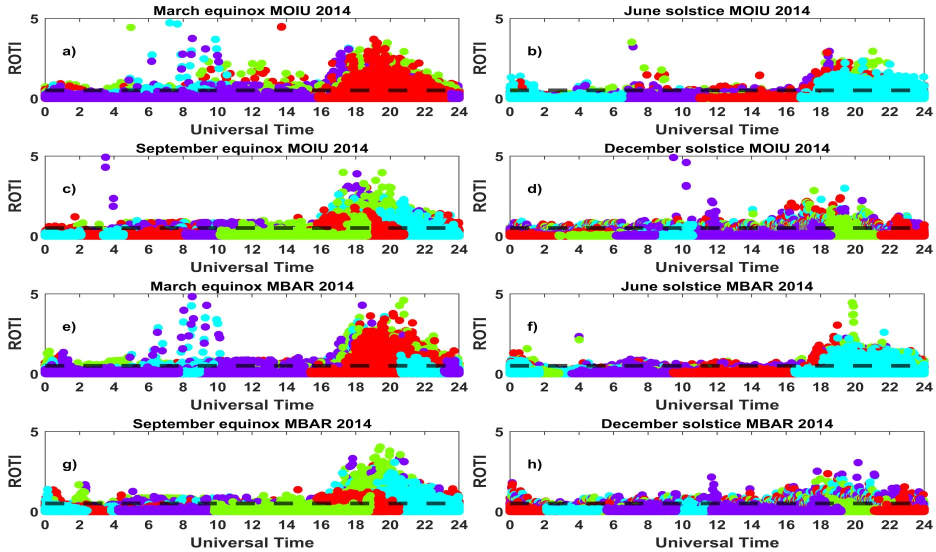

Figure 6.5: Seasonal variation ROTI as an indicator of ionospheric irregularity intensity over MOIU and MBAR in 2014. This figure presents the seasonal distribution of ROTI values, serving as a reliable proxy for detecting and assessing ionospheric irregularities in the equatorial region.

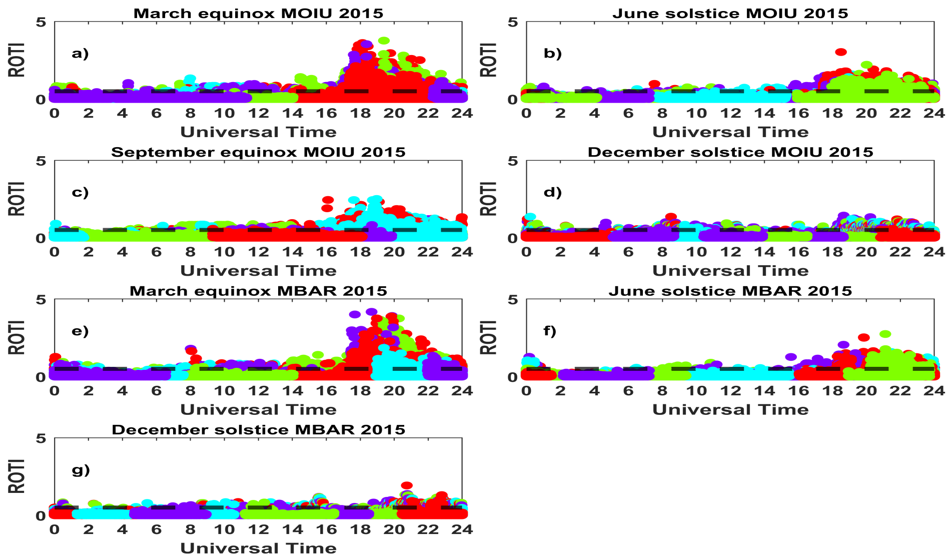

Figure 6.6: Seasonal variation ROTI as an indicator of ionospheric irregularity intensity over MOIU and MBAR in 2015. This figure presents the seasonal distribution of ROTI values, serving as a reliable proxy for detecting and assessing ionospheric irregularities in the equatorial region.

This strong post-sunset enhancement in ROTI is a well-known equatorial feature, driven by the PRE of the eastward electric field, which lifts the F-region and triggers Rayleigh-Taylor instabilities (Abdu, 2001; Sultan, 1996). The June solstice revealed significantly weaker ROTI activity. Across all stations and both years, post-sunset

Table 6.2: Seasonal maximum ROTI values in TECU/min and corresponding time intervals (UT) recorded at four East African GNSS stations (ADIS, RCMN, MOIU, and MBAR) during 2014 and 2015. The ROTI values predict the intensity of ionospheric irregularities, with higher values indicating the likely occurrence of EPBs. The table shows a clear seasonal pattern, with significantly increasing ROTI values during the equinoxes and notably weaker activity during the solstices periods, particularly in the post-sunset hours.

Year	station	Season	Max ROTI (TECU/min)	Time (UT)
2014	ADIS	March equinox	≈ 3.5	18:00-22:00
		June solstice	≈ 1.5	18:00-21:00
		September equinox	≈ 3.2	18:00-22:00
		December solstice	≈ 1.2	17:00-21:00
	RCMN	March equinox	≈ 4.8	18:00-22:00
		June solstice	≈ 2.0	18:00-21:00
		September equinox	≈ 4.5	18:00-22:00
		December solstice	≈ 1.3	18:00-21:00
	MOIU	March equinox	≈ 4.2	18:00-22:00
		June solstice	≈ 2.0	18:00-21:00
		September equinox	≈ 4.0	18:00-22:00
		December solstice	≈ 1.3	18:00-21:00
	MBAR	March equinox	≈ 5.0	17:00-22:00
		June solstice	≈ 1.8	18:00-21:00
		September equinox	≈ 4.3	18:00-22:00
		December solstice	≈ 1.2	18:00-21:00
2015	MOIU	March equinox	≈ 4.7	18:00-22:00
		June solstice	≈ 1.5	18:00-21:00
		September equinox	≈ 3.8	18:00-22:00
		December solstice	≈ 1.1	18:00-21:00
	MBAR	March equinox	≈ 5.0	17:00-22:00
		June solstice	≈ 1.7	18:00-21:00
		December solstice	≈ 1	18:00-21:00

ROTI values rarely exceeded 2.0 $TECU/min$, with most values remaining below 1.5 $TECU/min$. For instance, in 2014, the MBAR and MOIU stations displayed very weak irregularities with isolated post-sunset peaks around 1.8 $TECU/min$, while ADIS and RCMN showed negligible fluctuations. Similarly, the 2015 data showed almost flat ROTI curves, indicating a quiet ionospheric environment. The reduced vertical plasma drift and weaker E-region conductivity during solstices contribute to the suppression of EPB development. The September equinox also demonstrated robust ionospheric irregularities, though slightly weaker than those in March. In 2014, MBAR and MOIU registered ROTI values reaching 4.0-4.5 $TECU/min$ between 18:00 and 22:00 UT, indicating active EPB development. RCMN and ADIS showed moderate activity, with maximum ROTI values near 3.5 $TECU/min$. The September equinox in 2015 similarly showed enhanced ROTI values at MOIU, with peaks exceeding 3.5 $TECU/min$, while MBAR had values around 4.0 $TECU/min$. This seasonal enhancement is consistent with previous studies showing that equinoxes present optimal conditions for EPB growth due to the near alignment of the solar terminator with the magnetic equator, which maximizes the zonal electric fields. The December solstice was characterized by the lowest ROTI values across all datasets. For both years and all stations, ROTI values remained mostly below 1.0 $TECU/min$, with occasional isolated spikes not exceeding 1.5 $TECU/min$. This suggests a stable and less disturbed ionosphere, with minimal post-sunset EPB activity. Notably, ADIS and MBAR showed the lowest overall disturbances during this period. The absence of significant irregularities can be explained by the diminished prereversal enhancement and unfavorable electrodynamic conditions in December.

6.2.2 Comparison of sTEC enhancements and associated EPB activity.

The provided figures 6.7 and 6.8 illustrate the temporal variation of TEC and the associated EPB depletion for multiple stations across the East African sector. The analysis covers the years 2013, 2014, 2015 and 2016 at stations ADIS, RCMN, MOIU, and MBAR. These figures shows the monthly and seasonal variation of sTEC and EPB occurrences over the East African sector for the years. The sTEC plots represent the ionospheric total electron content, while the EPB plots reflect the depletion strength or variability due to plasma bubbles, calculated likely from parameters such as ROTI or dsTEC. As we can observe from the contour plot maps the TEC are get maximum during the day time between 10 to 18 LT and the EPBs is occurred during 20-24 LT and 0 to 3 LT. The higher the daytime TEC, the more intense and widespread the post-sunset EPBs, because the gradient-driven instability is stronger as result. As we can observe from the contour maps EPBs can be classified based on their time of occurrence during the night, mainly into post-sunset EPBs and post-midnight EPBs. These EPBs typically occurrence shortly after sunset, usually between 20:00 and 24:00 in the equatorial and low-latitude regions. The Post-sunset EPBs are primarily triggered by the PRE of the vertical plasma drift in the F-region, which destabilizes the ionosphere through the Rayleigh-Taylor instability. It's characterized by, strong, large-scale plasma depletions,results in TEC reductions and high scintillation activity. Most of the time initiate near the magnetic equator and extend along the field lines toward higher latitudes. The seconde type is post-Midnight EPBs which develop after midnight, typically between 00:00 LT and 05:00 LT, and are less frequent than post-sunset bubbles. This type of EPBs are formed due to continued growth of pre-existing post-sunset bubbles, or due to localized ionospheric instabilities under low background plasma density.It's characterized by weaker and smaller in spatial extent compared to post-sunset EPBs and produce moderate TEC depletions and weaker scintillation effects. It Can still propagate along field lines but are often more irregular.

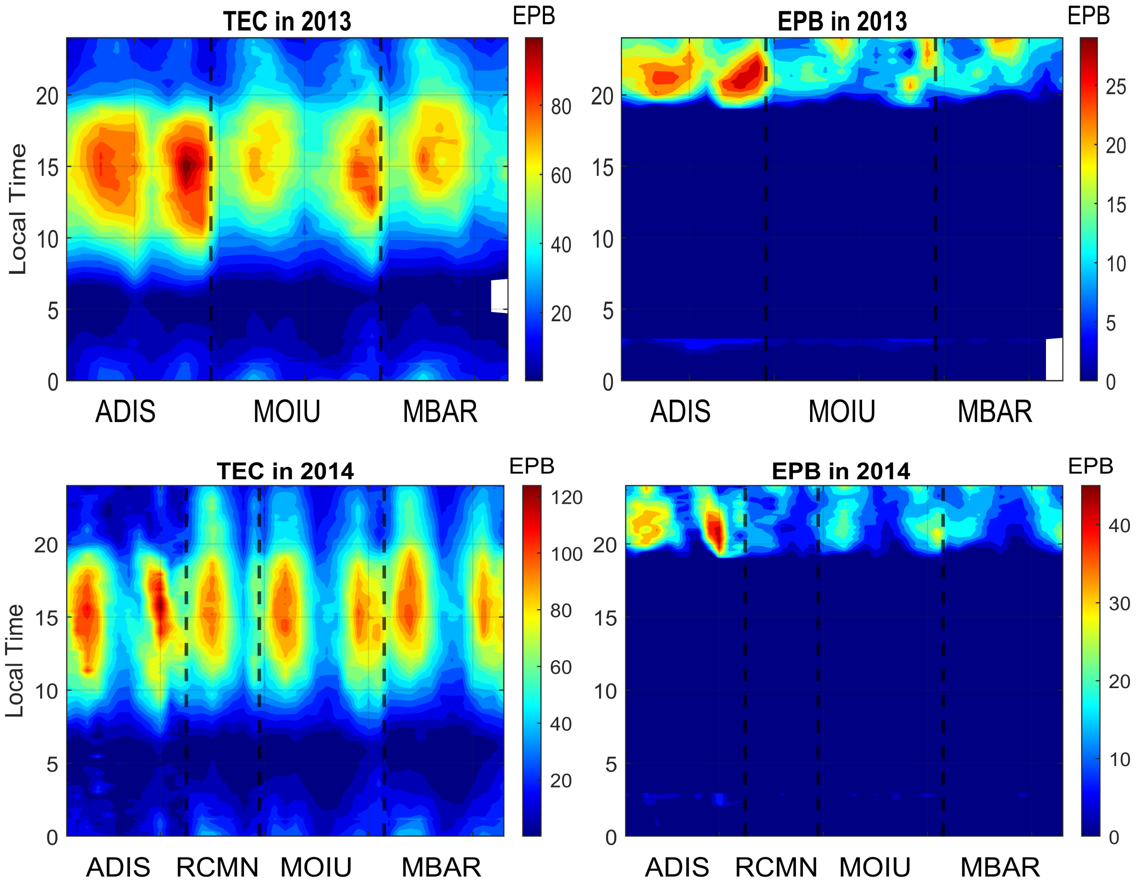

Figure 6.7: Variations of sTEC and EPB occurrence over ADIS, MOIU, and MBAR stations for 2013 and 2014 respectively.

The post-sunset behavior of the ionosphere over equatorial regions is characterized by significant variability in electron density, usually captured by the sTEC measured using GNSS signals. This enhancement in sTEC typically occurs between 18:00 and 21:00 UT due to the PRE of the eastward electric field, which lifts the F-region plasma to higher altitudes with reduced recombination rates, thereby increasing electron content (Fejer et al., 1991; Kelley, 2009) This elevated post-sunset ionization provides favorable conditions for the development of EPBs localized depletions in electron density that result from RTI in the bottomside F-layer (Woodman and La Hoz, 1976). EPBs typically initiate shortly after the peak of sTEC, often around 19:30 to 24:00 LT, indicating that a sufficient background ionospheric density is a prerequisite for EPB formation (Basu et al., 2001; Burke et al., 2004). The seasonal dependence of both sTEC and EPBs is also evident, with maximum activity during the equinoctial months, attributed to the alignment of the geomagnetic and solar terminators, which amplifies vertical plasma drift and instabilities. In contrast, solstice periods exhibit suppressed EPB activity despite moderate sTEC levels, likely due to weaker vertical drifts and altered thermospheric wind patterns (Sultan, 1996). Observations over East African stations confirm these patterns, highlighting that while sTEC peaks are necessary, they must be supported by dynamic electrodynamic drivers for EPB growth.

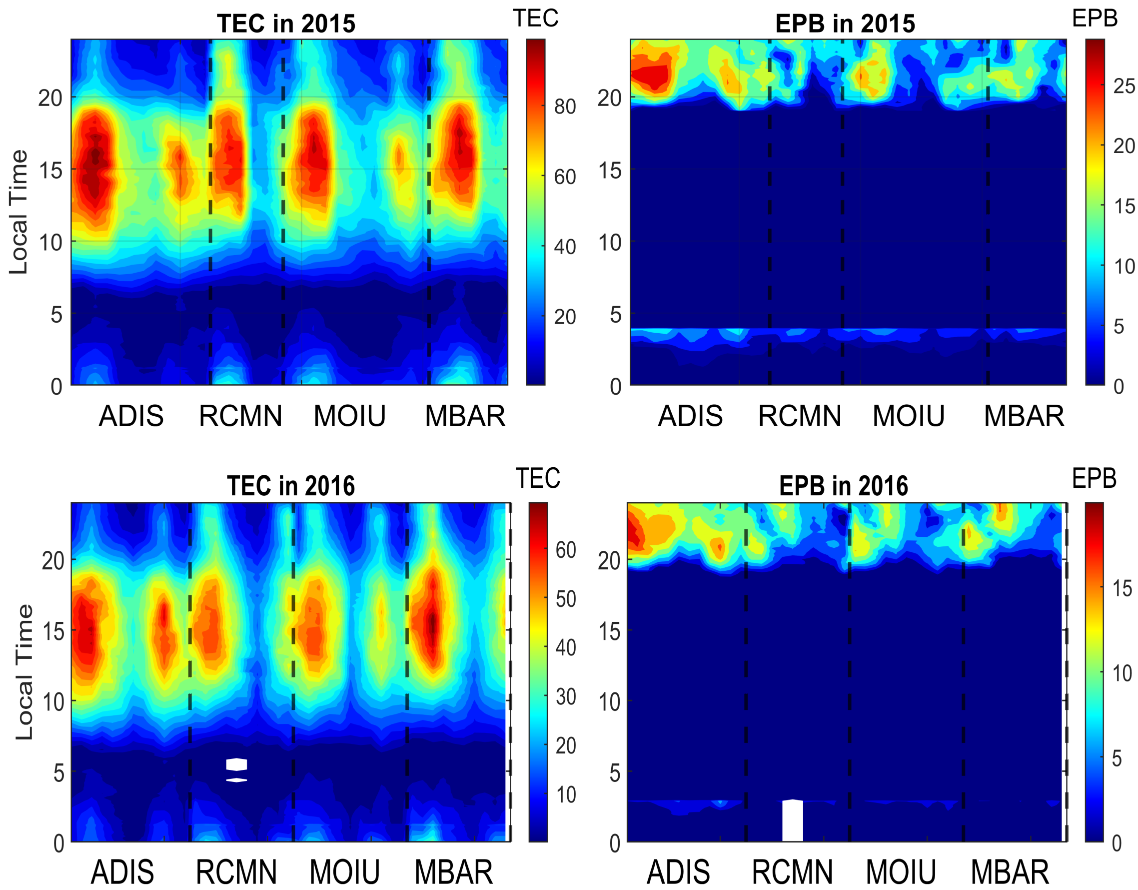

Figure 6.8: Variations of sTEC and EPB occurrence over ADIS, MOIU, and MBAR stations for 2015 and 2016 respectively.

This relationship underscores the critical role of post-sunset ionospheric conditions in space weather modeling and GNSS performance forecasting across equatorial regions. The comparison of TEC enhancements and associated EPB activity provides important insights into the coupling between ionospheric plasma density variations and the occurrence of post-sunset irregularities. TEC enhancements, often observed in the PRE period before local sunset, are indicative of increased ionization or plasma uplift in the equatorial ionosphere. These enhancements can create favorable conditions for the growth of RTI, which is the primary driver of EPB formation. Observations show that days with significant sTEC enhancement prior to sunset tend to exhibit higher EPB occurrence rates in the post-sunset hours. This is because a strong pre-sunset TEC increase is often associated with an intense PRE, driven by the eastward electric field and thermospheric wind dynamo. The PRE lifts the F-layer to higher altitudes, where the recombination rate is lower, and steepens the bottomside plasma density gradient. This enhanced gradient increases the growth rate of the generalized RTI (Sultan, 1996), allowing small perturbations in plasma density to grow rapidly into large-scale depletions that manifest as EPBs. Conversely, during geomagnetically quiet periods with weak pre-sunset sTEC enhancement, the bottomside density gradient remains small and the instability growth rate insufficient, resulting in suppressed EPB activity (Zakharenkova and Cherniak, 2021). This relationship, validated using GNSS-derived sTEC data and EPB occurrence statistics, provides a robust diagnostic framework for characterizing ionospheric irregularity climatology over equatorial and low-latitude regions, particularly in sectors such as East Africa where simultaneous multi-station observations enable high-resolution spatial mapping of both sTEC and EPB distributions.

Analysis of the 2013-2016 dataset shows that EPBs are closely associated with distinct variations in the TEC. During EPB events, TEC exhibits sharp post-sunset reductions corresponding to regions of depleted plasma density along the satellite line-of-sight. The depletion depth and duration of these TEC depletions vary with the intensity and spatial extent of the EPBs, with enhanced bubbles causing more pronounced drops in TEC. Across all four stations (ADIS, RCMN, MOIU, and MBAR), post-sunset TEC dips consistently coincide with periods of elevated EPB activity, as quantified by the EPB depletion depth and occurrence rate. This indicates that TEC measurements can serve as a reliable proxy for detecting and characterizing EPBs. Seasonal and annual variations further reveal that TEC depletion patterns reflect the temporal evolution of EPBs, highlighting the importance of TEC monitoring for understanding ionospheric irregularities in the East African sector.

6.3 Summary

This study provides a comprehensive assessment of Equatorial Plasma Bubbles (EPBs) and their impact on the ionospheric Total Electron Content (TEC) over low-latitude East African stations during geomagnetically quiet periods of the 24th solar cycle. Using GNSS-derived TEC measurements and the Rate of TEC Index (ROTI) with an optimized window size, we successfully identified characteristic depletion signatures indicative of EPBs. The analysis reveals that post-sunset TEC depletions consistently occur between 17:00 UT and 00:02 UT, confirming the presence of EPB activity across all four stations (ADIS, RCMN, MOIU, and MBAR).

The magnitude and duration of TEC depletions were found to vary with the intensity and spatial extent of the plasma bubbles, with stronger or larger EPBs producing more pronounced reductions in TEC. Across all stations, these post-sunset TEC dips reliably coincide with periods of elevated EPB activity, as quantified by both depletion depth and occurrence rate. This strong correlation indicates that TEC and its derived indices, such as ROTI, serve as effective proxies for detecting, characterizing, and monitoring EPBs in low-latitude regions.

Furthermore, the results highlight the temporal and spatial consistency of EPB occurrences over the East African sector, emphasizing the importance of continuous GNSS monitoring for understanding ionospheric irregularities. These findings have significant implications for predicting the impact of EPBs on trans-ionospheric radio communications and navigation systems, particularly in equatorial and low-latitude regions where scintillation effects are most pronounced.

Overall, this study reinforces the utility of TEC-based techniques for investigating EPB dynamics, providing valuable insights into their seasonal and interannual behavior, and supporting the development of reliable mitigation strategies for space weather effects on communication and navigation systems.

Chapter 7

Conclusions and suggestions for further research

7.1 Conclusion

This dissertation provided a comprehensive analysis of the spatial and temporal characteristics of Total Electron Content (TEC) and Equatorial Plasma Bubbles (EPBs) over the East African region using an extensive multi-year GNSS dataset spanning from 2012 to 2016. The study successfully demonstrated that the ionosphere over East Africa exhibits distinct diurnal, seasonal, and latitudinal behaviors that are consistent across multiple observation years. TEC values were found to peak around local noon, reflecting the strong influence of solar radiation on ionospheric electron density, and to reach their maximum during the equinoxes when geomagnetic and solar conditions favor enhanced ionospheric activity. Notably, significant TEC gradients were observed between the northern and southern regions of Ethiopia, highlighting the sensitivity of the equatorial ionosphere to small-scale spatial variations driven by its proximity to the magnetic equator.

The stability of TEC patterns across different stations and years underscores the robustness of the regional ionospheric dynamics. This consistency also validates the application of Ordinary Kriging as a reliable and effective spatial interpolation method for modeling TEC over East Africa. The technique demonstrated excellent performance, achieving an average correlation of approximately 95° with GPS-derived TEC measurements. Such a high level of agreement confirms that Kriging not only captures the broad spatial structure of the ionosphere but also preserves fine-scale features essential for both scientific research and practical applications in navigation and communication systems.

In addition to TEC variability, the study provided valuable insights into the occurrence and behavior of EPBs. EPBs were frequently observed between 17:00 and 03:00 UT, consistent with post-sunset ionospheric processes that drive plasma instability. Their highest intensity during equinoctial months aligns with established global EPB patterns, reinforcing the role of solar terminator effects and geomagnetic alignment in facilitating irregularity growth. The research highlighted the influence of multiple geophysical drivers including geomagnetic activity, neutral winds, geographic and geomagnetic positioning, and seasonal factors on EPB development. Although EPBs typically originate near the magnetic equator, the study showed that they can extend into the East African equatorial ionization anomaly region due to poleward neutral winds, uplifted plasma, and secondary instabilities, leading to significant impacts on GNSS signal propagation.

Furthermore, the effectiveness of detrended sTEC, ROTI, and the geomagnetic indices Dst and Kp as diagnostic tools for detecting and characterizing EPBs was clearly demonstrated. These indices proved capable of capturing both the onset and intensity of ionospheric irregularities, making them valuable for real-time monitoring and long-term studies of space weather phenomena. Their combined use enhances the capacity to understand ionospheric disturbances, forecast EPB occurrence, and support the mitigation of their adverse effects on satellite based navigation, communication, and remote-sensing systems in the region.

Overall, this research contributes significantly to the understanding of ionospheric behavior over the East African equatorial sector. The findings strengthen the scientific basis for improved space weather modeling and forecasting, support the development of resilient GNSS-based applications, and provide essential insights for future research aimed at enhancing regional ionospheric monitoring. By demonstrating the value of multi-year GNSS observations and advanced spatial interpolation techniques, this dissertation helps lay the groundwork for more accurate and reliable ionospheric studies in East Africa and comparable equatorial environments.

7.2 Further research

Based on the findings of this study, several approaches for future research are recommended to enhance the understanding of Total Electron Content (TEC) distribution and the occurrence of Equatorial Plasma Bubbles (EPBs) using advanced modeling techniques:

1. **Expansion of Kriging-Based TEC Modeling Across Solar Cycles and Geomagnetic Conditions**. The Kriging interpolation technique applied in this study has demonstrated strong performance in estimating GPS-derived TEC values, showing a positive correlation with observational data over the equatorial region. To enhance the robustness and applicability of this approach, it is recommended that the same Kriging methodology be extended to cover. An entire solar cycle to analyze long-term ionospheric behavior. Geomagnetically disturbed periods to evaluate the models performance under space weather events. This expansion will provide a more comprehensive understanding of ionospheric variability and improve prediction accuracy during both quiet and disturbed conditions.

2. **Application of Kriging to Global TEC Modeling Using Multi-Source Data**. While this study focused on regional TEC estimation, the Kriging method has the potential to be scaled globally. Future research could explore integrating diverse data sourcessuch as satellite-based TEC observations (e.g., COSMIC, SWARM), ground-based GPS networks, and ionosonde measurementsto create high-resolution global ionospheric TEC maps. This multi-source fusion approach can enhance the spatial and temporal resolution of global TEC models, making them more suitable for real-time ionospheric monitoring and forecasting applications.

3. **Comparative Analysis with Other Ionospheric Modeling Techniques**. A more detailed comparative study is recommended to assess the strengths and limitations of each method under various geophysical conditions. This comparison could provide valuable insights into selecting optimal modeling techniques for specific applications, such as satellite navigation, communication, and space weather prediction.

4. **Detailed Investigation of Equatorial Plasma Bubble (EPB) Occurrence and Dynamics**. The study also examined the formation and spatial distribution of EPBs over the equatorial region. Observations indicate that EPBs, which originate near the magnetic equator, can migrate along geomagnetic field lines and influence regions such as the East African Low-Latitude Anomaly

(ELA). Future research should:

- Utilize a larger and more comprehensive dataset, including multi-year GNSS observations, to analyze EPB occurrence patterns more precisely.
- Develop models that can predict the onset, propagation, and spatial extent of EPBs in relation to local time, season, solar activity, and geomagnetic disturbances.
- Specifically focus on modeling EPBs over the East African region, which remains under-studied despite its geophysical significance and socio-economic reliance on space-based technologies.

5. **Integration with Real-Time Ionospheric Monitoring Systems**. As modeling techniques like Kriging and machine learning-based models continue to evolve, their integration with real-time data assimilation systems should be explored. Such systems would be invaluable for supporting applications in navigation, aviation, and satellite operations that are sensitive to ionospheric disturbances.

By pursuing these recommendations, future research can significantly advance our understanding of ionospheric behavior in equatorial and global contexts, while also contributing to the development of practical tools for mitigating the effects of ionospheric irregularities on technological systems.

References

Aarons, J. (1997). Global positioning system phase fluctuations at auroral latitudes. *Journal of Geophysical Research: Space Physics*, 102(A8):17219–17231.

Abdu, M. (2001). Outstanding problems in the equatorial ionosphere–thermosphere electrodynamics relevant to spread f. *Journal of Atmospheric and Solar-Terrestrial Physics*, 63(9):869–884.

Abdu, M. (2005). Equatorial ionosphere–thermosphere system: Electrodynamics and irregularities. *Advances in Space Research*, 35(5):771–787.

Abe, O., Rabiu, A., Bolaji, O., and Oyeyemi, E. (2018). Modeling african equatorial ionosphere using ordinary kriging interpolation technique for gnss applications. *Astrophysics and Space Science*, 363(8):168.

Abiriga, F., Amabayo, E. B., Jurua, E., and Cilliers, P. J. (2020). Statistical characterization of equatorial plasma bubbles over east africa. *Journal of Atmospheric and Solar-Terrestrial Physics*, 200:105197.

Acharya, R. and Majumdar, S. (2019). Statistical relation of scintillation index s4 with ionospheric irregularity index roti over indian equatorial region. *Advances in space Research*, 64(5):1019–1033.

Ali, M., Goovaerts, P., Nazia, N., Haq, M. Z., Yunus, M., and Emch, M. (2006). Application of poisson kriging to the mapping of cholera and dysentery incidence in an endemic area of bangladesh. *International journal of health geographics*, 5:1–11.

Amabayo, E. B., Andima, G., and Ssenyunzi, R. C. (2021). Instantaneous ionospheric scintillation mapping over the east african region by use of gps derived amplitude scintillation proxy. *Asian J Res Rev Phys*, 4(2):6–20.

Anderson, D. (1973). A theoretical study of the ionospheric f region equatorial anomalyii. results in the american and asian sectors. *Planetary and Space Science*, 21(3):421–442.

Appleton, E. V. (1946). Two anomalies in the ionosphere. *Nature*, 157(3995):691–691.

Astafyeva, E., Yasyukevich, Y. V., Maletckii, B., Oinats, A., Vesnin, A., Yasyukevich, A., Syrovatskii, S., and Guendouz, N. (2022). Ionospheric disturbances and irregularities during the 25–26 august 2018 geomagnetic storm. *Journal of Geophysical Research: Space Physics*, 127(1):e2021JA029843.

Babu Sree Harsha, P., Venkata Ratnam, D., Lavanya Nagasri, M., Sridhar, M., and Padma Raju, K. (2020). Kriging-based ionospheric tec, roti and amplitude scintillation index (s 4) maps for india. *IET Radar, Sonar & Navigation*, 14(11):1827–1836.

Balan, N. and Bailey, G. (1995). Equatorial plasma fountain and its effects: Possibility of an additional layer. *Journal of Geophysical Research: Space Physics*, 100(A11):21421–21432.

Balan, N., Liu, L., and Le, H. (2018). A brief review of equatorial ionization anomaly and ionospheric irregularities. *Earth and Planetary Physics*, 2(4):257–275.

Basu, S., Basu, S., Groves, K., Yeh, H.-C., Su, S.-Y., Rich, F., Sultan, P., and Keskinen, M. (2001). Response of the equatorial ionosphere in the south atlantic region to the great magnetic storm of july 15, 2000. *Geophysical Research Letters*, 28(18):3577–3580.

Basu, S., Groves, K., Basu, S., and Sultan, P. (2002). Specification and forecasting of scintillations in communication/navigation links: current status and future plans. *Journal of atmospheric and solar-terrestrial physics*, 64(16):1745–1754.

Basu, S., Groves, K., Quinn, J., and Doherty, P. (1999). A comparison of tec fluctuations and scintillations at ascension island. *Journal of Atmospheric and Solar-Terrestrial Physics*, 61(16):1219–1226.

Baumjohann, W. and Treumann, R. A. (2012). *Basic space plasma physics*. World Scientific.

Bhattacharyya, A. (2022). Equatorial plasma bubbles: A review. *Atmosphere*, 13(10):1637.

Biswas, A. and Si, B. C. (2013). Model averaging for semivariogram model parameters. *Advances in agrophysical research*, 4:81–96.

Blanch, J. and Walter, T. (2002). Application of spatial statistics to ionosphere estimation for waas. In *Proceedings of the 2002 National Technical Meeting of The Institute of Navigation*, pages 719–724.

Brekke, A. (1998). Physics of the upper polar atmosphere. *Atmospheric Environment*, 32(2):262–262.

Brekke, A. (2012). *Physics of the upper polar atmosphere*. Springer Science & Business Media.

Burke, W., Gentile, L., Huang, C., Valladares, C., and Su, S. (2004). Longitudinal variability of equatorial plasma bubbles observed by dmsp and rocsat-1. *Journal of Geophysical Research: Space Physics*, 109(A12).

Cameron, K. and Hunter, P. (2002). Using spatial models and kriging techniques to optimize long-term ground-water monitoring networks: a case study. *Environmetrics: The official journal of the International Environmetrics Society*, 13(5-6):629–656.

Campbell, W. H. (2003). *Introduction to geomagnetic fields*. Cambridge University Press.

Carmo, C., Denardini, C., Figueiredo, C. A. O., Resende, L. C. A., Picanço, G. A. d. S., Neto, P. B., Nogueira, P. A. B., Moro, J., and Chen, S. S. (2021). Evaluation of different methods for calculating the roti index over the brazilian sector. *Radio Science*, 56(8):1–12.

Carrano, C. S., Groves, K. M., and Rino, C. L. (2019). On the relationship between the rate of change of total electron content index (roti), irregularity strength (ckl), and the scintillation index (s4). *Journal of Geophysical Research: Space Physics*, 124(3):2099–2112.

Carrasco, P. (2010). Nugget effect, artificial or natural? *Journal of the Southern African Institute of Mining and Metallurgy*, 110(6):299–305.

Cele, G., Andima, G., Habyarimana, V., and Jurua, E. (2023). Mapping of the ionospheric total electron content over the east african low–latitude region. *Advances in Space Research*, 71(10):4410–4423.

Chapman, S. (1931). The absorption and dissociative or ionizing effect of monochromatic radiation in an atmosphere on a rotating earth. *Proceedings of the Physical Society*, 43(1):26.

Chen, W., Gao, S., Hu, C., Chen, Y., and Ding, X. (2008). Effects of ionospheric disturbances on gps observation in low latitude area. *Gps Solutions*, 12:33–41.

Choi, B.-K. and Kil, H. (2017). Large ionospheric tec depletion induced by the 2016 north korea rocket. *Advances in Space Research*, 59(2):532–541.

Christensen, A., Paxton, L., Avery, S., Craven, J., Crowley, G., Humm, D., Kil, H., Meier, R., Meng, C.-I., Morrison, D., et al. (2003). Initial observations with the global ultraviolet imager (guvi) in the nasa timed satellite mission. *Journal of Geophysical Research: Space Physics*, 108(A12).

Cosentino, N., Opazo, N., Lambert, F., Osses, A., and van't Wout, E. (2023). Globalkrigger: A global kriging interpolation toolbox with paleoclimatology examples. *Geochemistry, Geophysics, Geosystems*, 24(6):e2022GC010821.

Coster, A. and Komjathy, A. (2008). Space weather and the global positioning system. *Space Weather*, 6(6).

Cressie, N. (2015). *Statistics for spatial data.* John Wiley & Sons.

Datta-Barua, S. and Bust, G. S. (2011). Gnss imaging-derived dynamics of ionospheric storm transition regions. In *Proceedings of the 24th International Technical Meeting of The Satellite Division of the Institute of Navigation (ION GNSS 2011)*, pages 2532–2541.

Davies, K. (1990). Ionospheric radio, number 31.

Davies, K. and Hartmann, G. (1997). Studying the ionosphere with the global positioning system. *Radio Science*, 32(4):1695–1703.

Deutsch, C. V., Journel, A. G., et al. (1992). Geostatistical software library and users guide. *New York*, 119(147):578.

Dieminger, W., Hartmann, G. K., and Leitinger, R. (2012). *The upper atmosphere: data analysis and interpretation.* Springer Science & Business Media.

D'ujanga, F. M., Opio, P., and Twinomugisha, F. (2016). Variation of the total electron content with solar activity during the ascending phase of solar cycle 24 observed at makerere university, kampala. *Ionospheric space weather: longitude and hemispheric dependences and lower atmosphere forcing*, pages 145–154.

Farley, D., Bonelli, E., Fejer, B. G., and Larsen, M. (1986). The prereversal enhancement of the zonal electric field in the equatorial ionosphere. *Journal of Geophysical Research: Space Physics*, 91(A12):13723–13728.

Fejer, B. (1991). Low latitude electrodynamic plasma drifts: A review. *Journal of Atmospheric and Terrestrial Physics*, 53(8):677–693.

Fejer, B. G., De Paula, E., Gonzalez, S., and Woodman, R. (1991). Average vertical and zonal f region plasma drifts over jicamarca. *Journal of Geophysical Research: Space Physics*, 96(A8):13901–13906.

Fejer, B. G., Scherliess, L., and De Paula, E. (1999). Effects of the vertical plasma drift velocity on the generation and evolution of equatorial spread f. *Journal of Geophysical Research: Space Physics*, 104(A9):19859–19869.

Fitzpatrick, R. (2022). *Plasma physics: an introduction*. Crc Press.

Garcia, F., Kelley, M., Makela, J., and Huang, C.-S. (2000). Airglow observations of mesoscale low-velocity traveling ionospheric disturbances at midlatitudes. *Journal of Geophysical Research: Space Physics*, 105(A8):18407–18415.

Gentile, L., Burke, W., and Rich, F. (2006). A climatology of equatorial plasma bubbles from dmsp 1989–2004. *Radio Science*, 41(05):1–7.

Getahun, G. B., Melessew, N., and Ambelu, T. (2022). Comparative assessment of the performances of gps-tec assisted ntcm, nequick2 and neural network models to describe the east-african equatorial ionosphere. *Authorea Preprints*.

Giday, N. M., Katamzi-Joseph, Z. T., and Stoneback, R. (2020). Effect of moderate geomagnetic storms on equatorial plasma bubbles over eastern africa in the year 2012: Evolution and electrodynamics. *Advances in Space Research*, 65(7):1701–1713.

Gombosi, T. I. (1998). *Physics of the space environment*. Cambridge University Press.

Gonzalez, W., Joselyn, J.-A., Kamide, Y., Kroehl, H. W., Rostoker, G., Tsurutani, B. T., and Vasyliunas, V. (1994). What is a geomagnetic storm? *Journal of Geophysical Research: Space Physics*, 99(A4):5771–5792.

Groves, K., Basu, S., Quinn, J., Pedersen, T., Falinski, K., Brown, A., Silva, R., and Ning, P. (2000). A comparison of gps performance in a scintillation environment at ascension island. In *Proceedings of the 13th International Technical Meeting of the Satellite Division of The Institute of Navigation (ION GPS 2000)*, pages 672–679.

Grynyshyna-Poliuga, O., Stanislawska, I., and Swiatek, A. (2014). Regional ionosphere mapping with kriging and b-spline methods. In *Mitigation of Ionospheric Threats to GNSS: an Appraisal of the Scientific and Technological Outputs of the TRANSMIT Project*. IntechOpen.

Haerendel, G. and Eccles, J. (1992). The role of the equatorial electrojet in the evening ionosphere. *Journal of Geophysical Research: Space Physics*, 97(A2):1181–1192.

Haerendel, G., Eccles, J., and Cakir, S. (1992). Theory for modeling the equatorial evening ionosphere and the origin of the shear in the horizontal plasma flow. *Journal of Geophysical Research: Space Physics*, 97(A2):1209–1223.

Hanson, W. and Moffett, R. (1966). lonization transport effects in the equatorial f region. *Journal of Geophysical Research*, 71(23):5559–5572.

Hargreaves, J. K. (1992). *The solar-terrestrial environment: an introduction to geospace-the science of the terrestrial upper atmosphere, ionosphere, and magnetosphere.* Cambridge university press.

Heelis, R. (2004). Electrodynamics in the low and middle latitude ionosphere: A tutorial. *Journal of Atmospheric and Solar-Terrestrial Physics*, 66(10):825–838.

Heelis, R., Kendall, P., Moffett, R., Windle, D., and Rishbeth, H. (1974). Electrical coupling of the e-and f-regions and its effect on f-region drifts and winds. *Planetary and Space Science*, 22(5):743–756.

Hernández-Pajares, M., Juan, J. M., Sanz, J., Aragón-Àngel, À., García-Rigo, A., Salazar, D., and Escudero, M. (2011). The ionosphere: effects, gps modeling and the benefits for space geodetic techniques. *Journal of Geodesy*, 85:887–907.

Hofmann-Wellenhof, B., Lichtenegger, H., and Collins, J. (1994). Third edn. gps: Theory and practice.

Huba, J. (2024). Impact of meridional winds on the development of equatorial plasma bubbles: a review. *Frontiers in Astronomy and Space Sciences*, 11:1472642.

Huba, J. D. and Ossakow, S. (1981). Diffusion of small-scale density irregularities during equatorial spread f. *Journal of Geophysical Research: Space Physics*, 86(A11):9107–9114.

Hunsucker, R. D. and Hargreaves, J. K. (2007). *The high-latitude ionosphere and its effects on radio propagation.* Cambridge University Press.

Isaaks, E. H., Srivastava, R. M., et al. (1989). Applied geostatistics.

Isobe, H., Miyagoshi, T., Shibata, K., and Yokoyama, T. (2005). Filamentary structure on the sun from the magnetic rayleigh–taylor instability. *Nature*, 434(7032):478–481.

Jakowski, N., Mayer, C., Hoque, M., and Wilken, V. (2011). Total electron content models and their use in ionosphere monitoring. *Radio Science*, 46(06):1–11.

Joshi, N. C., Bankoti, N. S., Pande, S., Pande, B., and Pandey, K. (2010). Behavior of plasma and field parameters and their relationship with geomagnetic indices during intense geomagnetic storms of solar cycle 23. *arXiv preprint arXiv:1003.2868*.

Jursa, A. S. (1985). *Handbook of Geophysics and Space Environments*, volume 5. Hanscom Air Force Base.

Kamide, Y. and Chian, A. (2007). *Handbook of the solar-terrestrial environment*. Springer.

Kaplan, E. D. and Hegarty, C. J. (2006). Understanding gps: principles and applications second edition. *Artech house*, pages 14–16.

Kastelec, D. and Košmelj, K. (2002). Spatial interpolation of mean yearly precipitation using universal kriging. *Developments in statistics*, 17:149–162.

Kelkar, M., Perez, G., and Chopra, A. (2002). Applied geostatistics for reservoir characterization. *(No Title)*.

Kelley, M. C. (2009). *The Earth's ionosphere: plasma physics and electrodynamics*. Academic press.

Kelley, M. C., Kotsikopoulos, D., Beach, T., Hysell, D., and Musman, S. (1996). Simultaneous global positioning system and radar observations of equatorial spread f at kwajalein. *Journal of Geophysical Research: Space Physics*, 101(A2):2333–2341.

Kepkar, A., Arras, C., Wickert, J., Schuh, H., Alizadeh, M., and Tsai, L.-C. (2020). Occurrence climatology of equatorial plasma bubbles derived using formosat-3/ cosmic gps radio occultation data. In *Annales Geophysicae*, volume 38, pages 611–623. Copernicus GmbH.

Kintner, P. M., Ledvina, B. M., and De Paula, E. (2007). Gps and ionospheric scintillations. *Space weather*, 5(9).

Kitanidis, P. K. (1997). *Introduction to geostatistics: applications in hydrogeology*. Cambridge university press.

Kivelson, M. G. and Russell, C. T. (1995). *Introduction to space physics*. Cambridge university press.

Klenzing, J., Halford, A. J., Liu, G., Smith, J. M., Zhang, Y., Zawdie, K., Maruyama, N., Pfaff, R., and Bishop, R. L. (2023). A system science perspective of the drivers of equatorial plasma bubbles. *Frontiers in Astronomy and Space Sciences*, 9:1064150.

Klobuchar, J. A. (1987). Ionospheric time-delay algorithm for single-frequency gps users. *IEEE Transactions on aerospace and electronic systems*, (3):325–331.

Kockarts, G. (1981). Effects of solar variations on the upper atmosphere. *Solar Physics*, 74(2):295–320.

Kumar, S. (2017). Morphology of equatorial plasma bubbles during low and high solar activity years over indian sector. *Astrophysics and Space Science*, 362(5):93.

Kumar, S. and Chen, W. (2016). Remote sensing of ionospheric plasma bubbles using gps/gnss. In *2016 International Conference on Localization and GNSS (ICL-GNSS)*, pages 1–5. IEEE.

Kumar, S., Chen, W., Liu, Z., and Ji, S. (2016). Effects of solar and geomagnetic activity on the occurrence of equatorial plasma bubbles over hong kong. *Journal of Geophysical Research: Space Physics*, 121(9):9164–9178.

Lan, T. T., Fleury, R., Amory-Mazaudier, C., Thang, N. C., Thanh, N. H., et al. (2016). Tec variations and ionospheric disturbances during the magnetic storm in march 2015 observed from continuous gps data in the southeast asia region. *Vietnam Journal of Earth Sciences*, 38(3):267–285.

Ledvina, S., Ma, Y.-J., and Kallio, E. (2008). Modeling and simulating flowing plasmas and related phenomena. *Comparative aeronomy*, pages 143–189.

Lee, J., Datta-Barua, S., Zhang, G., Pullen, S., and Enge, P. (2011). Observations of low-elevation ionospheric anomalies for ground-based augmentation of gnss. *Radio Science*, 46(06):1–11.

Li, C., Hancock, C. M., Hamm, N. A., Veettil, S. V., and You, C. (2020a). Analysis of the relationship between scintillation parameters, multipath and roti. *Sensors*, 20(10):2877.

Li, G., Ning, B., Liu, L., Zhao, B., Yue, X., Su, S.-Y., and Venkatraman, S. (2008). Correlative study of plasma bubbles, evening equatorial ionization anomaly, and equatorial prereversal e× b drifts at solar maximum. *Radio Science*, 43(04):1–11.

Li, G., Ning, B., Otsuka, Y., Abdu, M. A., Abadi, P., Liu, Z., Spogli, L., and Wan, W. (2021). Challenges to equatorial plasma bubble and ionospheric scintillation short-term forecasting and future aspects in east and southeast asia. *Surveys in Geophysics*, 42:201–238.

Li, Q., Zhu, Y., Fang, K., and Fang, J. (2020b). Statistical study of the seasonal variations in tec depletion and the roti during 2013–2019 over hong kong. *Sensors*, 20(21):6200.

Li, Y., Baorong, Z., Xiaohong, X., and Zijun, L. (2022). Application of a semivariogram based on a deep neural network to ordinary kriging interpolation of elevation data. *Plos one*, 17(4):e0266942.

Liu, K. (2019). Effect of charge accumulation on magnetic rayleigh-taylor instability. *Scientific Reports*, 9(1):10963.

Lühr, H., Xiong, C., Park, J., and Rauberg, J. (2014). Systematic study of intermediate-scale structures of equatorial plasma irregularities in the ionosphere based on champ observations. *Frontiers in Physics*, 2:15.

Magdaleno, S., Herraiz, M., Altadill, D., and Benito, A. (2017). Climatology characterization of equatorial plasma bubbles using gps data. *Journal of Space Weather and Space Climate*, 7:A3.

Maglambayan, V. L. L. and Macalalad, E. P. (2022). Two-dimensional mapping of ionospheric total electron content over the philippines using kriging interpolation. *Atmosphere*, 13(10):1626.

Mandea, M. and Korte, M. (2010). *Geomagnetic observations and models*, volume 5. Springer Science & Business Media.

Manga, N. A., Lakshmanna, K., Sarma, A. D., and Pant, T. K. (2021). Analysis of correlation between roti and s4 using gagan data. *Progress In Electromagnetics Research M*, 99:23–34.

Mannucci, A., Wilson, B., Yuan, D., Ho, C., Lindqwister, U., and Runge, T. (1998). A global mapping technique for gps-derived ionospheric total electron content measurements. *Radio science*, 33(3):565–582.

Matheron, G. (1963). Principles of geostatistics. *Economic geology*, 58(8):1246–1266.

Mayaud, P.-N. (1973). A hundred year series of geomagnetic data 1868-1967. *IAGA Bulletin*, 33:1868–1967.

McNamara, L. F. (1991). *The ionosphere: communications, surveillance, and direction finding*. Krieger publishing company.

Meijering, E. (2002). A chronology of interpolation: from ancient astronomy to modern signal and image processing. *Proceedings of the IEEE*, 90(3):319–342.

Mendillo, M., Meriwether, J., and Biondi, M. (2001). Testing the thermospheric neutral wind suppression mechanism for day-to-day variability of equatorial spread f. *Journal of Geophysical Research: Space Physics*, 106(A3):3655–3663.

Mengist, C. K., Kim, Y. H., Yeshita, B. D., and Workayehu, A. B. (2015). Mapping the east african ionosphere using ground-based gps tec measurements. *Journal of Astronomy and Space Sciences*, 33(1):29–36.

Mersha, M. W., Lewi, E., Jakowski, N., Wilken, V., Berdermann, J., Kriegel, M., and Damtie, B. (2020). A method for automatic detection of plasma depletions by using gnss measurements. *Radio Science*, 55(3):e2019RS006978.

Miranda, J. I. (2005). *Fundamentos de sistemas de informações geográficas.* Embrapa Informação Tecnológica; Campinas: Embrapa Informática Agropecuária.

Misra, P. and Enge, P. (2011). Global positioning system: signals measurements.

Mohannakumar, K. (2008). Stratosphere troposphere interaction: An introduction. *Cochin India, sprin ger.*

Moldwin, M. (2022). *An introduction to space weather.* Cambridge University Press.

Molin, J. P., do Amaral, L. R., and Colaço, A. (2015). *Agricultura de precisão.* Oficina de textos.

Morgan, C. J. (2011). *Theoretical and practical aspects of variography: in particular, estimation and modelling of semi-variograms over areas of limited and clustered or widely spaced data in a two-dimensional South African gold mining context.* PhD thesis.

Ngwira, C. M. (2011). *An analysis of ionospheric response to geomagnetic disturbances over South Africa and Antarctica.* PhD thesis, Rhodes University.

Nigussie, M., Damtie, B., Yizengaw, E., and Radicella, S. M. (2016). Modeling the east african ionosphere. *Ionospheric Space Weather: Longitude and Hemispheric Dependences and Lower Atmosphere Forcing*, pages 207–224.

Opio, P., Dujanga, F., and Ssenyonga, T. (2015). Latitudinal variation of the ionosphere in the african sector using gps tec data. *Advances in Space Research*, 55(6):1640–1650.

Otsuka, Y. (2018). Review of the generation mechanisms of post-midnight irregularities in the equatorial and low-latitude ionosphere. *Progress in Earth and Planetary Science*, 5(1):57.

Patel, N. C., Karia, S. P., Pathak, K. N., et al. (2017). Gps-tec variation during low to high solar activity period (2010-2014) under the northern crest of indian equatorial ionization anomaly region. *Positioning*, 8(02):13.

Paznukhov, V., Carrano, C., Doherty, P., Groves, K., Caton, R., Valladares, C., Seemala, G., Bridgwood, C., Adeniyi, J., Amaeshi, L., et al. (2012). Equatorial plasma bubbles and l-band scintillations in africa during solar minimum. In *Annales Geophysicae*, volume 30, pages 675–682. Copernicus Publications Göttingen, Germany.

Pedatella, N., Aa, E., and Maute, A. (2024). Quasi 6-day planetary wave oscillations in equatorial plasma irregularities. *Journal of Geophysical Research: Space Physics*, 129(4):e2023JA032312.

Pezzopane, M., Pignalberi, A., Coco, I., Consolini, G., De Michelis, P., Giannattasio, F., Marcucci, M. F., and Tozzi, R. (2021). Occurrence of gps loss of lock based on a swarm half-solar cycle dataset and its relation to the background ionosphere. *Remote Sensing*, 13(11):2209.

Pi, X., Mannucci, A., Lindqwister, U., and Ho, C. (1997). Monitoring of global ionospheric irregularities using the worldwide gps network. *Geophysical Research Letters*, 24(18):2283–2286.

Pignalberi, A., Pietrella, M., Pezzopane, M., and Rizzi, R. (2018). Improvements and validation of the iri up method under moderate, strong, and severe geomagnetic storms. *Earth, Planets and Space*, 70:1–22.

Pimenta, A., Fagundes, P. R., Bittencourt, J. A., and Sahai, Y. (2001). Relevant aspects of equatorial plasma bubbles under different solar activity conditions. *Advances in Space Research*, 27(6-7):1213–1218.

Piriz, A., Cortazar, O., Lopez Cela, J., and Tahir, N. (2006). The rayleigh-taylor instability. *American journal of physics*, 74(12):1095–1098.

Portillo, A., Herraiz, M., Radicella, S., and Ciraolo, L. (2008). Equatorial plasma bubbles studied using african slant total electron content observations. *Journal of Atmospheric and Solar-Terrestrial Physics*, 70(6):907–917.

Prölss, G. (2012). *Physics of the Earths space environment: an introduction*. Springer Science & Business Media.

Pyšek, P. and Richardson, D. M. (2010). Invasive species, environmental change and management, and health. *Annual review of environment and resources*, 35:25–55.

Qiang, L., Yanbo, Z., Zhipeng, W., and Kun, F. (2021). A method for automatic detection and characterization of plasma bubbles using gps and bds data. *Chinese Journal of Aeronautics*, 34(5):195–204.

Rao, P. R., Venkatesh, K., Prasad, D., and Niranjan, K. (2013). On the uncertainties in the measurement of absolute (true) tec over indian equatorial and low latitude sectors. *Advances in Space Research*, 51(7):1238–1252.

Ratcliffe, J. A. (1972). *An introduction to ionosphere and magnetosphere.* CUP Archive.

Rezende, L., De Paula, E., Stephany, S., Kantor, I., Muella, M., De Siqueira, P., and Correa, K. (2010). Survey and prediction of the ionospheric scintillation using data mining techniques. *Space Weather*, 8(6).

Rishbeth, H. and Garriott, O. K. (1969). Introduction to ionospheric physics. *Introduction to ionospheric physics.*

Saha, K. (2008). The earth's atmosphere: its physics and dynamics.

Sahai, Y., Fagundes, P. R., and Bittencourt, J. A. (2000). Transequatorial f-region ionospheric plasma bubbles: solar cycle effects. *Journal of Atmospheric and Solar-Terrestrial Physics*, 62(15):1377–1383.

Schaer, S. and helvétique des sciences naturelles. Commission géodésique, S. (1999). *Mapping and predicting the Earth's ionosphere using the Global Positioning System*, volume 59. Institut für Geodäsie und Photogrammetrie, Eidg. Technische Hochschule .

Schunk, R. and Nagy, A. (2009). *Ionospheres: physics, plasma physics, and chemistry.* Cambridge university press.

Schunk, R. W. and Nagy, A. F. (2000). *Ionospheres: Physics, plasma physics, and chemistry.* Cambridge university press.

Seemala, G. and Valladares, C. (2011). Statistics of total electron content depletions observed over the south american continent for the year 2008. *Radio Science*, 46(5).

Seif, A. and Panda, S. K. (2023). Ionospheric scintillation characteristics from gps observations over malaysian region after the 2011 valentines day solar flare. *Journal of Applied Geodesy*, 17(1):79–90.

Seok, H.-W., Ansari, K., Panachai, C., and Jamjareegulgarn, P. (2022). Individual performance of multi-gnss signals in the determination of stec over thailand with the applicability of klobuchar model. *Advances in Space Research*, 69(3):1301–1318.

Shaver, S., Smith, A., Babu, S., Baruah, Y., Bauer, M., Chaturmutha, V., Chen, H., Dalal, B., Dias da Silva, G., Eddy, T., et al. (2024). Exploring observational heliophysics across all scales: Reflections and insights from the 2023 nasa heliophysics summer school. *Perspectives of Earth and Space Scientists*, 5(1):e2023CN000217.

Sibanda, P. and McKinnell, L. (2011). Topside ionospheric vertical electron density profile reconstruction using gps and ionosonde data: possibilities for south africa. In *Annales Geophysicae*, volume 29, pages 229–236. Copernicus GmbH.

Smith, J. and Heelis, R. A. (2017). Equatorial plasma bubbles: Variations of occurrence and spatial scale in local time, longitude, season, and solar activity. *Journal of Geophysical Research: Space Physics*, 122(5):5743–5755.

Sobral, J. H. A., Abdu, M. A., Takahashi, H., Taylor, M. J., De Paula, E., Zamlutti, C. J., De Aquino, M., and Borba, G. (2002). Ionospheric plasma bubble climatology over brazil based on 22 years (1977–1998) of 630nm airglow observations. *Journal of Atmospheric and Solar-Terrestrial Physics*, 64(12-14):1517–1524.

Spatz, D., Franke, S., and Yeh, K. (1988). Analysis and interpretation of spaced receiver scintillation data recorded at an equatorial station. *Radio Science*, 23(3):347–361.

Sultan, P. (1996). Linear theory and modeling of the rayleigh-taylor instability leading to the occurrence of equatorial spread f. *Journal of Geophysical Research: Space Physics*, 101(A12):26875–26891.

Tapping, K. (2013). The 10.7 cm solar radio flux (f10. 7). *Space weather*, 11(7):394–406.

Taylor, G. I. (1950). The instability of liquid surfaces when accelerated in a direction perpendicular to their planes. i. *Proceedings of the Royal Society of London. Series A. Mathematical and Physical Sciences*, 201(1065):192–196.

Tiwari, R., Strangeways, H., Tiwari, S., and Ahmed, A. (2013). Investigation of ionospheric irregularities and scintillation using tec at high latitude. *Advances in Space Research*, 52(6):1111–1124.

Tsunoda, R. T. (1985). Control of the seasonal and longitudinal occurrence of equatorial scintillations by the longitudinal gradient in integrated e region pedersen conductivity. *Journal of Geophysical Research: Space Physics*, 90(A1):447–456.

Türkoğlu, N., Aydin, O., Duman, N., and Çiçek, İ. (2016). Comparison of various spatial interpolation methods for precipitation in türkiye. *Journal of Human Sciences*, 13(3):5636.

Vankadara, R. K., Jamjareegulgarn, P., Seemala, G. K., Siddiqui, M. I. H., and Panda, S. K. (2023). Trailing equatorial plasma bubble occurrences at a low-latitude location through multi-gnss slant tec depletions during the strong geomagnetic storms in the ascending phase of the 25th solar cycle. *Remote Sensing*, 15(20):4944.

Vankadara, R. K., Panda, S. K., Amory-Mazaudier, C., Fleury, R., Devanaboyina, V. R., Pant, T. K., Jamjareegulgarn, P., Haq, M. A., Okoh, D., and Seemala, G. K. (2022). Signatures of equatorial plasma bubbles and ionospheric scintillations from magnetometer and gnss observations in the indian longitudes during the space weather events of early september 2017. *Remote Sensing*, 14(3):652.

Vital, L. F. R., Xu, J., Otsuka, Y., Ayorinde, T. T., Takahashi, H., Barros, D., de Sousa Carmo, C., Figueiredo, C. A. O. B., Wrasse, C. M., Lima, L. M., et al. (2025). On the fresh development of midnight plasma bubbles over south america. *Earth, Planets and Space*, 77(1):131.

Walt, M. (1994). Introduction to geomagnetically trapped radiation. *Camb. Atmos. Space Sci. Ser*, 10.

Wanninger, L. (1993). Effects of the equatorial ionosphere on. *GPS world*.

Woldemariam, S. W. and Gogie, T. K. (2024). Characterize the long-term ionospheric response to the changes in solar activity at low-latitude stations of the east african sector. *Advances in Space Research*, 73(3):1875–1892.

Woodman, R. F. and La Hoz, C. (1976). Radar observations of f region equatorial irregularities. *Journal of Geophysical Research*, 81(31):5447–5466.

Xiong, C., Stolle, C., Lühr, H., Park, J., Fejer, B. G., and Kervalishvili, G. N. (2016). Scale analysis of equatorial plasma irregularities derived from swarm constellation. *Earth, Planets and Space*, 68:1–12.

Yaacob, N., Abdullah, M., and Ismail, M. (2010). *GPS total electron content (TEC) prediction at ionosphere layer over the equatorial region*. IntechOpen.

Ya'acon, N., Yusof, A. L., Ali, M. T., and Idris, A. (2012). Measurement of total electron content (tec) using virtual reference station (vrs) data at ionosphere layer/norsuzila ya'acob...[et al.]. *Journal of Applied Sciences Research*, 8(8):4084–4095.

Yeboah, A., Paulino, I., Medeiros, A., Buriti, R., and Wrasse, C. (2019). Seasonal variation of plasma bubbles during solar cycle 23–24 over the brazilian equatorial region. *Adv. Space Res*, 64(7):1365–1374.

Yokoyama, T., Jin, H., Shinagawa, H., and Liu, H. (2019). Seeding of equatorial plasma bubbles by vertical neutral wind. *Geophysical Research Letters*, 46(13):7088–7095.

Yokoyama, T., Shinagawa, H., and Jin, H. (2014). Nonlinear growth, bifurcation, and pinching of equatorial plasma bubble simulated by three-dimensional high-resolution bubble model. *Journal of Geophysical Research: Space Physics*, 119(12):10–474.

Zakharenkova, I. and Cherniak, I. (2021). Effects of storm-induced equatorial plasma bubbles on gps-based kinematic positioning at equatorial and middle latitudes during the september 7–8, 2017, geomagnetic storm. *Gps Solutions*, 25(4):132.

Zalesak, S., Ossakow, S., and Chaturvedi, P. (1982). Nonlinear equatorial spread f: The effect of neutral winds and background pedersen conductivity. *Journal of Geophysical Research: Space Physics*, 87(A1):151–166.

Zimmerman, D., Pavlik, C., Ruggles, A., and Armstrong, M. P. (1999). An experimental comparison of ordinary and universal kriging and inverse distance weighting. *Mathematical Geology*, 31:375–390.

Zolesi, B. and Cander, L. R. (2014). *Ionospheric prediction and forecasting*. Springer.